OPTICAL IMAGING OF NEURAL AND HEMODYNAMIC BRAIN ACTIVITY

By

JENNIFER LYNN SCHEI

A dissertation submitted in partial fulfillment of
the requirements for the degree of

DOCTOR OF PHILOSOPHY

WASHINGTON STATE UNIVERSITY
Department of Physics and Astronomy

MAY 2011

To the Faculty of Washington State University:

The members of the Committee appointed to examine the dissertation of JENNIFER LYNN SCHEI find it satisfactory and recommend that it be accepted.

David M. Rector, Ph.D., Co-Chair

Matthew D. McCluskey, Ph.D., Co-Chair

Mark G. Kuzyk, Ph.D.

Frederick Gittes, Ph.D.

ACKNOWLEDGMENT

To think that the production of this proposed dissertation was an individual effort would be a grave mistake. Countless people have contributed to this work in a variety of different ways and I am forever grateful to those folks for helping me through this great endeavor.

First and foremost I would like to thank my Mom and Dad for their continued support and encouragement; providing me a ground reference in life, sending me care packages when I thought the end would never be in sight, sharing Collin stories with me when I needed a laugh, and listening to me when the stresses of life became overwhelming. Without this foundation, I would not be where I am today.

Jason Disterhaupt for his love, continued support, and encouragement. For never trying to hold me back, no matter how many things I attempt drown myself with, being a strong foundation for me, and helping me to remember what really matters.

Several faculty members have served as mentors, helping me along the pathway in graduate school. To them I am grateful. Dave Rector for his patience and guidance and allowing me to pick his brain. His generosity has provided me with endless opportunities to grow as a scientist in which I will forever be grateful. Matt McCluskey for always guiding me in the prospective of physics, helping me study for the preliminary examination, and reminding me that walking away can be more helpful than banging my head against the wall. Fred Gittes for initially interesting me in the field of biophysics and his help in editing this dissertation. Mark Kuzyk for enlightening me in a variety of conversations ranging from physical concepts to the Stanley Cup winners. Also, for encouraging me to play hockey, a stress relief and social experience that was necessary for the maintenance of my sanity. Pete Meighan for our invaluable conversations helping me to connect physics and physiology and gain new perspectives.

My brothers, Matt and Dan, for their ability to help me step back from the details and see the bigger picture. In their brotherly fashion, they have continually offered me support and encouragement. My sister-in-law, Heidi, for her kindness, support, and keeping me in the loop. My Grandma, Bev Schei, who thoroughly read every piece of writing I sent and asked questions about the content and implications.

My friends spread across the globe for their endless support and encouragement. I am grateful for everyone who came to visit me in Pullman, Washington and allowed me to share my research, especially Jenny Forrer, Jenni Bolnick, Katie Gruber, Aaron Monson, and Mark Otis. Lynn Bruce Wilson III for our interesting and humorous conversations sharing our undergraduate and graduate school experiences, which were strikingly parallel. Tiffany Taylor, an amazing person, has inspired me to push myself and believe in myself. Kara Yedinak offered support and advise when I needed it most.

To my co-workers in the Rector Lab, especially Amanda Foust, a brilliant scientist and great friend, for teaching me the way of the lobster; Mark McNabb for his computer assistance; Derrick Phillips for his constant string of jokes, albeit dry and nerdy; Christi Pedrow, my mom-in-Pullman, for her open ear and wonderful advise; and Bree Peterson for her technological assistance and behind-the-scenes work. To my co-workers McCluskey Lab, especially Gabriel Hanna for helping me prepare for the preliminary examinations and teaching me how to use LaTeX. The Washington State University Department of Physics and Astronomy faculty and staff for helping me navigate the graduate program.

This work was supported by NIH MH60263, NSF DGE-0900781, and grants from the Beckman Young Investigators Fellowship Program, the Murdock Foundation, the Keck Foundation, and a fellowship from the Poncin Foundation.

OPTICAL IMAGING OF NEURAL AND HEMODYNAMIC BRAIN ACTIVITY

Abstract

by Jennifer Lynn Schei, Ph.D.
Washington State University
May 2011

Chairs: David M. Rector and Matthew D. McCluskey

Optical imaging technologies can be used to record neural and hemodynamic activity. Neural activity elicits physiological changes that alter the optical tissue properties. Specifically, changes in polarized light are concomitant with neural depolarization. We measured polarization changes from an isolated lobster nerve during action potential propagation using both reflected and transmitted light. In transmission mode, polarization changes were largest throughout the center of the nerve, suggesting that most of the optical signal arose from the inner nerve bundle. In reflection mode, polarization changes were largest near the edges, suggesting that most of the optical signal arose from the outer sheath. To overcome irregular cell orientation found in the brain, we measured polarization changes from a nerve tied in a knot. Our results show that neural activation produces polarization changes that can be imaged even without regular cell orientations.

Neural activation expends energy resources and elicits metabolic delivery through blood vessel dilation, increasing blood flow and volume. We used spectroscopic imaging techniques combined with electrophysiological measurements to record evoked neural and hemodynamic responses from the auditory cortex of the rat. By using implantable optics, we measured responses across natural wake and sleep states, as well as responses following different amounts of sleep deprivation. During quiet sleep, evoked metabolic responses were larger compared to wake, perhaps because blood vessels were more compliant. When animals were sleep deprived, evoked hemodynamic responses were smaller following longer periods of deprivation. These results suggest that prolonged neural activity through sleep deprivation may diminish vascular compliance as indicated by the blunted vascular response. Subsequent sleep may allow vessels to relax, restoring their ability to deliver blood. These results also suggest that severe sleep deprivation or chronic sleep disturbances could push the vasculature to critical limits, leading to metabolic deficit and the potential for tissue trauma.

Contents

List of Figures

List of Tables

Dedication

This dissertation is dedicated to those in persuit of continued education,
further knowledge, and a deeper understanding of the world that
surrounds us, striving to quench our innate curiosity.
Especially young women.

Part I

Optical Neural Imaging

Chapter 1

Introduction

Electromagnetic radiation consists of perpendicular electric and magnetic fields propagating through space. The electromagnetic wave spectrum is mapped out as a function of wavelength in Figure 1.1.

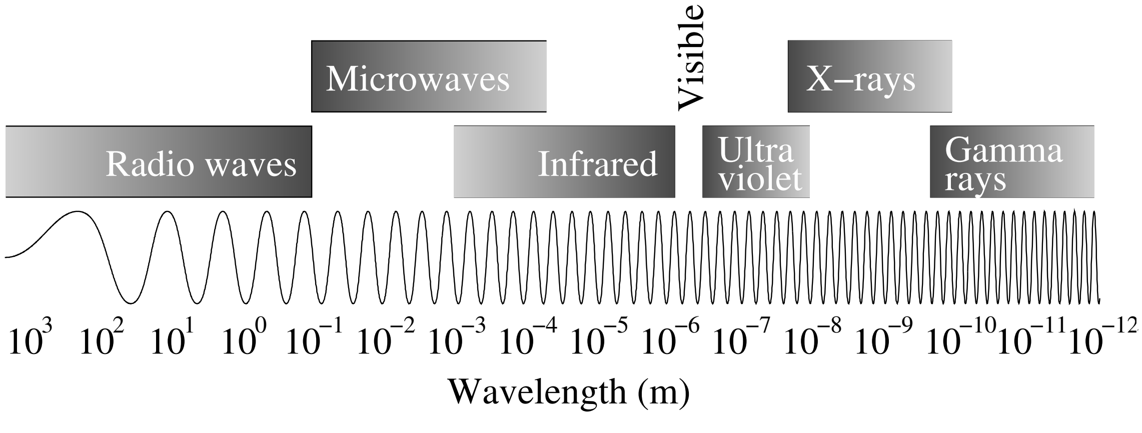

Figure 1.1: Spectrum of electromagnetic radiation as a function of wavelength. Several current imaging technologies use a variety of electromagnetic radiation sources in order to create structural and functional images of the body.

Portions of this chapter were published as: Schei, J.L. and Rector, D.M. 2009. Fast Optical Neurophysiology, chapter 10, pp. 223-243. *In* A.W. Roe (ed.), Imaging the Brain with Optical Methods. Springer, New York, NY.

Wavelengths in the infrared, visible, and ultraviolet range are commonly referred to as light. Ever since the description of light as electromagnetic wave propagation by Maxwell in the 1800's (Maxwell, 1865), the scientific community has utilized disturbances of these waves as an avenue to probe, measure, and record a wide variety of physical processes and properties within the human body (Sochurek and Miller, 1987). For example, x-rays penetrate soft tissues and scatter off denser objects such as bone. X-ray scattering is used to produce visible images of the skeletal structure on radiographic film. Magnetic resonance imaging (MRI) uses pulsed radio waves at a specific region in the body to compile structural and functional images of various soft tissues. Positron emission tomography (PET) imaging relies on an injected short-lived tracer isotope that emits a positron upon decay. The positron eventually collides with an electron and the two annihilate, producing a pair of gamma-rays that propagate in opposite directions. A detector collects gamma-rays and reconstruction techniques trace the location of radioactivity and maps the concentrations within the tissue. Electroencephalography (EEG) and magnetoencephalography (MEG) rely on synchronous neural activity in order to produce ionic currents large enough to generate detectable electrical and magnetic signals. Ultrasound waves, sound at frequencies above human detection, directed into tissues generate echoes at regions where the tissue density changes. The time delay, amplitude, and frequency of the echoes are used to construct low-resolution images of tissue structures.

Most types of electromagnetic radiation used in noninvasive measurements operate with high energy levels and often cause tissue damage with prolonged exposure. Light, on the other hand, provides information using lower energy photons and has a much lower risk of causing tissue damage since it uses non-ionizing radiation. Tissues have different optical scattering and absorption coefficients which can be utilized to construct images of tissue structure (Cheong et al., 1990). Topographical maps of body regions can be generated from photons scattered or transmitted through tissue (Yodh and Chance, 1995; Boas et al., 2002). Photon transport models and image reconstruction techniques describe photon trajectories through inhomogeneous tissue. These techniques enhance images of scatters and absorbers within the tissue, improving the detection of localization of objects, such as tumors (Arridge and Hebden, 1997). Optical imaging techniques and image reconstruction methods can be used as diagnostic tools for detecting tumors and hematomas.

Optical imaging of the human brain also provides a noninvasive means for mapping functional activity. In brain tissue, the primary absorbers of light are oxygenated hemoglobin, deoxygenated hemoglobin, and water (Roggan et al., 1999) and tissue oxygenation changes were first measured by Jöbsis in 1977 (Jöbsis, 1977). Light in the near-infrared (NIR) range has been used for *in vivo* imaging since it penetrates the skin and skull (Eggert and Blazek, 1987; Villringer and Chance, 1997; Hillman, 2007) and interacts with blood, displaying signals correlated with hemodynamic changes as a consequence of neural activity and metabolism (Grinvald et al., 1986; Frostig et al., 1990; Mayhew et al., 2000; Sheth et al., 2003; Devor et al., 2007). Since these signals are indicative of the hemodynamic response, they occur several seconds after the stimulus.

Fast intrinsic optical imaging uses scattered light changes concomitant with neural activation. Optical responses occurring tens of milliseconds after the stimulus may be more closely related to electrical events of neural activation (Rector et al., 1997; Maclin et al., 2004; Rector et al., 2005a). Birefringence imaging techniques utilize polarization optics to measure changes in light polarization as a consequence of neural activation. The information extracted from these signals provides temporal resolution on the order of milliseconds, concurrent with electrical activity.

1.1 Electromagnetic Radiation

As light waves interact with different physical media, they have the potential to undergo alterations or perturbations as they collide with particles. In order to use light to probe neural activity, we must first understand the various ways that light interacts with different materials. Some processes that contribute to changes in electromagnetic radiation are shown in Figure 1.2.

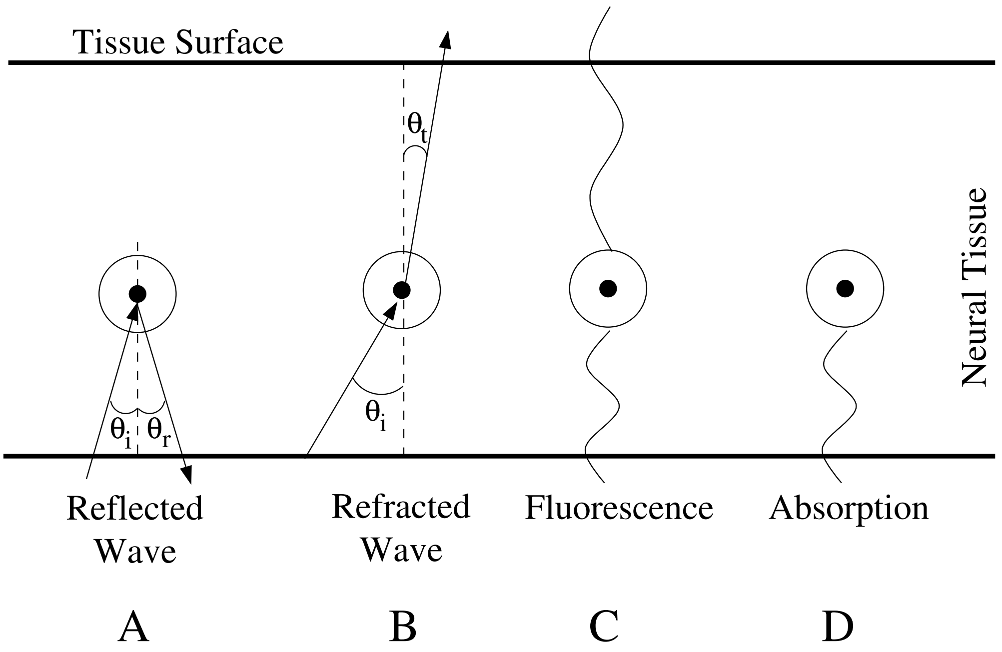

Figure 1.2: Types of electromagnetic disturbances. (A) Rays reflect from the surface of a medium at an angle equal to the incident angle: $\theta_r = \theta_i$. (B) Rays passing between media will change propagation direction due to a change in velocity. The angle of refraction can be calculated using Snell's law (Equation 1.3). (C) Fluorescent materials absorb a particular wavelength of radiation and emit a wave of lower energy, or longer wavelength. (D) Rays can be absorbed by tissue, usually at particular wavelengths.

1.1.1 Elastic Scattering

Scattering, in the simplistic case, is the redirection of light rays. During elastic scattering events, the energy of the photon is conserved while undergoing some change in direction. While conserving energy, light interacting with a medium can either reflect or refract (Figure 1.2(A, B)). The law of reflection states that the angle of incidence is equal to the angle of reflection,

$$\theta_i = \theta_r. \tag{1.1}$$

In other words, we can direct light onto some medium at an angle θ_i and the light will reflect at the same angle $\theta_r = \theta_i$.

Refraction occurs when a light ray changes direction of propagation upon interaction with a non-conductive medium. This can be observed when sticking a pencil into a glass of water. The pencil appears to bend between the air/water interface. This phenomenon occurs because the light wave changes propagation velocity as it enters a different medium. Velocity changes are proportional to the indices of refraction of the two media, where an index of refraction is defined as the speed of light propagating in a vacuum (c) divided by the speed of light propagating through the medium (v),

$$n = \frac{c}{v}. \tag{1.2}$$

The angle at which the light wave will refract is given by Snell's law,

$$n_1 \sin(\theta_1) = n_2 \sin(\theta_2). \tag{1.3}$$

So, when shining light through the air and onto tissue, the light will refract at some angle that can be calculated from Snell's law (Equation 1.3). Dispersive media display wavelength-dependent refraction. For example, shining white light onto a prism creates a rainbow since the prism causes different wavelengths refract at different angles.

Activated tissue will change its index of refraction causing a small, but detectable, change in refracted light (see section 1.6).

1.1.2 Inelastic Scattering

In the case of inelastic scattering, the energy of the photon is not conserved upon interaction with a material. These events cause the photon to lose some energy. Absorption occurs when a material takes in the energy of a photon. This phenomenon is wavelength-dependent, meaning that a material will best absorb waves near particular wavelengths. Molecules that absorb light at specific wavelengths, causing an apparent decrease in light intensity, are called chromophores. Hemoglobin, albumin, water, amino acids, lipids, and many proteins are chromophores available in tissue and serve as indicators for physiological processes.

Fluorescence occurs when a material absorbs light of a particular wavelength, exciting the electrons in the material to a higher energy state. The excitation is followed by a rapid drop of the electrons to a lower energy state. This electron transition results in the emission of a photon of lower energy (Figure 1.2(C)). The process of photon absorption and an appreciable delay of photon emission is called phosphorescence. Currently, many molecules that fluoresce exist as dyes but are toxic to cells. Endogenous fluorescent molecules such as nucleic acids, amino acids, NAD, and NADH, absorb ultraviolet light. These can be used as indicators of neural activity; however, extensive ultraviolet light exposure is damaging to the tissue.

1.1.3 Polarization

Electromagnetic waves consist of perpendicular electric and magnetic fields that oscillate perpendicular to the direction of propagation. They are typically represented by drawing the electric field component. Randomly polarized light is composed of several randomly oriented waves where, on average, there is no preferred direction. This is also commonly referred to as unpolarized light; although this term is somewhat misleading since each wave has a particular polarization angle. In the case of linear polarization, the net wave is oriented in a plane (Figure 1.3). Elliptically polarized light contains two perpendicular wave components shifted out of phase as shown in Figure 1.3.

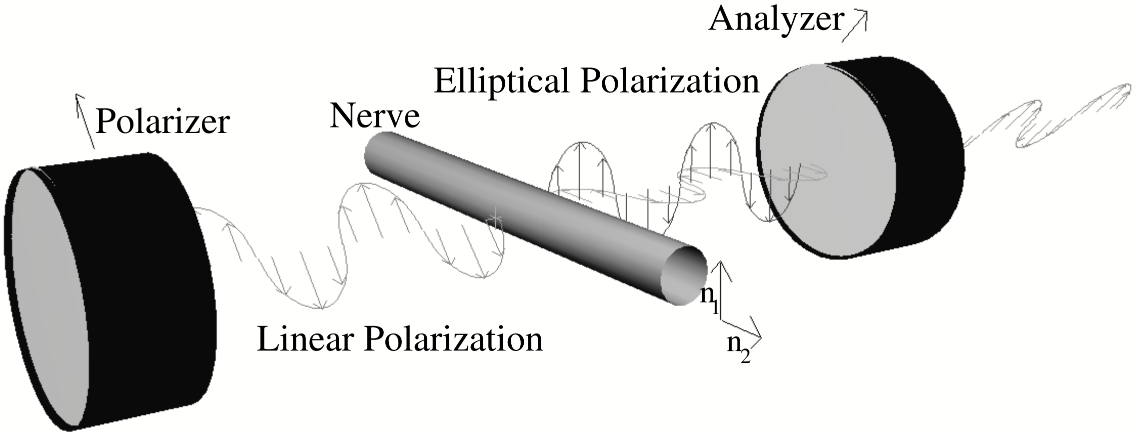

Figure 1.3: Schematic of polarization measurements from an isolated lobster nerve. Incident light was linearly polarized 45 degrees with respect to the long axis of the nerve. The nerve bundle contains perpendicular, differing indices of refraction (n_1 and n_2). The components of the linearly polarized light propagate along the indices of refraction at different velocities, which make up elliptically polarized light. An analyzer, oriented 90 degrees out of phase with the polarizer, transmits the components of the elliptically polarized light along the angle of polarization.

Retinal imaging experiments using bright field, dark field, and polarization illumination techniques showed changes in scattered and transmitted light in response to optical stimulation. While optical responses using bright field illumination yielded single cell resolution images, dark field illumination techniques improved the contrast of the signal by reducing the background light. Polarization measurements showed similar signal contrast to dark field illumination images. The response was confined to the location of illumination whereas the dark field response was subject to responses from spreading neural activation beyond the stimulated area (Yao and George, 2006b). The temporal optical response using dark field illumination was subject to scattering events corresponding to cellular activation delays and metabolic responses. As a result, multiple temporally overlapping components convolve into the optical response (Yao and George, 2006a). Polarization measurement techniques may be advantageous since non-specific background light is excluded by the cross polarizers, enhancing the signal contrast.

1.1.4 Dichroism

A material that holds the same optical properties in all directions is termed optically isotropic. Conversely, a material that exhibits different optical properties depending on the direction of measurement is termed optically anisotropic. A dichroic material is optically anisotropic where light is selectively absorbed in one direction and transmitted in the perpendicular direction. Dichroic properties of a material may be wavelength-dependent. Circular dichroism occurs when left or right circular polarized light is differentially absorbed. Chiral molecules, such as glucose, exhibit circular dichroism and optical imaging techniques can be used to monitor glucose concentration in the blood (McNichols and Cote, 2000). During neural activity, selective absorption properties of perpendicular polarization components may change; however, they have not been separated out from birefringence. One possible way to determine the dichroic properties of a material is to measure the response across the Mueller matrix parameters. The Mueller matrix is a 4x4 matrix that characterizes the polarization properties of a material (see section 1.1.6). Experimentally, we can measure these parameters by changing the incident light polarization and measuring the transmitted and reflected light polarizations. Ultimately, this approach may enable us to decompose the anisotropic optical properties of neural tissue and characterize their changes during neural activation.

1.1.5 Birefringence

A birefringent material is an optically anisotropic material containing perpendicular indices of refraction that differ (n_1 and n_2 as shown in Figure 1.3). Light incident upon a non-equivalent axis will refract into two rays with different velocities. Because of this phenomenon, birefringence literally means double refraction.

Incident linearly polarized light passed through a birefringent material will give rise to a wave component polarized along one index of refraction (n_1) and another wave component polarized along the other index of refraction (n_2). The phase shift between these two perpendicular waves, due to different propagation velocities, results in elliptically polarized light. A second polarizer, also called an analyzer, oriented 90 degrees with respect to the first polarizer transmits the components of the elliptically polarized light parallel to the analyzer. These two wave components combine, resulting in a superposition of linearly polarized light.

In the case of the lobster nerve, the largest signals emerge when light is polarized 45 degrees with respect to the long axis of the nerve (Cohen et al., 1968; Yao et al., 2005). Most of the light passes through the cell or is unaltered during neural activity. Therefore, birefringence techniques provide more robust signals than scattered light measurements because the cross polarizers reject photons that are unaltered by neural activity, thus improving the size of the signal relative to background.

1.1.6 Mueller Matrix Characterization

To determine the polarization properties of activated neural tissue, we can measure the Mueller matrix parameters of the evoked optical response during action potential propagation. The Mueller matrix is a mathematical representation of the polarization properties of a material. Experimentally, we can measure these parameters by changing the incident polarization and measuring the transmitted and reflected polarizations. Ultimately, this approach may enable us to decompose the anisotropic optical properties during neural activation.

The polarization of a beam of light can be fully described by the four Stokes parameters represented by a 4x1 matrix called the Stokes vector

$$S = [I, Q, U, V]^T. \tag{1.4}$$

For convenience, horizontal representation is used and T is the transpose of the matrix (Hecht, 2002).

The parameter I represents the irradiance, Q represents vertical or horizontal polarization, U represents 45 degree polarization, and V represents right or left handedness. The polarization effects of an optical element on an incoming light beam can be described in terms of the 4x4 Mueller matrix so that

$$S_f = MS_i, \tag{1.5}$$

where S_i is the Stokes vector for the incoming light beam, M is the 4x4 Mueller matrix characterizing the polarization effects of the material, and S_f is the Stokes vector for the exiting light beam.

In order to calculate the Stokes parameters, we can measure the light intensity during six different polarization configurations. First, we can measure the intensity of linearly polarized light where the polarization axis was oriented parallel to the x-axis (I_x) and then when the polarization axis was parallel to the y-axis (I_y). From these measurements, the first and second Stokes parameters are

$$\begin{aligned} I &= I_x + I_y \quad (1.6) \\ Q &= I_x - I_y. \quad (1.7) \end{aligned}$$

Next, we can measure the intensity of light polarized 45 degrees with respect to the horizontal axis (I_{45}) and polarized -45 degrees with respect to the x-axis (I_{-45}). The third parameter of the Stokes vector is

$$U = I_{45} - I_{-45}. \quad (1.8)$$

The last Stokes parameter represents circularly polarized light. We can measure the intensity of light through a quarter wave plate with its fast axis oriented 45 degrees from the x-axis (I_L) and then with its fast axis oriented -45 degrees from the x-axis (I_R) (Gerrard and Burch, 1975)

$$V = I_L - I_R. \quad (1.9)$$

The polarization state alterations of light emerging from a material can be described by the 4x4 Mueller matrix

$$\begin{bmatrix} I_f \\ Q_f \\ U_f \\ V_f \end{bmatrix} = \begin{bmatrix} m_{11} & m_{12} & m_{13} & m_{14} \\ m_{21} & m_{22} & m_{23} & m_{24} \\ m_{31} & m_{32} & m_{33} & m_{34} \\ m_{41} & m_{42} & m_{43} & m_{44} \end{bmatrix} \begin{bmatrix} I_i \\ Q_i \\ U_i \\ V_i \end{bmatrix}. \quad (1.10)$$

By knowing the initial polarization state and measuring the final polarization state, we can experimentally calculate the 16 parameters of the Mueller matrix (Equation

1.5) for a biological material. The first column of the Mueller matrix is measured by illuminating the sample with unpolarized light. The Stokes vector for the incoming beam is

$$\begin{bmatrix} I_i \\ Q_i \\ U_i \\ V_i \end{bmatrix} = \begin{bmatrix} \alpha \\ 0 \\ 0 \\ 0 \end{bmatrix}, \tag{1.11}$$

and the first column of the Mueller matrix is

$$\begin{aligned} m_{11} &= I_2/\alpha \\ m_{21} &= Q_2/\alpha \\ m_{31} &= U_2/\alpha \\ m_{41} &= V_2/\alpha. \end{aligned} \tag{1.12}$$

The second column of the Mueller matrix is measured using horizontally polarized incident light. The incoming Stokes vector is

$$\begin{bmatrix} I_i \\ Q_i \\ U_i \\ V_i \end{bmatrix} = \begin{bmatrix} \beta \\ \beta \\ 0 \\ 0 \end{bmatrix}. \tag{1.13}$$

The second column of the Mueller matrix is

$$\begin{aligned} m_{12} &= I_3/\beta - m_{11} = I_3/\beta - I_2/\alpha \\ m_{22} &= Q_3/\beta - m_{21} = Q_3/\beta - Q_2/\alpha \\ m_{32} &= U_3/\beta - m_{31} = U_3/\beta - U_2/\alpha \\ m_{42} &= V_3/\beta - m_{41} = V_3/\beta - V_2/\alpha. \end{aligned} \tag{1.14}$$

To calculate the third column of the Mueller matrix, we polarized incident light 45 degrees with respect to the x-axis. The incoming Stokes vector is

$$\begin{bmatrix} I_i \\ Q_i \\ U_i \\ V_i \end{bmatrix} = \begin{bmatrix} \mu \\ 0 \\ \mu \\ 0 \end{bmatrix}, \tag{1.15}$$

and the Mueller matrix components are

$$\begin{aligned} m_{13} &= I_4/\mu - m_{11} = I_4/\mu - I_2/\alpha \\ m_{23} &= Q_4/\mu - m_{21} = Q_4/\mu - Q_2/\alpha \\ m_{33} &= U_4/\mu - m_{31} = U_4/\mu - U_2/\alpha \\ m_{43} &= V_4/\mu - m_{41} = V_4/\mu - V_2/\alpha. \end{aligned} \tag{1.16}$$

The last column of the Mueller matrix is measured using right circularly polarized light so that the Stokes vector is

$$\begin{bmatrix} I_i \\ Q_i \\ U_i \\ V_i \end{bmatrix} = \begin{bmatrix} \omega \\ 0 \\ 0 \\ \omega \end{bmatrix}, \tag{1.17}$$

and the last column in the Mueller matrix is

$$\begin{aligned} m_{14} &= I_5/\omega - m_{11} = I_5/\omega - I_2/\alpha \\ m_{24} &= Q_5/\omega - m_{21} = Q_5/\omega - Q_2/\alpha \\ m_{34} &= U_5/\omega - m_{31} = U_5/\omega - U_2/\alpha \\ m_{44} &= V_5/\omega - m_{41} = V_5/\omega - V_2/\alpha. \end{aligned} \tag{1.18}$$

To measure the relative polarization changes during the action potential, we can decompose the Mueller matrix into three components. Polarization changes may arise from three separate phenomena: depolarization, a change in the light polarization; diattenuation, a change in amplitude of the electric field components; and retardation, a change in phase of the electric field components. The Mueller matrix can be separated into these three components.

$$M = M_\Delta M_R M_D, \tag{1.19}$$

where M_Δ is the depolarization matrix, M_R is the retardation matrix, and M_D is the diattenuation matrix. While matrix multiplication is non-commutative, this combination of elements has been shown to be physically realizable in clear (Lu and Chipman, 1996) and turbid (Ghosh et al., 2008) media.

The diattenuation matrix is defined as

$$M_D = \begin{bmatrix} 1 & \vec{d}^T \\ \vec{d} & m_D \end{bmatrix}, \tag{1.20}$$

where $\vec{d}$ is the diattenuation vector and m_D is a 3x3 submatrix. The diattenuation vector is defined as

$$\vec{d} = \frac{1}{M(1,1)} \times [M(1,2)\; M(1,3)\; M(1,4)]^T, \tag{1.21}$$

where $M(i,j)$ are the elements of the Mueller matrix. The first element of the diattenuation vector describes horizontal diattenuation, the second element describes 45 degree diattenuation, and the third element describes circular diattenuation. The diattenuation magnitude is defined as

$$d = \frac{1}{M(1,1)} \times [M(1,2)^2 + M(1,3)^2 + M(1,4)^2]^{1/2}. \tag{1.22}$$

The submatrix m_D is defined as

$$m_D = \sqrt{1-d^2}\mathbb{1} + (1 - \sqrt{1-d^2}\hat{d}\hat{d}^T, \tag{1.23}$$

where $\mathbb{1}$ is the 3x3 identity matrix and $\hat{d} = \vec{d}/|d|$.

After calculating the diattenuation matrix, we can define a matrix based on the Mueller matrix and the diattenuation matrix,

$$M' \equiv M M_D^{-1}. \tag{1.24}$$

The matrix M' can be decomposed into the retardation matrix and depolarization matrix,

$$M' = M_\Delta M_R = \begin{bmatrix} 1 & \vec{0}^T \\ \vec{P}_\Delta & m' \end{bmatrix}, \tag{1.25}$$

where $m' = m_\Delta m_R$. We can calculate the three eigenvalues of $m'm'^T$ (λ_1, λ_2, λ_3) and use those values to construct m_Δ,

$$\begin{aligned} m_\Delta &= \pm[m'(m')^T + (\sqrt{\lambda_1\lambda_2} + \sqrt{\lambda_2\lambda_3} + \sqrt{\lambda_3\lambda_1})\mathbb{1}]^{-1} \\ &\quad \times[(\sqrt{\lambda_1} + \sqrt{\lambda_2} + \sqrt{\lambda_3})m'(m')^T + \sqrt{\lambda_1\lambda_2\lambda_3}\mathbb{1}]. \end{aligned} \tag{1.26}$$

The minus sign is used if the determinant of m' is negative. The depolarization matrix can be constructed using $\vec{P}_\Delta$ and m_Δ,

$$M_\Delta = \begin{bmatrix} 1 & \vec{0}^T \\ \vec{P}_\Delta & m_\Delta \end{bmatrix}. \tag{1.27}$$

The depolarization power is defined as,

$$\Delta = 1 - \frac{|\mathrm{tr}(M_\Delta) - 1|}{3}. \tag{1.28}$$

The depolarization power is between 0 and 1, where 1 denotes a completely depolarizing material.

The retardation matrix can be calculated using the matrix M' and the depolarization matrix M_Δ,

$$M_R = M_\Delta^{-1} M' = \begin{bmatrix} 1 & \vec{0}^T \\ \vec{0} & m_R \end{bmatrix}, \tag{1.29}$$

where m_R is a 3x3 submatrix. The total retardance can be calculated as

$$R = \cos^{-1}\left(\frac{\mathrm{tr}(M_R)}{2} - 1\right). \tag{1.30}$$

Optical rotation is the change of the linear polarization plane along the direction of propagation, and can be calculated by

$$\Psi = \tan^{-1}\left(\frac{M_R(3,2) - M_R(2,3)}{M_R(2,2) + M_R(3,3)}\right). \tag{1.31}$$

Molecules with asymmetrical chiral structure, such as glucose, exhibit optical rotation effects (Hadley and Vitkin, 2002).

Linear retardance is the phase difference between the two orthogonal electric fields of linearly polarized light. This can be calculated as

$$\delta = \cos^{-1}\left(\{[M_R(2,2) - M_R(3,3)])^2 + [M_R(3,2) - M_R(2,3)]^2\}^{1/2} - 1\right). \tag{1.32}$$

Mueller matrix characterization fully describes the polarization properties of a material and the effect on light as it passes through the material. By characterizing the polarization change of incident light on an activated nerve, we can dissect the optical changes caused by the action potential. Furthermore, we can optimize these optical imaging technologies in order to reduce non-specific background light, maximize polarization changes related to neural activation, and increase the signal-to-noise.

1.2 Neural Activation

The central nervous system is comprised of nerve cells, glial cells, and blood vessels. Glial cells provide support for neurons and are involved in neurovascular coupling (see section 5.4.3). Blood vessels transport metabolites to the tissue through blood flow (see section 5.4). Neurons conduct electrical signals throughout the nervous system. An image of a pyramidal neuron from a rat cortical slice is shown in Figure 1.4. The soma, or cell body, contains the nucleus and synthesizes proteins. Extending from the soma are two types of processes: axons and dendrites. Axons are long processes that extend from the cell body and conduct signals to other neurons. Dendrites, on the other hand, are short, thin processes that branch out from the soma to other cells and receive signals.

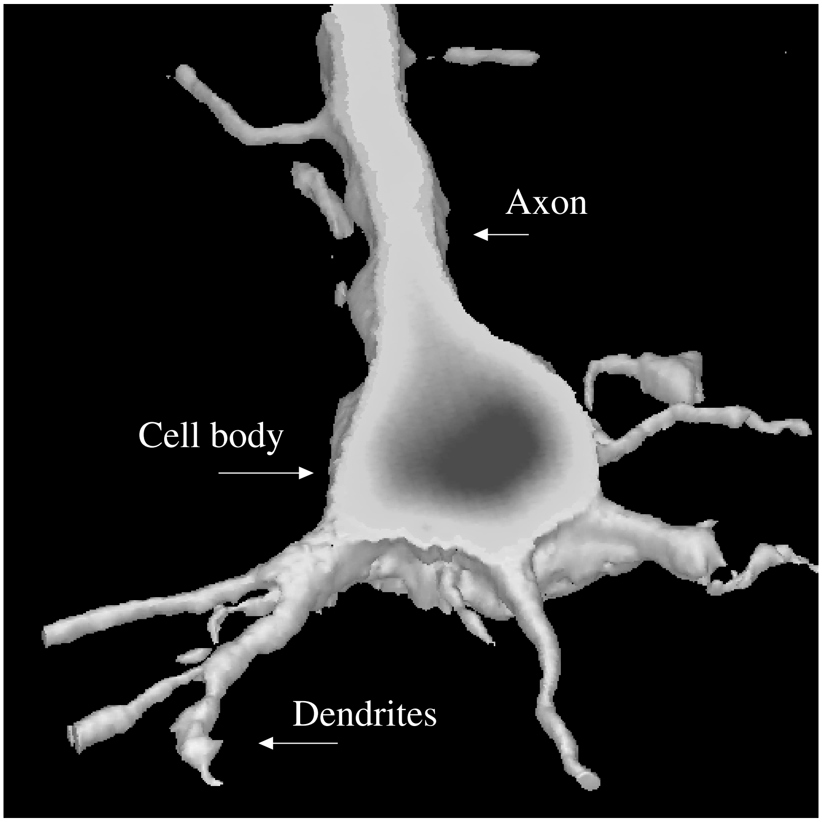

Figure 1.4: Pyramidal nerve cell from a rat cortical slice imaged using confocal microscopy (Rector et al., 2003).

1.2.1 Resting Membrane Potentials

Neural membranes contain ion channels that span the cell membrane which conduct ions, are selective to specific ions, and are regulated by specific stimulation. For example, hair cells in the ear move by pressure waves, and ionic channels in the ear respond to mechanical stimulation. At rest, axons are permeable to sodium (Na^+), potassium (K^+), and chlorine (Cl^-) ions. Two forces act on the ions to produce movement across the membrane: a chemical driving force and an electrical driving force. The concentration gradient across the membrane produces a chemical driving force moving high concentrations of ions to places of low concentration of ions. The electric potential difference across the membrane produces an electrical driving force moving ions to create a low electric potential. At rest, the chemical and electrical forces are equal and opposite. The equilibrium potential can be calculated for each ion using the Nernst equation,

$$E_X = \frac{RT}{zF} \ln \frac{[X]_o}{[X]_i}, \tag{1.33}$$

where R is the universal gas constant, T is the temperature in Kelvin, z is the valence of the ion, F is the Faraday constant, $[X]_o$ is the ion concentration outside the cell, and $[X]_i$ is the ion concentration inside the cell. Ionic flux is the sum of the chemical and electrical forces, multiplied by the membrane conductance,

$$\begin{aligned} \text{ion flux} &= (\text{electrical driving force} + \text{chemical driving force}) \\ &\quad \times \text{membrane conductance}. \end{aligned} \tag{1.34}$$

Since axons have relatively few resting sodium ion channels, the conductance of sodium ions at rest is low. There is a relatively large number of resting potassium

Table 1.1: Concentrations of major ions across a neural membrane at rest in the giant axon of a squid (Kandel et al., 2000)

Ion Species	Concentration in cytoplasm (mM)	Concentration in extracellular fluid (mM)	Equilibrium Potential (mV)
K^+	400	20	−75
Na^+	50	440	+55
Cl^-	52	560	−60

ion channels, and the conductance of potassium ions at rest is high. The distribution of ions across the membrane at rest is shown in Table 1.1.

At rest, there is a higher concentration of intracellular potassium ions, extracellular sodium ions, and extracellular chlorine ions. Ionic gradients are maintained by the sodium-potassium pump, which moves ions against the gradient. Passive ion transfer and active ion pumping counterbalance each other to maintain a steady-state membrane potential at rest. The resting membrane potential can be calculated by the Goldman equation which takes into account ion concentration and permeability for each ion type

$$V_m = \frac{RT}{F} \ln \frac{P_K[K^+]_o + P_{Na}[Na^+]_o + P_{Cl}[Cl^+]_o}{P_K[K^+]_i + P_{Na}[Na^+]_i + P_{Cl}[Cl^+]_i}, \tag{1.35}$$

where V_m is the resting membrane potential and P is the ionic permeability (Goldman, 1943). Since the ionic permeability for potassium ions is high compared to sodium ion permeability, the resting membrane potential is closer to the potassium equilibrium potential. For neurons, the resting membrane potential ranges between -90 mV to -30 mV.

1.2.2 Action Potentials

Axons and dendrites conduct signals through an electro-chemical impulse, called an action potential. The impulse results from electric potential differences across the cell membrane through ion exchange. When membrane depolarization reaches a certain threshold, Na^+ channels rapidly open, or activate, increasing the ionic conductance, and an inward current of sodium ions depolarizes the cell further. During this phase, the membrane potential approaches the sodium equilibrium potential. This is observed as the rising phase of the action potential. Then, sodium ion channels gradually begin to close and become inactivated. At the same time, potassium ion channels open, allowing an efflux of potassium ions and repolarization of the membrane. These two processes contribute to the peak and falling phase of the action potential. When the membrane potential reaches the sodium equilibrium potential, the potassium ion channels close. Since channel closing takes a few milliseconds, the membrane potential dips below the resting membrane potential, closer to the potassium equilibrium potential. This transient hyperpolarization is seen as the undershoot, or after hyperpolarization, in the action potential. Sodium ions are more hydrated than potassium ions and the change in intracellular ionic concentration during the action potential causes an influx of water and cellular swelling. The cellular swelling during an action potential changes the transparency and scattered light measurements can be used to image neural activity. Changes in channel conformation may alter the polarization of light. Thus, light polarization measurements of neural activity are tightly coupled with membrane depolarization (Foust and Rector, 2007).

Following the action potential are two refractory periods of attenuated cellular excitability. Immediately following the action potential is an absolute refractory period where the membrane becomes repolarized, sodium ion channels are inactivated, and a second action potential cannot be generated. Following the absolute refractory period is the relative refractory period. During this time, sodium ion channels return to their resting state. Since not all sodium ion channels recover at the same time, and some potassium ion channels remain open, it is more difficult to generate an action potential. In order to generate a second action potential during the relative refractory period, stronger stimulation is required for the cell to become depolarized to the threshold level.

The action potential propagates down the axon through depolarization of the adjacent axon region. The change in membrane potential decays exponentially with distance

$$\Delta V(x) = \Delta V_0 e^{-\frac{x}{\lambda}}, \tag{1.36}$$

where λ is the length constant, x is the distance along the axon from the depolarization site, V_0 is the membrane potential at $x = 0$, and $V(x)$ is the membrane potential at position x. The length constant can be expressed as

$$\lambda = \sqrt{\frac{R_m}{\rho} \cdot \frac{a}{2}}, \tag{1.37}$$

where R_m is the specific resistance of a unit area of membrane, ρ is the specific resistance of a cubic centimeter of cytoplasm, and a is the cross-sectional area of the axon. Axons with thicker cross-sectional areas will have a larger length constant, depolarize membranes at longer distances, and propagate the action potential more rapidly. The axon diameter determines the propagation velocity, and optical imaging techniques using polarized light can measure action potentials from different size axons and calculate propagation velocities (Carter et al., 2004). The passive spread of membrane depolarization to adjacent regions of the axon generates an action potential in the next segment along the process. Since the initial activated region undergoes a refractory period, the adjacent action potential does not generate an rebound action potential.

The action potential is an all-or-none phenomenon. Initial membrane potential depolarization is graded, meaning that the stronger the stimulation the more depolarized the cell will become. Depolarization of the membrane must reach a threshold in order to initiate an action potential. Through positive feedback from sodium currents, the amplitude of the action potential is constant, regardless of the input current or stimulus intensity. Different regions of the neuron have different densities of sodium ion channels, and areas with a high density are more sensitive to depolarization. Such a region is called the trigger zone.

1.3 History of Neural Imaging

Before the electrical properties of neurons were fully described, scientists used light to study the properties of nerves. Over a century ago, Gustav Mann observed that active cells appear to be larger and swollen (Mann, 1894). This simple yet profound discovery that cells undergo physiological change upon activation led to an explosion of experiments studying neural activity. Subsequently, the squid giant axon was discovered to be the largest and longest nerve in the animal kingdom making it an ideal model for studying neural properties. Some experimenters stretched and twisted squid giant axons in order to study the forces exerted by nerves during activation (Kornakova et al., 1947). Other experimenters emptied the contents of the axon and analyzed the chemical components (Flaig, 1947; Cragg, 1951; Hodgkin and Keynes, 1955). In 1952, Hodgkin and Huxley characterized the electro-chemical properties of the action potential (Hodgkin and Huxley, 1952). Amidst the studies of axon properties, the use of scattered light to image neural activation was demonstrated by Hill and Keynes (Hill and Keynes, 1949). These ground-breaking experiments showed a correlation between activation and opacity changes in nerve bundles. While further studies aimed at connecting the physical components responsible for the changes in scattered light, some investigators discovered that using cross polarizers to image changes in light polarization produced signals that were an order of magnitude larger than scattering signals (Cohen et al., 1968; Tasaki et al., 1968). Additional studies using polarization techniques have characterized the optical signal in order to determine the underlying source of light polarization changes and improve imaging technologies (Carter et al., 2004; Yao et al., 2005; Foust et al., 2005; Foust and Rector, 2007; Foust et al., 2008; Schei et al., 2008). Several investigators have exploited optical imaging techniques *in vivo* in order to investigate brain structure and functionality (Hoshi and Tamura, 1993; Gratton et al., 1997; Rector et al., 1997; Mayhew et al., 2000; Steinbrink et al., 2000; Maclin et al., 2004; Culver et al., 2005; Chen-Bee et al., 2007; Devor et al., 2007). Many of these imaging modalities rely on light scattered from the cortex that provides information related to the hemodynamic consequences of neural activity. Our aim, however, is to use polarization techniques to record information more closely related to the electrical consequences of neural activity.

1.4 Technological Issues

1.4.1 Light Sources

In order to optimize the fractional changes in the evoked optical signals, we studied the polarization responses using different illumination sources. Preliminary experiments utilized halogen lights, emitting white light, to record changes in polarization (Figure 1.5(B)). While these sources exhibit high intensity and stability, they also include a large range of wavelengths which are difficult to exclude using polarizers. This excess amount of light contributes to the background brightness during imaging. Light emitting diodes (LEDs) are also high intensity, but specific to a narrow wavelength.

Polarizers achieved better extinction coefficients (the ratio between the incident and transmitted light) when using narrow bandwidth light sources. In other words, in the absence of tissue, cross polarizers exclude more light when the source is a specific wavelength. These better extinction coefficients reduced the background noise and contributed to larger fractional changes of the evoked responses as shown in Figure 1.5(A) (Foust et al., 2005). Additionally, LED light sources exhibited lower low-frequency noise than halogen lamps (Salzberg et al., 2005). Wavelengths in the near-infrared (NIR) spectrum elicited larger signals and better signal-to-noise ratios (SNR) than wavelengths in the visible spectrum (Figure 1.5(C)). Reducing noise sources and increasing SNRs is crucial for extracting and optimizing these small intrinsic optical signals. By using light sources that emit specific wavelengths with narrow bandwidths, we can achieve better extinction coefficients with the polarization optics and thereby optimize the signal.

1.4.2 Noise Sources In Vitro

While LEDs are superior to white light sources, laser diodes (LD) also have narrow bandwidth emission with high intensity. Many current optical imaging technologies rely on lasers to illuminate tissue because their high intensity and small size. We characterized the instrumental noise components between LEDs and LDs in order to gain a better understanding of noise sources within the optical system. While a LD light source showed a definite change in polarized light correlated with the action potential, the signal was significantly noisier (Figure 1.5(D)). Laser speckle, a noise source deriving from the coherence of the light, significantly increased the root mean square (RMS) noise and contributed to a lower SNR. Increasing the LD

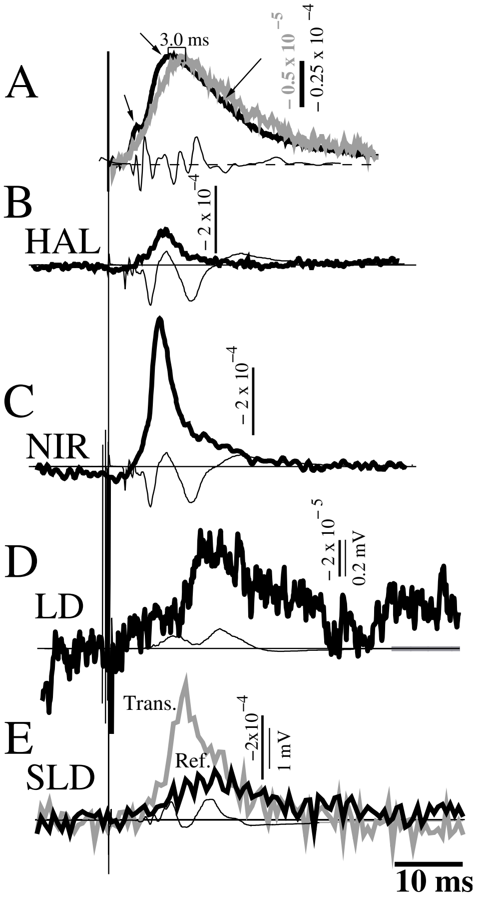

Figure 1.5: Polarization responses were measured from an isolated lobster nerve during activation. (A) The thin gray trace is the evoked electric potential response showing a volley of action potentials that corresponded to axons of different diameters. The thick black line is the change in light polarization and the thick gray line is the 90 degree scattering response. Polarization changes occurred approximately 3 ms before scattering changes. Additionally, three temporal components (arrows) revealed signals from large, medium, and small diameter axons. (B) Polarization changes using a halogen (HAL) light source. (C) Polarization changes using a near-infrared (NIR) light source (880 nm). Wavelengths in the NIR range elicited the largest responses because the polarizers achieved better extinction coefficients at narrower wavelengths. (D) Polarization changes using a laser diode (LD) light source. Small shifts in laser speckle, due to the coherence of the light, contributed to the noisy signal. (E) Reflected (thick black line) and transmitted (thick gray line) polarization changes using a superluminescent diode (SLD) emitting near-infrared light were less noisy because there was much less speckle as with LDs.

intensity resulted in speckle noise dominating the signal and therefore decreasing SNR. The LED source exhibited low RMS noise since it is a non-coherent light source and exhibited an order of magnitude larger SNRs with fewer averages. In fact, signals prevail on single pass trials. This may be due to a combination of brighter illumination and lower noise (Foust et al., 2008). Transmitted polarization signals show more robust responses during neural activation compared to reflected polarization signals. This may be due to fewer photons being back-scattered 180 ° than are transmitted through the nerve bundle.

1.5 Temporal Signal Components

Stimulation of isolated lobster nerves with incident linearly polarized light elicits a decrease in light polarization changes and a decrease in 90 degree scattered light simultaneous to the action potential (Figure 1.5(A)). The fractional changes in scattered light are small, on the order of 10^{-5}. The fractional changes in polarization, however, are an order of magnitude larger (10^{-4}) than those observed during scattering events (Cohen et al., 1968; Tasaki et al., 1968; Carter et al., 2004). The 90 degree scattering measurement experienced a delayed onset of 2-3 milliseconds compared to the polarization signal, suggesting that the mechanisms underlying the optical changes might be different. After averaging the optical signals across stimuli, the polarization signal exhibited a significantly higher SNR than the 90 degree scattering signal. The larger amplitude, earlier onset, and higher SNR characteristics of the polarization signal may be due to the polarization optics rejecting light unaltered by neural activity, therefore, increasing the signal contrast. Scattered light and birefringence imaging techniques are useful because the signals are tightly coupled with the membrane potential, providing measurements with a temporal resolution on the order of milliseconds and a spatial resolution of micrometers (Foust and Rector, 2007). These techniques have the potential to provide information about neural activation in very specific tissue regions.

The electrical potential measured in Figure 1.5(A) shows a volley of action potentials corresponding to axons with different diameters. The evoked polarization signal not only occurred 2-3 milliseconds before the scattering signal, but also exhibited temporal structures related to axon diameter (Carter et al., 2004). The initial peak in evoked response was associated with faster, larger diameter axons whereas the last peak was associated with slower, smaller diameter axons. The temporal structure of the polarization signals allows us to discriminate between different axon diameters. The scattering signal lacked the temporal structure observed in the polarization signal, perhaps because the physiological mechanisms that produce the two optical signals differ.

1.6 Physiological Mechanisms

Several mechanisms may be responsible for the decrease in polarized and scattered light associated with neural activation. Microtubules are birefringent (Oldenbourg et al., 1998), and an influx of water causes axonal swelling and membrane unfolding which may contribute to the change in the evoked optical signal (Yao et al., 2003). Some investigators argue that the source of decreased polarized light is the reorientation of membrane dipoles (Cohen et al., 1968; Landowne, 1985). Studies using pharmacological agents have further dissected the source of the elusive polarization signal. Toxins such as Tetrodotoxin (TTX), Tetraethylammonium chloride (TEA), and Dimethyl sulfoxide (DMSO) that disrupt the membrane potential, concomitantly disrupt signals from voltage sensitive dyes and the polarization signal. These results suggest that polarization changes are tightly coupled to the membrane potential. Large angle scattering has typically been thought to be resultant of cellular swelling. Pharmacological agents that altered the cellular swelling and refractive index had profound effects on the large angle scatting signal. These results affirm that optical scattering signals are closely dependent on changes in the interstitial spaces (Foust and Rector, 2007). However, since several of these physiological processes involved with action potential propagation alter the tissue optical properties, the polarization signal is convoluted compared to the electrical signal.

1.7 Conclusions

Optical imaging techniques can provide a means to image neural activity using changes in polarized light. Several physiological processes during action potential propagation, such as protein conformation changes and cellular swelling, alter light scattering and polarization. Based on these intrinsic optical properties of neurons, we employed methods to image neural activity using polarized light. These techniques provide higher SNRs than scattering measurements since cross polarizers reject background light and improve signal contrast. Since *in vivo* imaging techniques will require reflected signals, we compared polarization signals transmitted and reflected through neural tissue and developed a model of the tissue optical properties. Additionally, brain tissue does not have a regular orientation of processes as in the lobster nerve. We tested the effect of random cell orientation by tying the nerve in an overhand knot prior to imaging.

Chapter 2

Experimental Techniques

2.1 Nerve Preparation

In order to optically image action potential propagation, we used isolated lobster nerves since they produce very little physiological noise and cells are oriented in the same direction. Nerves from the first and second lobster legs, *Homarus americanus* (Sea View Lobster, Kittery, ME, USA), were used to compare the reflected and transmitted polarization signals. Each nerve, approximately 6 cm long and 1-2 mm in diameter, was extracted using the Furusawa pulling out method (Furusawa, 1929) and sutured on each end. We then placed the nerve in a sample chamber (Figure 2.1) brimmed with a bath solution (525 nM NaCl, 13.3 mM KCl, 12.4 mM CaCl, 24.8 mM MgCl, and 5 mM dextrose). The center of the sample chamber contained a glass microscope slide which permitted light to transmit through the nerve. In reflection mode imaging, we placed another glass microscope slide over the top of the imaging area to reduce reflections caused by the bath solution meniscus. Each side of the im-

---

Portions of this chapter were published as: Schei, J.L., McCluskey, M.D., Foust, A.J., Yao, X.C., and Rector, D.M. 2008. Action potential propagation imaged with high temporal resolution near-infrared video microscopy and polarized light. *NeuroImage*, 40(3):1034-1043.

aged area contained 4 wells fitted with silver electrodes. We isolated each well using petroleum jelly before flooding the sample chamber with the bath solution. One end of the nerve was stimulated by a pair of electrodes delivering a 2 mA current pulse at a width of 0.2 ms using a direct current isolated stimulator (Model A365R, World Precision Instruments, Inc., Sarasota, FL, USA). Stimulus intervals were randomly administered between 1 and 2 seconds. Population action potentials were measured both before and after the imaging window using two pairs of electrodes which were spaced 21 mm apart. The signal was averaged over 200 stimuli for each nerve.

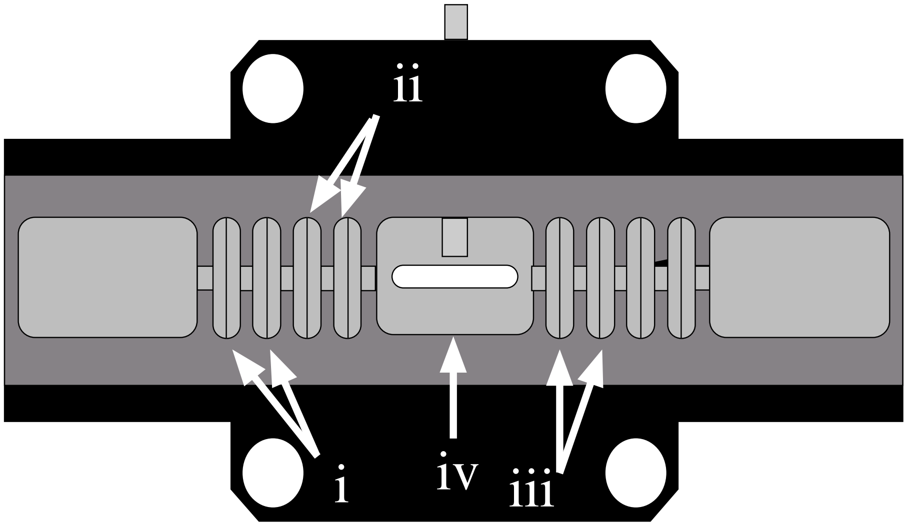

Figure 2.1: Lobster nerve chamber. Stimulating current was delivered by a pair of electrodes (i). The electrophysiological response (EPR) from summed population action potentials was recorded pre-optical (ii) and post-optical (iii). Polarized light shone onto the nerve through the imaging window (iv).

2.2 Imaging Setup

A schematic diagram of the transmission mode experimental setup is shown starting from the bottom in Figure 2.1. We used a free-space superluminescent diode (SLD) module (SLD-380-MP3-TOW2-PD, Superlum Diodes Ltd., Moscow, Russia), with a peak emission wavelength of 833 nm and spectral bandwidth of 23 nm, to illuminate the nerve. The beam was collimated by a lens with a focal length of f = 5 mm (06 3008, Linos Photonics, Milford, MA, USA) and polarized (46087, Edmund Optics, Barrington, NJ, USA) 45 degrees with respect to the nerve. The light projected through the image window of the sample chamber and illuminated the nerve with a 2-3 mm diameter spot. A second polarizer (46087, Edmund Optics, Barrington, NJ, USA) transmitted crossed-polarized light. We focused the image using a lens of focal point f = 12.5 mm (06 3032, Linos Photonics, Milford, MA, USA) onto the CCD camera chip (TC255, Texas Instruments, Dallas, TX, USA) with 10 micron square pixels. Custom built control and acquisition systems were used to collected images at a rate of 1667 Hz (Rector and George, 2001).

In the reflection mode experimental setup, starting from the left in Figure 2.2, we used the same near-infrared SLD light module, a lens of focal length f = 5 mm to collimate the SLD light, and a polarizer to reject p-polarized light and transmit s-polarized light (in the geometry of this experiment, s-polarized light was parallel to the optical table). The s-polarized light was reflected onto the nerve bundle, which yielded an illumination diameter of 2-3 mm, using a polarizing beam splitter (G335599000, Linos Photonics, Milford, MA, USA). Light scattered off of the nerve and traveled through the polarizing beam splitter that only transmitted p-polarized light (Yao et al., 2005). We focused the light with the same lens (f = 12.5 mm) onto the CCD that acquired images at a rate of 1667 Hz.

The long axis of the nerve and the CCD array were oriented at a 45 angle to the polarization of the light in order to maximize the response (Cohen et al., 1968; Yao et al., 2005). The image of the nerve fell on a 108 x 162 pixel portion of the CCD. In order to integrate all of the available light and reduce noise, every 2 pixels were

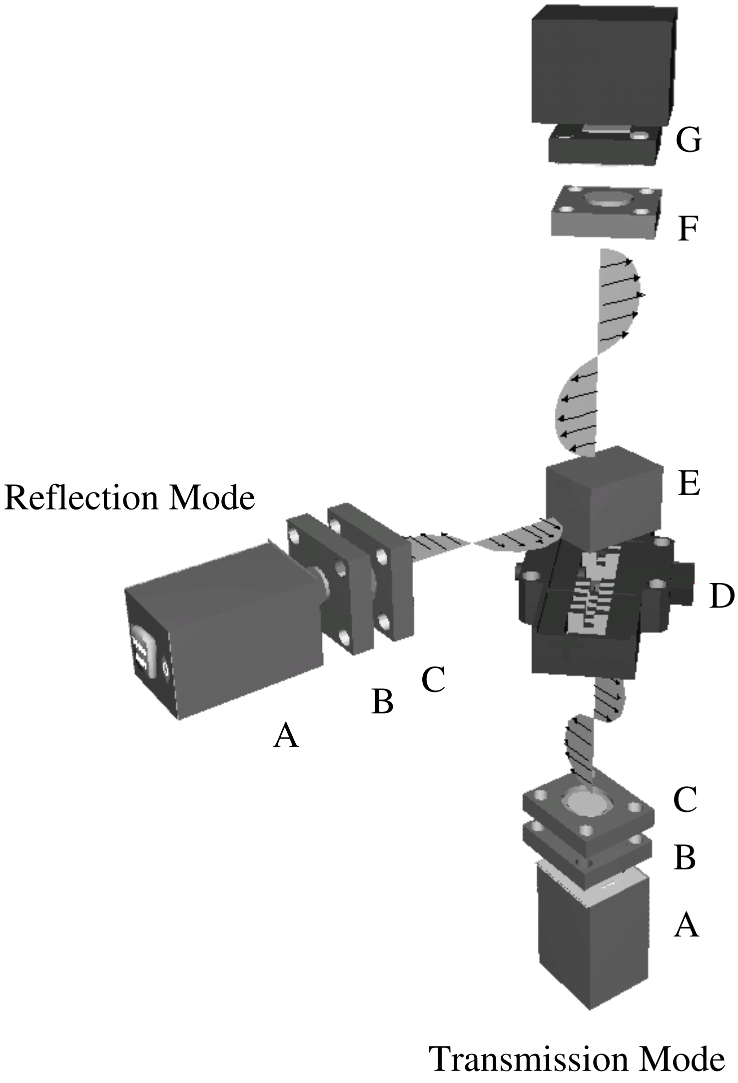

Figure 2.2: Schematic diagram of the transmission mode experimental system (starting from the bottom). Light in the near-infrared spectrum emitted by an superluminescent diode (SLD, A) was collimated by a lens (f = 5 mm) (B) and polarized 45 degrees with respect to the nerve (C). The light passed through the imaging window of the lobster sample chamber (D). Polarized light from the nerve passed through a second polarizer (E). The image was focused by a second lens (f = 12.5 mm) (F) and images were collected by a CCD camera (G). In reflection mode (starting from the left), near-infrared light emitted by an SLD (A) was collimated by a lens (f = 5 mm) (B). The light passed through a polarizer (C), which only transmitted s-polarized light. The s-polarized light was reflected by a polarizing beamsplitter (for reflection mode, the polarizer was replaced by a polarizing beamsplitter) (E) onto the nerve (D). Scattered light from the nerve traveled back through the polarizing beamsplitter, which only transmitted p-polarized light. The light was focused by a lens (f = 12.5 mm) (F) onto a CCD camera (G).

horizontally binned and every 9 pixels were vertically binned, resulting in a 54 X 18 pixel image.

2.3 Data Analysis

All data were analyzed using Octave (www.octave.org), an open source data analysis and mathematical modeling package. We measured the propagation velocity of the electrical signals by dividing the distance between the two electrode pairs (21 mm) by the difference in the time from the population action potential peaks between the first pair of electrodes, before the imaging window, and the second pair of electrodes, after the imaging window. The integrated polarization signal was obtained by averaging the signal across all pixels in the image and dividing by the baseline intensity (dI/I). We calculated the signal-to-noise ratio (SNR) by dividing the peak amplitude of the signal by the root mean square (RMS) of the data from 150-500 ms. RMS values are read in arbitrary data units from the digitizer and are reported in arbitrary units (AU).

The raw image of the nerve was produced by averaging the temporal component of the signal for each pixel in the image and plotting the signal amplitudes. The spatially resolved color images are plots of the signal amplitude given by

$$A(x,y) = -\sum_{t} f(x,y,t), \tag{2.1}$$

where $f(x,y,t)$ was the baseline-corrected signal for pixel (x,y) at a time t. The negative sign was used so that A was positive when the response decreased. The maximal signal amplitude was calculated by summing each pixel across the time interval t = 18-55 ms, corresponding to the time window where the response was maximal.

Since our signal to noise ratio was about 3:1 for individual pixels, we needed a fitting algorithm to model and accurately determine the time dependence of the signal for each pixel. We used the following impulse response function to model the signal

$$F(x,y,t) = \begin{cases} \frac{A(x,y)}{\tau^2}(t-t_0)e^{\frac{-(t-t_0)}{\tau}} & t \geq t_0 \\ 0 & t < t_0, \end{cases} \tag{2.2}$$

where $F(x,y,t)$ was the response function; $A(x,y)$ was the signal amplitude from Equation 2.1; t was the time; τ and t_0 were adjustable constants. This function describes a linear response starting at t_0, followed by an exponential decay. The time t_0 was determined for each pixel using the method of least squares. The rise time τ was assumed to be the same for all pixels; a value of $\tau = 0.004$ s was found to yield the best fit.

In order to determine the relative amounts of polarization changes emanating from different parts of the nerve, pixels from the intensity amplitude plots were averaged horizontally, along the length of the nerve, and divided by the average signal baseline intensity. The resulting plot was the signal dI/I versus vertical pixel number where one pixel equals 0.28 mm. We averaged multiple nerves together to further separate the signal from the noise. Each plot was stretched across a set number of pixels to compensate for variations in nerve positions and widths. The signal amplitudes were also normalized to one, in order to account for varying overall intensities in each image. We used 22 nerves total, 19 in transmission mode and 3 in reflection mode.

An action potential movie was created by baseline correcting, temporally smoothing the signal by a factor of 10 using a convolution smoothing function, and spatially smoothing each pixel using a 3x3 spatial convolution function. Each frame was subtracted from a baseline generated by averaging the first 10 frames together and divided by the DC light intensity, resulting in dI/I. To demonstrate the left to right propagation of the action potential, the image of the nerve was divided into three regions where the middle region was twice the length of the two outer regions. The optical signal from the outer two regions was divided by the baseline intensity to give dI/I. The signal was filtered between 0 and 200 Hz and numerically differentiated to illustrate the latency of the signal between the two ends of the nerve. We expect that the leftmost region will change before the rightmost region if the action potential propagates from left to right.

In order to test the effect of random cell orientation, as occurs *in vivo*, we collected data from 5 nerves, each tied in an overhand knot before imaging. We created images of the average response over time to show the locations of the polarization signal. The temporal signal was filtered between 0 and 400 Hz, smoothed by a factor of 2, and then plotted for four individual regions within the nerve. An overlying fit to the signal was then obtained using Equation 2.2.

Chapter 3

Fast Neural Signals

3.1 Theoretical Modeling

3.1.1 Spatial Signal Components

We quantified the relative contributions of reflected and transmitted light to the overall signal by developing a model of the intensity profile across the width of the nerve using simple geometric considerations.

The nerve was modeled as a cylindrical nerve bundle with a radius R_b surrounded by a sheath membrane of thickness R_s (Figure 3.1) to determine the optical properties of the comprising materials. Light rays were incident on the nerve at a perpendicular distance r from the center and the depolarization of light was assumed to be proportional to the path length through the material. We assumed that photons traveled to the center of the nerve before being scattered, on average. Light refraction was assumed to be negligible since the refractive index of the nerve was similar

---

Portions of this chapter were published as: Schei, J.L., McCluskey, M.D., Foust, A.J., Yao, X.C., and Rector, D.M. 2008. Action potential propagation imaged with high temporal resolution near-infrared video microscopy and polarized light. *NeuroImage*, 40(3):1034-1043. and Schei, J.L. and Rector, D.M. 2009. Fast Optical Neurophysiology, chapter 10, pp. 223-243. *In* A.W. Roe (ed.), Imaging the Brain with Optical Methods. Springer, New York, NY.

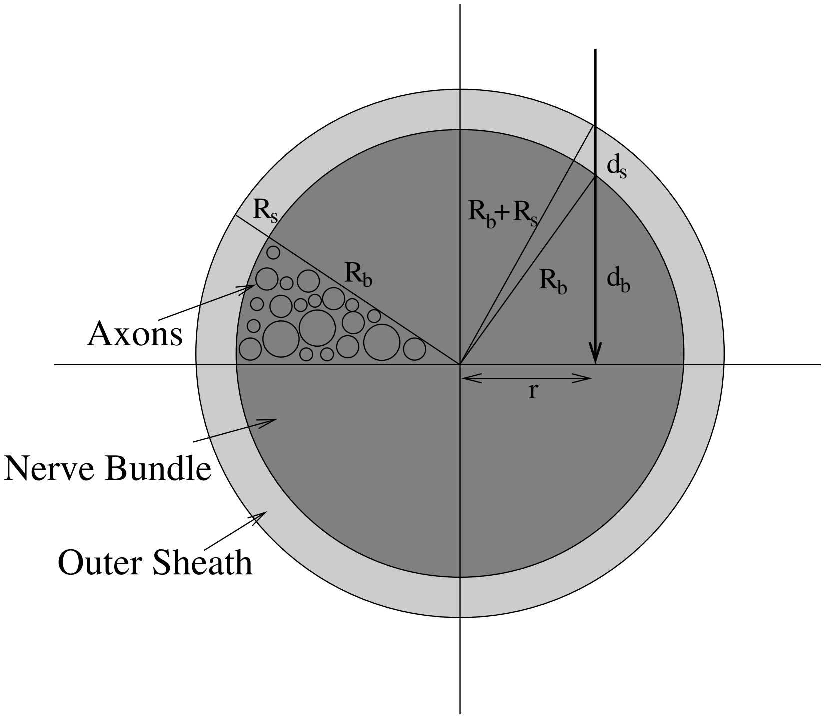

Figure 3.1: The nerve was modeled as a cylindrical nerve bundle of radius R_b encased by a membrane of thickness R_s. A light ray, indicated by the arrow, displaced by a distance r from the center of the nerve traveled a distance d_s and d_b through the membrane and bundle, respectively.

to the refractive index of the bath solution (Stepnoski et al., 1991). We calculated the path length through each material using the Pythagorean theorem. The path length through the outer sheath, d_s, as a function of r was given by the following equation:

$$d_s(r) = \begin{cases} 0 & r > R_s + R_b \\ \sqrt{(R_s + R_b)^2 - r^2} & R_b < r < R_b + R_s \\ \sqrt{(R_s + R_b)^2 - r^2} - \sqrt{R_b^2 - r^2} & r < R_b. \end{cases} \tag{3.1}$$

When r was greater than R_b and less than $R_b + R_s$, light traveled through the outer sheath only whereas when r was less than R_b, light traveled through both the outer sheath and the inner bundle. The path length through the inner bundle was calculated using the following equation:

$$d_b(r) = \begin{cases} 0 & r > R_s + R_b \\ \sqrt{R_b^2 - r^2} & r < R_s + R_b. \end{cases} \tag{3.2}$$

3.1.2 Temporal Signal Components

The optical properties of each material were modeled separately using $(A_s d_s(r) + A_b d_b(r))$ where d_s and d_b were the path lengths through the outer sheath and inner bundle, respectively, as calculated in Equation 3.1 and Equation 3.2; A_s and A_b were empirical constants. We modeled the intensity of light traveling through a medium using an exponential. We assumed a weak scattering limit meaning that photons underwent few scattering events before detection. In transmission mode, the intensity of the light was modeled by

$$I_T(r) = I_0 e^{-(k_s d_s + k_b d_b)}, \tag{3.3}$$

where I_0 was the initial intensity; k_s and k_b were the extinction coefficients of the outer sheath and inner bundle, respectively; d_s and d_b were the path lengths through the respective materials. Photons were assumed to scatter elastically. In other words, the light could only be either transmitted or reflected through the material. From this premise, the intensity of reflected light was given by

$$I_R(r) = I_0(1 - e^{-(k_s d_s + k_b d_b)}). \tag{3.4}$$

By combining the polarization properties of the material with the intensity of the signal, we modeled the transmission mode signal using the equation

$$S(r) = (A_s d_s(r) + A_b d_b(r))e^{-(k_s d_s + k_b d_b)}, \tag{3.5}$$

where $S(r)$ was the optical signal obtained from the nerve at each point along the radius; d_s and d_b were the path lengths through the membrane and bundle, respectively; A_s and A_b were empirical constants; k_s and k_b were the extinction coefficients of the material. The reflection mode signal was modeled using the equation

$$S(r) = (A_s d_s(r) + A_b d_b(r))(1 - e^{-(k_s d_s + k_b d_b)}). \tag{3.6}$$

Equation 3.5 and Equation 3.6 were numerically integrated over each pixel width to simulate the CCD response. The parameters were determined using a reduced chi-squared fit.

3.2 Experimental Results

3.2.1 Simultaneous Electrical and Polarization Signals

A plot of the change in intensity divided by the baseline intensity (dI/I) integrated over the entire imaged region for both reflection and transmission mode along with the electrophysiological response (EPR) is shown in Figure 3.2. The EPR signal (top panel of Figure 3.2) was recorded both before and after the imaging window, as shown in Figure 2.1 (ii and iii, 21 mm apart), and both responses are composed of several waveforms corresponding to the activation of axon populations of different sizes (Carter et al., 2004). Propagation velocities were calculated for the different axon sizes using the EPR signals. For large (l), medium (m), and small (s) axons, the calculated velocities were 3.28 m/s, 2.04 m/s, 1.63 m/s respectively. The polarization changes in both reflection and transmission mode (bottom panel of Figure 3.2) shows a clear response after electrical stimulation, corresponding to the timing of the EPR. While the signal is discernible in both transmission and reflection mode imaging, the signal amplitude in transmission mode is about 3 times larger than in reflection mode. Since the total noise for the recorded signals was 12.3 AU (arbitrary units), and the measured root mean square (RMS) noise for the recording system (9.1 AU), system noise accounted for a larger proportion of the RMS noise calculated due to physiological noise (8.3 AU). Thus, a significant source of noise originated from the CCD camera. The signal-to-noise ratio (SNR) in transmission mode is 5.6 while the SNR in reflection mode is 3.6. The low signal amplitude in reflection mode may be due to significantly fewer photons both changing polarization and scattering a full 180 degrees. In transmission mode, a larger number of photons change polarization due to neural activity and transmit directly through the material with few scattering events. Additionally, in reflection mode, some scattering from interfaces may not have been specific to neural activity, causing a weaker signal.

3.2.2 Transmission Mode Imaging

Spatially resolved images in transmission mode are shown in Figure 3.3(A, B). The horizontal and vertical coordinates are parallel and perpendicular to the nerve respectively. Figure 3.3(A) is the transmitted light intensity image of the nerve averaged across time. The diffuse properties of the nerve bundle required a lens to focus the light onto the camera. Reduced spatial resolution and blurring of the image was partially dependent on our ability to adjust the focus of the image as well as pixel binning across the image. The image of the nerve is vertically centered in the plot,

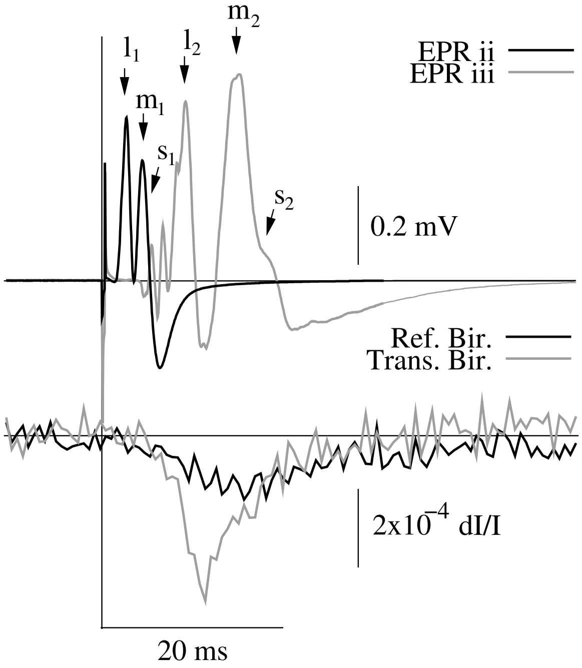

Figure 3.2: Electrical and optical measurements of a lobster nerve. The vertical line indicates the time of stimulus. The upper panel shows the EPR before the imaging window (thin black trace) and after the imaging window (thin gray trace). The action potential contains multiple components corresponding to axons with different diameters. Signal components from EPR ii are labeled as large (l_1), medium (m_1), and small (s_1) axons and signal components from EPR iii are labeled as large (l_2), medium (m_2), and small (s_2) axons. The optical signal was obtained by averaging all of the pixels in the CCD array and dividing the change in intensity by the baseline intensity. The thick black trace is the transmitted signal and the thick gray trace is the reflected signal.

as indicated by the two arrows. The intensity of the light appears evenly spread throughout the nerve. A spatial plot of the signal amplitude, which is summed over the peak of the response (18-55 ms), is shown in Figure 3.3(B). An increase in amplitude correlates to a decrease in intensity, pseudo-colored with warmer colors. The large changes in birefringent light appear ubiquitously throughout the nerve.

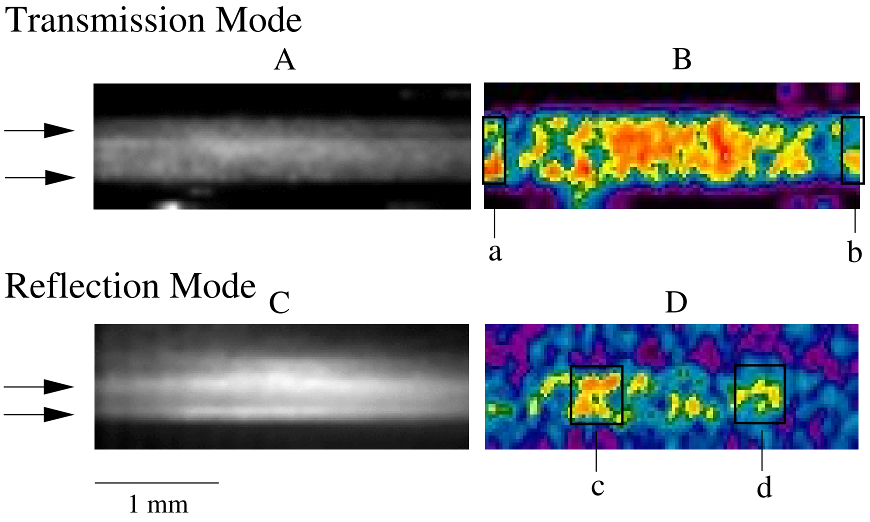

Figure 3.3: An image of the transmission mode intensity averaged over time is displayed in (A). The arrows indicate the edge of the nerve. The pseudo-colored amplitude image of the transmission mode baseline corrected signal summed from 18 ms to 55 ms for each pixel is shown in (B). Decreases in polarized light correspond to warm colors where black pixels represents 0 dI/I and white pixels represent 2 x 10^{-3} dI/I. The signal intensity is evenly spread throughout the nerve. An image of reflection mode intensity is displayed in (C). The arrows indicate the edges of the fascicle. The reflection mode pseudo-colored amplitude image is shown in (D) where a decrease in polarized light corresponds to warmer colors with black pixels representing 0 dI/I and white pixels representing 1 x 10^{-3} dI/I. The regions of maximum amplitude are mostly located near the fascicle edges. The signals in regions a, b, c, and d were averaged together and fit to the temporal model shown in Figure 4.4.

3.2.3 Reflection Mode Imaging

While most birefringence studies focus on the transmitted signal, reflection mode imaging is required for *in vivo* imaging. Before employing birefringence techniques *in vivo*, we first optimized a reflection imaging modality.

A spatially resolved reflection mode intensity image averaged across time is shown in Figure 3.3(C). The edges of the nerve bundle are clearly resolved in this picture, as indicated by the arrows. Some of the scattered light, particularly near the center of the image, may be due to reflections from the glass/water interface. A spatial plot of the signal response, summed from 18 to 55 ms, is shown in Figure 3.3(D) where a decrease in intensity corresponds to warmer colors. The highest intensity of light occurred at the edges of the nerve (Figure 3.3(D)). This suggests that a significant fraction of the reflected polarization changes in lobster nerves arose from the outer fascicle sheath.

3.2.4 Temporal Signal Components

We modeled the temporally resolved polarization signal in order to extract the neural components from the noise. This model can serve as a template for noisy reflection mode signals and perhaps be used in single pass trials. Figure 3.3 shows the signal for four separate regions (a, b, c, and d) corresponding to the locations outlined in Figure 3.2. The corresponding temporal model was fit using Equation 2.2.

The action potential propagates along the nerve from left to right in Figure 3.3(D). In principle, this motion should result in an increase in t_0 with x. To examine this effect, we performed a least-squares linear fit on t_0,

$$t_0(x) = a + bx, \tag{3.7}$$

where $a = 32.8 \pm 0.6$ ms and $b = 0.87 \pm 0.4$ s/m. The uncertainties were calculated using error propagation methods. The positive value for b verifies that the action potential propagates from left to right and taking the inverse gives a propagation velocity of 1.15 ± 0.5 m/s. This velocity is marginally slower than the velocity calculated by the two electrode pairs in Figure 3.2 (1.63 m/s) and earlier reports (Carter et al., 2004), 1.5 m/s. Our propagation velocity derived from the optical signal was comparable only to the slowest propagation velocities perhaps because of temporal smearing in our analysis together with the noise contribution which may have blan-

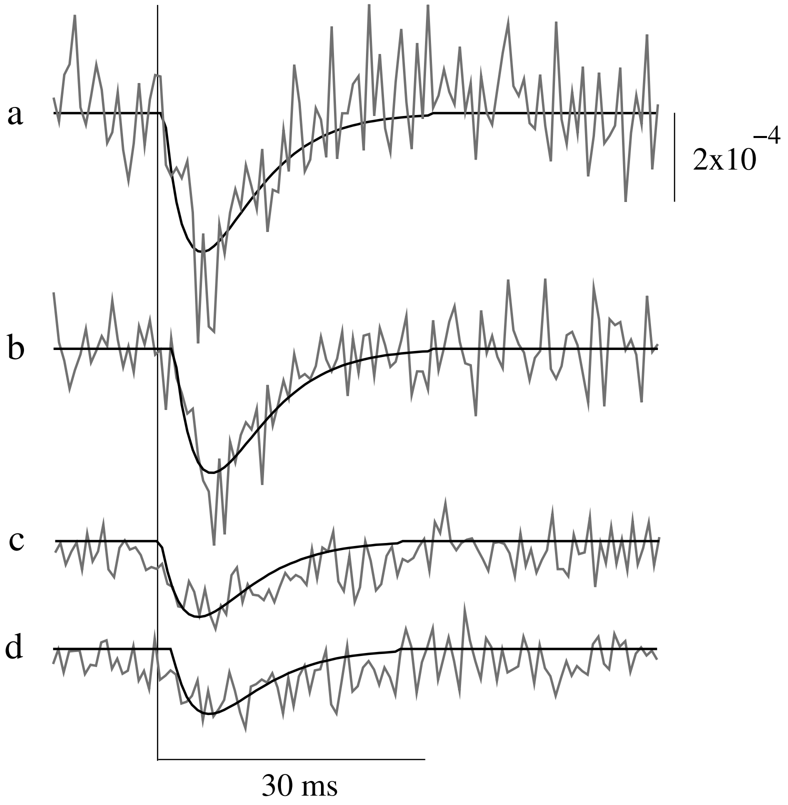

Figure 3.4: Plot of the light intensity changes as a function of time, for four regions (shown in Figure 3.3); two in transmission mode (a and b) and two in reflection mode (c and d). The solid black line is a fit to the data (gray line) using Equation 2.2. A least squares fit of the temporal model across the length of the nerve showed that the action potential propagates from left to right with a velocity of 1.15 ± 0.5 m/s.

keted the signal. It could also be due to slower response times for the biophysical components leading to the polarization changes or perhaps the contributions of the smallest, slower axons were greatest (Carter et al., 2004).

3.2.5 Geometrical Considerations for Signal Sources

In order to identify the source of the polarization signal from the reflection and transmission modes, we analyzed the relative contribution of the signal across the width of the nerve, which correlates to the vertical pixel number. The signals were modeled using Equations 3.5 and 3.6 and setting $\frac{A_s}{A_b} = 6.25$, $R_b = 1.67$ mm, $R_s = 0.42$ mm, $k_s = 1.76$ mm^{-1}, and $k_b = 0.32$ mm^{-1} and fit using means of reduced chi-squared ($\chi^2 = 0.22$ for transmission mode and $\chi^2 = 2.65$ for reflection mode where $p > 0.99$).

The transmission mode vertical pixel intensity is shown in Figure 3.5(A). The signal intensity was small near the edges of the nerve and gradually increased to a plateau across the middle of the nerve. A slight decrease in the intensity was observed in the center of the nerve but a paired students t-test between the circled pixels in Figure 3.5(A) revealed that this dip was not significant across the 19 nerves recorded ($p > 0.95$). As a result, the simulation (gray dotted line in Figure 3.5) shows a plateau of intensity across the center of the nerve.

The reflection mode sample data in Figure 3.5(B) shows significant maxima intensity peaks near the edges of the nerve image ($p < 0.05$). If we assume that the nerve is a uniform cylinder, we expect a symmetric intensity profile, however, the peak intensity at pixel 3 is not as robust as the peak intensity at pixel 16. This discrepancy may be due to the inhomogeneity of the nerves. Furthermore, the light may not have been centered on the nerve resulting in a larger intensity of birefringent light on one side of the nerve relative to the other side of the nerve.

The transmitted signal appears to dominate across the middle of the nerve suggesting that the inner nerve bundle is more transmissively polarizing than the outer sheath. Thus, photons traveling through a large portion of the inner nerve bundle material change polarization, but are less likely to scatter at large angles. The peaks appearing at the edge of the nerve in reflection mode imply that more of the signal arises from the fascicle sheath. We conclude that this material is more reflectively polarizing. The path of a photon on the outer edge of the nerve travels through more

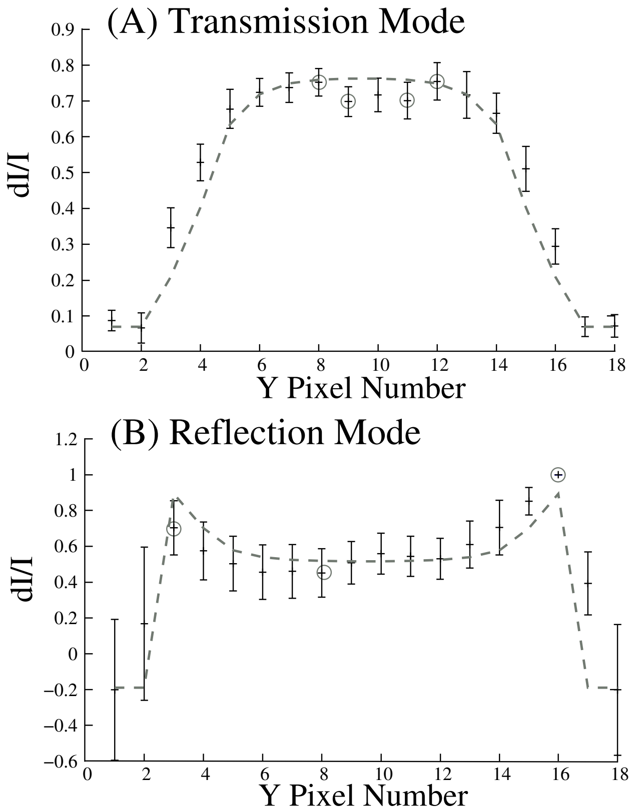

Figure 3.5: Panel (A) illustrates a plot of the transmission mode signal amplitude as a function of distance (Y), obtained by averaging pixels horizontally, along the length of the nerve. The sample data is the signal of 19 nerves stretched to a set size, normalized to one, and then averaged together. The dashed line was obtained by means of best fit using Equation 3.5. The intensity is small along the edges of the nerve and gradually increases towards the middle. A paired students t-test shows that differences between the highest and lowest points in the middle (circled) are insignificant even at 14 degrees of freedom and a 95% confidence interval (pixel 8 versus pixel 9, t = 2.13; pixel 11 versus pixel 12, t = 1.34). Overall, the signal is evenly distributed throughout the middle of the nerve. Panel (B) shows a plot of the reflection mode scattering amplitude as a function of distance (Y) where the two peaks that correspond to maxima in the signal occur at the edges of the fascicle. A paired students t-test confirms that the signal intensity between the edge and center of the nerve (circled) is significant at 3 degrees of freedom and a 95% confidence level (pixel 3 versus 8, t = 4.88; pixel 8 versus pixel 16, t = 4.05). The dashed line is a fit to the data using Equation 3.6. The data was averaged from 3 nerves, each image stretched to a set size to account for width variations and then the intensity is normalized to one.

outer sheath tissue than a photon elsewhere on the nerve. This longer path length in the fascicle sheath allows for a higher probability that a photon is scattered.

The spatial components contributing to the polarization signal can resolve the neural constituents responsible for generating the signal. Spatial studies of the evoked polarization signals from lobster nerves revealed that the transmitted signals arose predominantly from the inner nerve bundle rather than the outer sheath. Cohen *et al.* (1968) found that the signal intensity was larger at the edge of a squid giant axon in transmission mode, hypothesizing that the transmitted polarization signal arises from the edge of an axon. These results, however, originated from a single large axon whereas our data was recorded from a lobster leg nerve which contained bundles of axons surrounded by an outer sheath. While the transmitted signal may peak at the edge of a single axon, a bundle containing hundreds of axons may wash out these peaks revealing an evenly distributed transmitted intensity profile throughout the nerve. Reflected polarization signals revealed that the largest spatial component of the signal emanates from the outer sheath of the nerve bundle because the outer sheath is more reflective (Schei et al., 2008). Birefringence techniques applied *in vivo* require the use of reflected light topologies and thus will rely on short range polarization changes.

3.2.6 Action Potential Movie

We compiled the transmission mode spatially resolved images to illustrate the detection of neural activation and action potential propagating along the nerve using polarized light. Figure 3.6 shows successive frames of the change in polarized light. Beginning at 7.2 ms after the stimulus, sporadic regions on the left end of the nerve begin to show a change in polarization which moves right through 10.2 ms. The early components of this response may represent the faster motor axon action potentials.

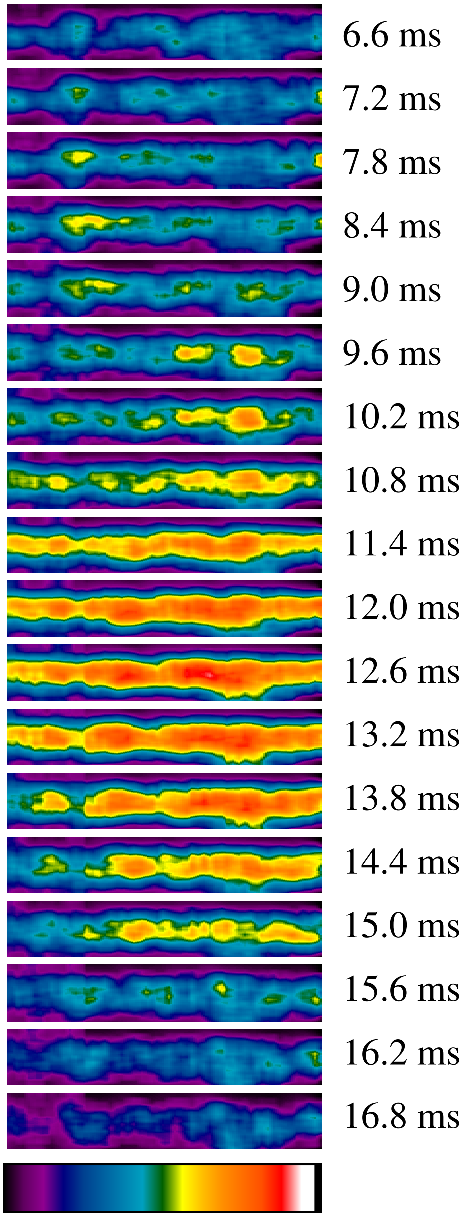

Figure 3.6: Transmission mode action potential movie. Each frame was subtracted from the baseline intensity and divided by the DC light intensity resulting in dI/I. A decrease in intensity corresponds to warmer colors where black pixels are equivalent to 0 dI/I and white pixels are equivalent to 1.0 x 10^{-4} dI/I. The time is in milliseconds after the stimulus. Neural activation begins at 15.6 ms and peak activation occurs at 17.4 ms. Because the rise in activation is fast, we see most of the nerve change in intensity at 15.6 ms. The action potential propagates from left to right, as is seen by the slower decay of the signal on the right side of the nerve at 19.2 20.4 ms.

At 10.8 ms, the left portion of the nerve shows activation from the slower axons, mixed with the later parts of the fast action potentials. The signal moves to the right once more at a slower rate, tapering off at 15.6 and 16.2 ms. In these frames, the action potentials appear to propagate from left to right, as would be expected since the stimulus electrodes are on the left side.

In order to compare the propagation velocity determined by the fit data (Figure 3.4), the nerve image was divided into three regions and the average signal intensity from the outer two regions were used to measure response time. To reduce noise in the response, frequencies greater than 200 Hz were filtered from the data. Figure 3.7 shows the differentiated dI/I signal from regions A and C. The signal from the left region occurs first, verifying that the action potential propagates from left to right. From the rising phase information, the propagation velocity of the action potential volley was calculated to be 2.57 m/s. Our rising phase velocity may reflect the activation of medium axons, whereas the peak response times reported in Figure 3.6 may be dominated by the slowest axons. While we were able to resolve the slower action potential propagation from the smaller axons, better video technology is required to image the different components comprising the polarization signal, especially the fast rising phase, and faster sampling rates would allow for more accurate measures of propagation velocities.

The initial response began on the left side, where the stimulus wires were placed, and corresponded to the activation of large diameter axons. The largest portion of the signal arose from medium diameter axons, although it involved components from axons of all sizes. The slow decay began on the left side and correspond to small diameter axons. Being able to resolve, both spatially and temporally, movies of action potential propagation demonstrates the advantages of fast intrinsic optical imaging. These imaging technologies have spatial resolution on the order of tens of

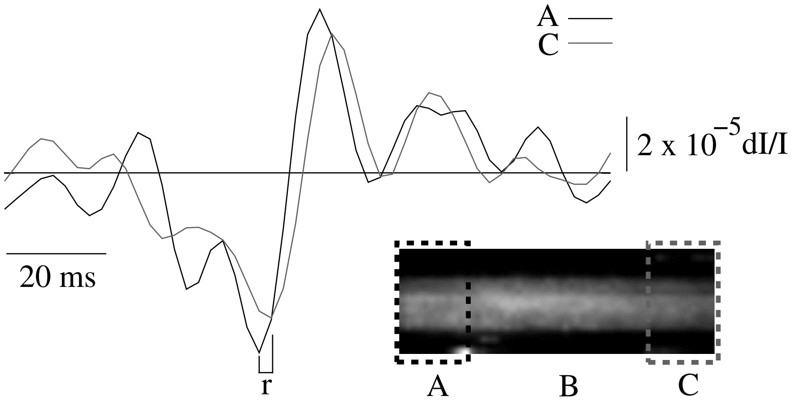

Figure 3.7: The nerve image shown in the upper panel was divided into three regions, A, B, and C with the middle region (B) twice the size of the outer two regions (A, C). The black line represents the leftmost region (A) and the gray line represents the rightmost region (C). The differentiated optical response was plotted for the leftmost region and the rightmost region. The left region leads the response verifying that the action potential propagates from left to right. The propagation velocity was calculated to be 2.57 m/s for the rising phase (r).

micrometers and temporal resolution on the order of milliseconds, a combination that exceeds current imaging techniques.

3.2.7 Irregular Cell Orientation

Imaging the lobster nerve provides relatively simple experiments and data interpretation because the physiological noise is low and the cells are oriented in the same direction. Imaging *in vivo*, however, introduces complexities from random cell orientation and dendritic, somatic, and glial activation. In order to optimize our birefringence imaging techniques before employing them *in vivo*, we confronted random cell orientation by tying the nerve in an overhand knot and imaging the change in polarization using transmitted light. Our measured EPR signals before and after the imaging window confirm that the action potential propagates through the knotted portion of the nerve. The spatially resolved image of the knot is shown in Figure 3.8(A). Since

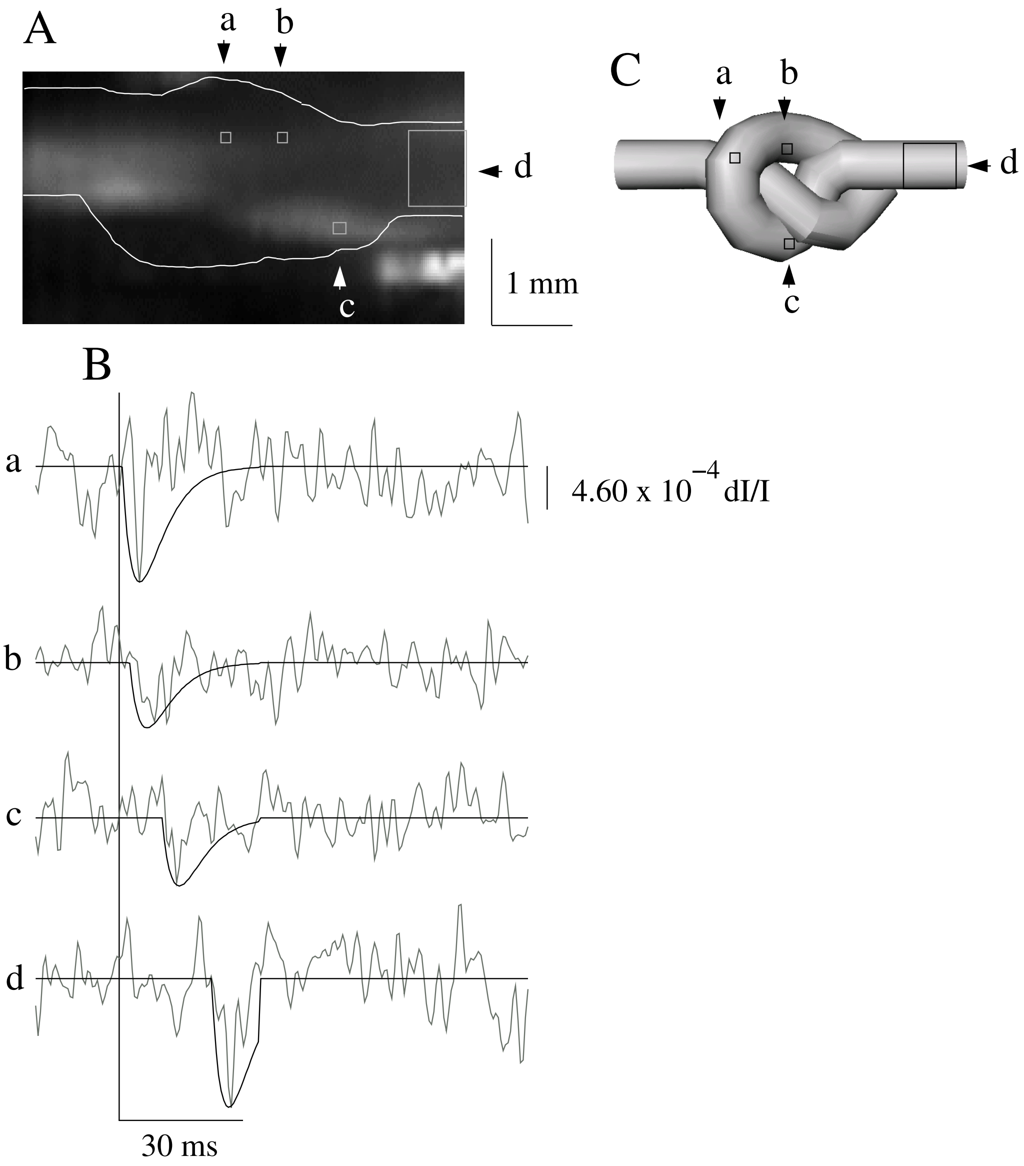

Figure 3.8: Panel (A) is an image of the transmitted light averaged over time with the nerve tied in an overhand knot. The solid black lines in (B) are fit to the raw data, shown in gray, using Equation 2.2. The time component confirms that the action potential first passes through pixel a, then through pixel b, following in pixel c and finally through pixel d which is the expected course of the action potential according to the geometry of the knot as mapped out in (C).

the orientation is difficult to decipher, Figure 3.8(C) shows a spatial map of the knot. We extracted polarization signals from specific regions in the knotted nerve and fit them to our temporal model (Figure 3.8(B)). Recall that the strongest signals arise when the incident light is polarized at 45 degrees with respect to the nerve bundle (Cohen et al., 1968; Yao et al., 2005). Signals from different regions within the nerve were fit to Equation 2.2 using a least squares fit. The signal in region (a) arose a couple of milliseconds after the stimulus from the underlying straight portion of the nerve where the light was incident at 45 degrees. The signal in region (b) shows a later response from region (a). Region (c) physically follows region (b) and the optical signal in (c) appears later than the optical signal in (b). The latency of the signal in region (d) shows that the action potential propagates through the entire knot. Each region revealing a response had incident light oriented 45 degrees with respect to the nerve bundle (Schei et al., 2008). These experiments confirm that when the sample contains processes with different orientations, the polarization signals are still present and demonstrate the expected latency according to the physical position. Although, the signals are smaller and are observed from specific regions of the nerve where the majority of the fibers are oriented 45 degrees with respect to the light. In theory, if the orientation of polarized light was rotated across different angles, different areas of the nerve would elicit signals.

3.3 Conclusions

In both transmission and reflection imaging modalities there was a clear decrease in polarized light corresponding to the action potential (Figure 3.2). The amplitude of the evoked signal in reflection mode, however, was about one third the amplitude of the signal observed in transmission mode. This smaller reflected signal may be due to fewer photons both changing polarization and scattering a full 180 degrees. In transmission mode imaging, many photons may be changing polarization while undergoing fewer scattering events, contributing to a larger response (Schei et al., 2008). While there is a distinct decrease in reflected polarized light corresponding to electrical activation, it is crucial to optimize the imaging techniques by utilizing procedures with good extinction coefficients and using non-coherent light sources in order to extract the small reflected changes in polarization.

Using a camera to both spatially and temporally image the change in polarized light, we created a movie of a propagating action potential. Optical imaging technologies using polarized light have spatial resolution on the order of tens of micrometers and temporal resolution on the order of milliseconds, a combination that exceeds current imaging techniques. This demonstrates the advantages of fast intrinsic optical imaging.

Chapter 4

Conclusions

Fast optical imaging has the potential to advance brain imaging with higher spatial and temporal resolution than other methods such as EEG or fMRI. Although fast optical scattering responses can be used to map highly localized neural activity, the signals remain small. Polarization measurements have been shown to be advantageous over scattering measurements since cross-polarizers reject many photons unaltered by neural activity (Cohen et al., 1968; Carter et al., 2004). The reduction of the background noise allows for an increase in dynamic range of the imaging system and improvement of signal contrast. These increased sensitivity measurements, in turn, increase the signal-to-noise ratio. Further improvements will hinge, in part, on our ability to detect photons that are altered by neural activity and reject those photons not altered by neural activity. Using these techniques *in vivo*, however, adds additional complications not present in the lobster nerve such as random orientation of fibers and dendritic, somatic, and glial activation. Random cell orientation hinders

---

Portions of this chapter were published as: Schei, J.L., McCluskey, M.D., Foust, A.J., Yao, X.C., and Rector, D.M. 2008. Action potential propagation imaged with high temporal resolution near-infrared video microscopy and polarized light. *NeuroImage*, 40(3):1034-1043. and Schei, J.L. and Rector, D.M. 2009. Fast Optical Neurophysiology, chapter 10, pp. 223-243. *In* A.W. Roe (ed.), Imaging the Brain with Optical Methods. Springer, New York, NY.

the application of these techniques *in vivo*; however, our preliminary results using polarization techniques on a knotted lobster nerve support the advantages of using polarized light. When utilizing these imaging techniques *in vivo*, we could also make measurements along the polar angles of the Muller matrix to account for random cell orientation (Berezhnyy and Dogariu, 2004). By combining the different views and extracting common features in the signal across all angles, we could reduce the noise and characterize the signal more clearly.

4.1 In vivo Applications

Some efforts have been made to uncover fast optical signals in humans using noninvasive imaging techniques. Fast backscattering light intensity changes have been shown during motor stimulation (Steinbrink et al., 2000). Other optical imaging techniques using modulated light sources show signal phase delays after stimulation. Photon migration methods measure relative photon delays during stimulation paradigms (Gratton et al., 1997; Maclin et al., 2004). Optical detections of fast physiological changes *in vivo* are easily swallowed by background noise corresponding to glial, synaptic, and hemodynamic events. Better signal optimization is required in order for fast optical responses to be readily applied in noninvasive imaging. Additionally, special care must be taken to exclude artifacts from vascular pulsations and vasomotion.

4.2 Future Approaches

Intrinsic optical imaging techniques have evolved significantly in the past half century. While *in vivo* optical imaging techniques are rapidly gaining in popularity, these techniques typically use scattered light to record hemodynamic-related changes. Our research has focused on integrating polarization imaging techniques for *in vivo* imaging in order to measure optical signals resulting from neural activity. Thus far, we have shown that polarization imaging techniques can be utilized with irregular cell orientations. A more robust signal may be possible by decomposing the parameters of the Mueller matrix and then reconstructing the responses associated with the polarization changes. Although improvements were made by overcoming irregular cell orientation obstacles during optical imaging, other scattering events hinder the application of optical techniques *in vivo*. Somatic, dendritic, and glial activation may cause changes in optical activity, thus complicating the interpretations of the detected signal. Polarization optics increase the signal by an order of magnitude compared to the scattering signal; however, further increases in contrast are needed to measure optical responses consequential of electrical activity in fewer averages, especially when recording the signals noninvasively. Using modulated light sources or time-gated detectors would allow for photon path retracing and multi-depth imaging. Better noise reduction methods such as background subtraction and EKG and respiration artifact removal would further increase the contrast of the signal. With polarization imaging techniques, we have the potential to produce images with better simultaneous spatial and temporal resolution than other current imaging techniques. As we further explore the properties of light interactions with neural tissue, we step closer to noninvasive, high resolution optical imaging technologies.

Part II

Optical Hemodynamic Imaging

Chapter 5

Introduction

Neural activity utilizes energy resources and requires replenishment of metabolites through vascular dilation. During wake, cortical neurons usually have depolarized membrane potentials and exhibit frequent spontaneous action potentials, requiring an increased metabolic delivery to activated tissue and causing blood vessels to dilate. Quiet sleep (QS) is characterized by alternating membrane potential between a depolarized and hyperpolarized state. The hyperpolarized state has a lower membrane potential and exhibits few action potentials, which may be less metabolically demanding.

We can measure hemodynamic activity as a consequence of neural activation using spectroscopic techniques. Additionally, implantable optical technologies provide measurements of cerebral hemodynamic activity from freely behaving animals without movement constraint or anesthesia. We investigated the changes in metabolic deliv-

---

Portions of this chapter were published as: Schei, J.L., Foust, A.J., Rojas, M.J., Navas, J.A., and Rector, D.M. 2009. State-dependent auditory evoked hemodynamic responses recorded optically with indwelling photodiodes. *Applied Optics* 48:D121-D129. and Schei, J.L. and Rector, D.M. Assessment of network states: Local hemodynamics. *Topics in Medicinal Chemistry* (in press).

ery following neural stimulation across wake and sleep states, and following sleep deprivation.

5.1 Synaptic transmission

Neurons conduct signals through electrochemical impulses along processes extending from the cell body. Communication between neurons takes place at synapses using either electrical or chemical signal transduction. Synaptic activity utilizes energy resources and initiates delivery of metabolites through increased regional blood flow and volume.

5.1.1 Electrical Transmission

Electric transmission provides instantaneous signal conduction between neurons through gap junctions, conduits of hemichannels that span the two cells. Gap junctions open in response to cellular depolarization, directly transmitting current to the postsynaptic cell proportional to the presynaptic signal. These signals can occur bidirectionally since electrical transmission relies on passive charge spread in the synapse.

5.1.2 Chemical Transmission

Chemical transmission is another means by which signals are transmitted between neurons. The location of transmission is called the synaptic cleft, a small space between between the presynaptic cell and postsynaptic cell. The presynaptic cell contains vesicles filled with neurotransmitters, chemicals that bind to specific postsynaptic cell receptors. As the membrane depolarizes, calcium-gated ion channels open, allowing an influx of calcium ions into the presynapse. The increased intracellular calcium concentration causes the vesicles to fuse with the presynaptic membrane, opening the vesicles and releasing neurotransmitter into the synaptic cleft. The neurotransmitter diffuses in the synaptic cleft and some molecules bind to specific receptors on the postsynaptic cell membrane. The neurotransmitter-receptor binding activates the postsynaptic cell by opening or closing ion channels. The neurotransmitter molecules are eventually released from the receptors and are either reabsorbed by the presynaptic cell or broken down. Since this process is complex compared to electrical transmission, chemically transmitted signals propagate slower compared to electrically transmitted signals. However, chemically transmitted signals have more variability in the signaling type and can produce more complex behavior.

An excitatory postsynaptic potentials (EPSP) is a depolarization of the postsynaptic membrane following chemical transmission. The depolarization occurs when ion channels open and positively charged ions flow into the cell. An inhibitory postsynaptic potential (IPSP) is a hyperpolarization of the postsynaptic membrane following chemical transmission. This can occur by either positively charged ions flowing out of the cell or negatively charged ions flowing into the cell. Both excitatory and inhibitory postsynaptic potentials are graded responses, and the summation may be temporal or spatial. Temporal and spatial summations are dependent on the time constant and length constant of the neuron, respectively. The membrane potential must reach a threshold in order to generate an action potential in the postsynaptic neuron.

5.2 Field Potentials

Synaptic activity elicits changes in ionic current in the surrounding intracellular and extracellular regions. These transient ionic currents cause changes in electric potential and extracellular recordings of synaptic activity measure field potential. Extracellular recordings during an EPSP show an increase in electric potential while an IPSP show a decrease in electric potential (Niedermeyer and Da Silva, 2005).

5.3 EEG and ERP Recordings

Synchronous synaptic activity produces large changes in electric potential that can be measured by surface electrodes placed on the cortex or the scalp. This measurement system is referred to as electroencephalography (EEG) (Berger, 1929). Evoked response potentials (ERPs) are measurements of the electric potential following a given stimulus. ERPs have typically been used in sleep research since they show state-dependent responses and can be used to study mechanisms of sleep and repercussions of sleep disruption (Colrain and Campbell, 2007). In our studies, we measure ERPs from the auditory cortex following auditory stimulation. In addition, we use optical imaging techniques to measure evoked hemodynamic responses following stimulation and investigated the coupling under different vigilant states.

5.4 Cerebral Blood Supply

The brain constitutes about 2% of total body weight; however, it consumes approximately 20% of delivered oxygen (Rolfe and Brown, 1997). Oxygenated blood leaves the heart through the aorta and travels to the brain through the common carotid arteries ascending in the neck. The arteries branch into cerebral arteries to deliver nutrients to tissue. The arteries branch into smaller diameter arterioles. Arteries and arterioles control blood flow through muscular contractions. Arterioles branch further into capillaries which are small in diameter, allowing blood cells to pass single-file. The capillary walls are thin and allow oxygen and other chemicals to diffuse into the surrounding tissue. Capillary networks extend throughout tissue to supply nutrients and remove waste products. These networks converge into larger diameter venules and eventually larger diameter veins to carry deoxygenated blood back to the heart. Venules and veins do not contract; rather, they modulate blood return passively using gravity and valves to prevent blood ebbing.

5.4.1 Autoregulation

Blood perfusion to the brain is tightly regulated in order to adequately maintain nutritional supply to the tissue, despite variations in blood pressure, through a process called autoregulation. Changes in systemic blood pressure cause arteries and arterioles to contract or dilate, regulating the mean arterial pressure. During periods of low blood pressure, such as sleep, autoregulation causes arteries to dilate, preventing tissue ischemia. During periods of high blood pressure, such as exercise, arteries contract, preventing hyperemia and potential tissue damage (Strandgaard and Paulson, 1984). Autoregulation is also modulated by metabolic changes (Aaslid et al., 1989). Changes in the partial pressure of carbon dioxide, partial pressure of oxygen, and pH contribute to vessel constriction and dilation. This process is integral in maintaining cerebral blood delivery and protecting against ischemia and hyperemia, which could lead to tissue damage.

5.4.2 Functional Hyperemia

During rest, oxygen supply to brain tissue exceeds oxygen consumption (Buckweitz et al., 1980). Regional changes in metabolic activity require fluctuations in regional blood delivery, balancing metabolic demand with blood supply. Increased neural activity increases the cerebral metabolic rate of oxygen and decreases the partial pressure of oxygen. This causes a local increase in local cerebral blood flow to replenish metabolic resources in the region (Roy and Sherrington, 1890; Fox et al., 1988).

However, the oxygen delivery rate is larger than the consumption rate (Hoge et al., 1999; Uludag et al., 2004; Masamoto and Tanishita, 2009), perhaps as a protection mechanism. While these studies investigated functional hyperemia in awake humans, changes in vigilance state alter metabolic delivery and consumption rate. During wake, spontaneous neural activity expends energy resources and blood vessels dilate to increase blood flow and volume to replenish metabolites. Physical limits in vascular dilation may decrease vessel compliance and limit blood delivery during wake. Sleep is less metabolically demanding and may serve to restore vascular compliance. In order to investigate state-dependent responses, we used optical imaging techniques to measure evoked hemodynamic responses in freely-behaving animals.

5.4.3 Neurovascular Coupling

The coupling between neural activation and functional hyperemia, termed neurovascular coupling, is not direct. Rather, a complex process of reactions couple these two responses. Astrocytes, a type of glia cell, reside in close proximity to synapses and blood vessels. Astrocytic endfeet processes project to arterioles and capillaries. Neural activation leads to a release of different chemical agents such as adenosine, nitric oxide, and COX-2-derived prostanoids which contribute to vasodilation and increase cerebral blood flow. In addition, neural activity releases glutamate from the synaptic terminal which generates astrocytic activity, releasing vasoactive substances that lead to blood vessel dilation and increased cerebral blood flow (Iadecola and Nedergaard, 2007; Jakovcevic and Harder, 2007). Neurons, astrocytes, and blood vessels work together to deliver metabolites during autoregulation and functional hyperemia. Several studies have investigated the coupling between ERPs and evoked hemodynamic responses (Devor et al., 2003; Franceschini et al., 2008); however, the preparations rely on anesthetized conditions, which may alter neurovascular coupling.

5.5 Auditory Evoked Response Potentials

Evoked responses can be used to measure modality-specific neural activity and the concomitant hemodynamic response. In our studies, we used auditory stimulation and measured evoked responses from the auditory cortex. This allowed for measurements of responses under freely-behaving conditions.

Sound pressure waves displace the tympanic membrane, or eardrum, which vibrate the ossicles, a series of bones within the ear. The ossicles move a membrane, called the oval window, that displaces fluid in the cochlea and deflects the auditory receptors, called hair cells. These receptors generate action potentials at a rate that is encoded to the sound intensity. Action potentials travel along the auditory nerve to the ventral cochlear nucleus and the superior olive in the brainstem. The pathways ascend to the inferior colliculus of the midbrain, travel to the medial geniculate nucleus of the thalamus, and project to the auditory cortex (Kandel et al., 2000).

Auditory ERPs elicit several components that arise from different regions along the auditory pathway. Early response components occurring 2-5 ms following the stimulus may originate from the brain stem; middle-latency response components occurring 8-15 ms may originate in the medial geniculate body of the thalamus and layer 4 of the primary cortex; and late-latency responses occurring 25-100 ms may have contributions from the medial geniculate body of the thalamus, hippocampus, primary auditory cortex, and secondary auditory cortex (Hall, 2006).

5.6 Sleep

The control and function of sleep are among the least understood brain phenomena, yet are vital physiological processes for human quality of life and performance. Economic stresses, societal pressures, and strenuous lifestyles have increasingly limited the amount of sleep that we obtain, resulting in disrupted sleep and sleep loss for many individuals (Bixler, 2009). Sleep deprivation may be the cause of numerous performance issues including driving and industrial accidents; social problems; and a wide variety of health detriments such as obesity, obstructive sleep apnea, diabetes, and heart disease (Orzeł-Gryglewska, 2010).

The prevailing scientific theory considers sleep a whole animal property, controlled by centralized sleep regulatory structures and measured by markers of whole animal behavior and neural tissue physiology. Sleep onset is strongly influenced by two factors: a homeostatic pressure to sleep that builds up during wakefulness and dissipates during sleep, and a 24 hour oscillatory circadian rhythm that drives sleep (Achermann and Borbely, 2003). Correlates of sleep, and repercussions of sleep deficit, are measured by sleep latency, EEG spectral power, global metabolic levels, and cognitive task performance (Belenky et al., 2003; Borbély et al., 1981; Friedman et al., 1979; Tassi et al., 2006; Buchsbaum et al., 1989; Madsen and Vorstrup, 1991). However, these parameters do not provide a direct causal mechanism for the occurrence of sleep in the brain.

Under normal situations, most land-based animals exhibit consolidated, whole-body sleep patterns because it is most economical for an organism to obtain sleep for the entire body during niche appropriate times when activities, such as foraging, are not productive. However, recent evidence shows that sleep is not necessarily a global brain event, especially when niche appropriate sleep is not possible. Rather, sleep-like characteristics may manifest in localized areas asymmetrically distributed across the brain (Krueger and Obäl Jr, 1993; Rector et al., 2005b). Concepts of local sleep require new markers to define wake- and sleep-likes states. During wake, neurons are depolarized and exhibit frequent, spontaneous action potentials while during QS, neurons oscillate between depolarized and hyperpolarized states (Steriade et al., 2001). Evoked responses to low intensity stimuli exhibit different characteristics based on cortical state which are low amplitude during the depolarized, wake-like state and high amplitude during the hyperpolarized, sleep-like state (Rector et al., 2005b; Massimini et al., 2003).

In response to the vast changes in neural activity across wake and sleep, vascular dynamics allow for sufficient metabolite delivery to activated tissue regions, replenishing energy resources. Depolarized states may be highly metabolically demanding since the membrane potential greatly exceeds the resting membrane potential, many spontaneous action potentials occur, and ATP is utilized by the sodium-potassium pumps to restore ionic gradients. Conversely, hyperpolarized states may be less metabolically demanding since the membrane potential is closer to the potassium equilibrium potential and ATP utilization from the sodium-potassium pumps is reduced. During the depolarized state, blood vessels expand to deliver metabolic resources while during the hyperpolarized state, blood vessels may be allowed to relax and increase compliance due to a decreased metabolic demand. We hypothesize that neurovascular restoration may be one function of sleep such that vascular compliance is low during the depolarized state and high during the hyperpolarized state.

During QS delta rhythms, cortical tissue membrane potential oscillates between depolarized and hyperpolarized states. If the hyperpolarized state is indeed sleep-like, then QS could be considered a consolidated, niche appropriate period of synchronous sleep. Under conditions of extended use, sleep restriction, or sleep deprivation, niche appropriate rules for whole-organism sleep could break down and the need for sleep may manifest in any part of the cortex that has experienced exertion (Krueger et al., 2008). When an animal cannot conform to niche appropriate sleep, we submit that other mechanisms must ensure brain homeostasis to circumvent risk of tissue trauma. For example, reticular activating systems may keep cells in the depolarized state when the animal needs to attend to external stimuli, but this can only be maintained for a limited time before detrimental consequences may occur. Therefore, local sleep mechanisms might provide a means for sleep and homeostasis when central mechanisms are overridden.

In order to investigate the metabolic consequences of sleep, we combined optical imaging technologies with electrophysiology to simultaneously measure hemodynamic responses elicited by evoked neural activity within the auditory cortex. Both the evoked neural and hemodynamic responses show state-dependent changes (Schei et al., 2009) which can be used as markers of sleep and indicators of tissue state. If sleep allows for vascular compliance restoration and metabolic replenishment, then optical techniques can be used to record hemodynamic responses and serve as a measure of tissue state. Since vessels may be more compliant during sleep, we would expect a larger evoked hemodynamic response to external stimulation during sleep. Conversely, waking activity may expand vessels, making them less compliant and resulting in smaller evoked hemodynamic responses. Transient changes in local metabolic activity may provide an index of prior neural use, which can link metabolic markers with predictors of task performance in order to better understand performance degradation with increased time-on-task.

5.6.1 Electrophysiological Markers of Sleep

Sleep is inferred from a variety of measures including electroencephalograms (EEG), electromyograms (EMG), brain temperature, behavior, posture, and heart rate. Correlates of whole-animal sleep are used to characterize whole-animal epochs (usually less than one minute) as being in a particular state and aggregates of epochs identify quantitative measures of sleep such as latency, intensity, frequency, and duration. These measures, combined with subjective measures, such as self-reported sleep quality, are used in clinical diagnostics and studies determining normal sleep, the consequences of sleep deprivation, and the implications of sleep disorders. While indirect measures of sleep are useful in a clinical setting, this top-down approach is limited by the inference of sleep since the measurements are consequences of sleep, or lack thereof, and not direct measures. Additionally, under many sleep pathologies, the standard markers of whole animal sleep no longer fit standard definitions, making interpretation difficult (Mahowald and Schenck, 2005).

In order to explore mechanisms of sleep localized within cortical networks, we examined evoked responses from the auditory cortex of rats under freely behaving conditions across a 24 hour period. Auditory stimulation allows for periodic measurements of cortical state under freely behaving conditions, without significantly disturbing normal sleep patterns (Phillips et al., 2011). We recorded ERPs by implanting a blunted stainless steel screw electrode over the auditory cortex of four rats and measuring potential differences from a reference electrode placed over the occipital lobe. Electrocardiographic activity (EKG) and electromyographic activity (EMG) were recorded using two insulated stainless steel wires, with 1 mm exposed ends, situated next to the thoracic cavity and in the neck muscle, respectively (Schei et al., 2009). Data were acquired using a custom-built data system that amplified (x1000), filtered (0.1 Hz - 3.2 kHz), and digitized (10 kHz) the signals (Rector and George, 2001).

We identified animal state for each 2 second epoch using a cluster cutting algorithm based on EEG Delta power and EMG power. Clusters of data points separated animal state such that high EMG power and low EEG Delta power corresponded to wake; low EMG power and high EEG delta power corresponded to QS; and low EMG power and low EEG Delta power corresponded to rapid eye movement (REM) sleep

(Rector et al., 2009a). Following cluster cutting, we visually confirmed each epoch state using the physiological signals and video camera images.

To measure electrical activity from cortical networks, we stimulated the animal using a train of 5 speaker clicks (10 Hz, 64 dBa, 2-13 s ISI) and generated ERPs in response to auditory stimulation in freely behaving animals over a 24 hour recording period. Two recordings were conducted for each animal and stimuli were sorted by state and averaged across each 24 hour recording period. We identified the ERP components in terms of latency following the stimulus such that P1 occurred around 25 ms, and N1 occurred around 50 ms during wake and REM and around 100 ms during QS (Rector et al., 2009a; Knight et al., 1985). The P1 and N1 components of the localized ERP showed that during periods of QS the amplitude and area were larger than those during wake or REM sleep (Rector et al., 2005b; Schei et al., 2009; Rector et al., 2009a; Knight et al., 1985) (Figure 8.1, Mann-Whitney U-test, $p < 0.05$). Furthermore, ERPs showed sleep-like responses as a function of prior neural use, that is, the longer the period of prior low amplitude wake-like responses, the higher the probability for large amplitude sleep-like responses, independent of whole-animal state (Rector et al., 2005b). Prolonged periods of waking or high neural activity may transiently drive the cells into the hyperpolarized state. In the hyperpolarized state, neurons exhibit fewer spontaneous action potentials (Steriade et al., 2001; Vyazovskiy et al., 2009) and may be less metabolically demanding, as discussed above. Thus, if the sleep-like, hyperpolarized state is less metabolically demanding, then it is possible that tissue which experiences high use may have a high probability of entering a hyperpolarized state to protect it from a metabolic deficit.

During QS periods, synchronous delta rhythms are indicative of cortical cell membrane potential oscillation between a hyperpolarized and depolarized state (0.3-3 Hz) (Steriade et al., 2001; Massimini et al., 2003). The ERP amplitude correlates to the cellular membrane potential where the hyperpolarized state elicits large amplitude, sleep-like ERPs and the depolarized state elicits small amplitude, wake-like ERPs (Rector et al., 2005b; Massimini et al., 2003; Rosanova and Timofeev, 2005). Since consolidated QS periods with delta rhythm may be a niche appropriate mechanism allowing for whole animal sleep at appropriate times, where cells hyperpolarize, controlled by subcortical structures, cortical column resources could be restored during QS. If external stimuli are best perceived during the depolarized, wake-like state (Phillips et al., 2011), then the delta rhythm may allow periodic attention for arousal and behavioral responses since neuronal spiking is more prevalent during the depolarized state (Steriade et al., 2001; Vyazovskiy et al., 2009). Furthermore, the delta rhythm oscillation between hyperpolarized and depolarized states would be important to achieve cellular restoration during hyperpolarization while providing an opportunity for arousal during depolarization, with implications for survival mechanisms to escape immediate danger.

5.6.2 Metabolic Markers of Sleep

Neural activation elicits a blood, or hemodynamic, response concomitant with electrical activity, typically associated with the BOLD (blood oxygen level-dependent) response measured using functional magnetic resonance imaging (fMRI) techniques. During waking activity, neural tissue exhibits frequent, spontaneous action potentials, utilizing energy resources and requiring increased vessel diameter and blood flow to replenish metabolites. Prolonged waking periods may stretch vessels in response to high metabolic demand and cause them to approach compliance limits, where further dilation in response to neural activation is limited. If vessels approach compliance limits while neural activity remains in high demand, then cells may enter a sleep-like state in order to reduce metabolic demand, replenish metabolites to the tissue, and restore vascular compliance.

Sleep may serve to restore vascular compliance and replenish metabolites to tissue, and optical techniques can be used to record hemodynamic responses and serve as a measure of local tissue state.

Chapter 6

Spectroscopy

Optical imaging techniques can be used to assess relative changes in oxygen concentration in hemoglobin, known as pulse oximetry. Attenuation of light through tissue is described by the modified Beer-Lambert law (Equation 6.1) and changes in the amount of light collected are dominated by changes in light absorbed by hemoglobin while changes in scattered light are negligible (Roggan et al., 1999; Schei et al., 2009). We used time-resolved spectroscopic techniques to measure hemodynamic responses following neural stimulation.

6.1 Light Absorption

Neural activation elicits changes in local oxygenated hemoglobin concentrations and blood volume. These changes can be measured using optical techniques which rely on the absorption properties of blood (Pittman, 1986). For short distances we can assume that scattering is negligible and attenuation of light through a medium can

---

Portions of this chapter were published as: Schei, J. L., Foust, A. J., Rojas, M. J., Navas, J. A., and Rector, D. M. 2009. State-dependent auditory evoked hemodynamic responses recorded optically with indwelling photodiodes. *Applied Optics*, 48(10):D121-D129.

be described by the Beer-Lambert Law

$$I = I_0 10^{-\mu_\lambda d}, \tag{6.1}$$

where μ_λ is the absorption coefficient and d is the path length of light. Considering only the oxyhemoglobin and deoxyhemoglobin components, the absorption coefficient can be written as a linear combination of the oxy- and deoxyhemoglobin absorption extinction coefficients, ϵ_λ, the fractional oxygenated hemoglobin saturation, S, and the total hemoglobin concentration, c,

$$\mu_\lambda = S\epsilon_{\lambda_{HbO_2}} c + (1-S)\epsilon_{\lambda_{Hb}} c. \tag{6.2}$$

Changes in absorption are described as

$$\begin{aligned} A &= log(\frac{I_0}{I}) && (6.3) \\ A &= S\epsilon_{\lambda_{HbO_2}} cd + (1-S)\epsilon_{\lambda_{Hb}} cd. && (6.4) \end{aligned}$$

The sensitivity of absorption changes to oxygenated hemoglobin saturation can be calculated as

$$\frac{dA_\lambda}{dS} = \epsilon_{\lambda_{HbO_2}} cd - \epsilon_{\lambda_{Hb}} cd. \tag{6.5}$$

We solved for the total hemoglobin concentration and path length using Equation 6.4,

$$cd = \frac{A}{(S\epsilon_{\lambda_{HbO_2}} + (1-S)\epsilon_{\lambda_{Hb}})}. \tag{6.6}$$

The sensitivity of absorption to changes in oxygenated hemoglobin saturation as a function of wavelength is

$$\frac{dA_\lambda}{dS} = \frac{A(\epsilon_{\lambda_{HbO_2}} - \epsilon_{\lambda_{Hb}})}{(S\epsilon_{\lambda_{HbO_2}} + (1-S)\epsilon_{\lambda_{Hb}})}, \tag{6.7}$$

where $A = 0.7404$ for the example shown in Figure 8.2. This sensitivity curve is shown in top trace of Figure 6.1 for varying the initial oxygenated hemoglobin saturation conditions. At 660 nm wavelength, the optical signal becomes more sensitive to changes in deoxygenated hemoglobin at larger fractional oxygenated hemoglobin saturation.

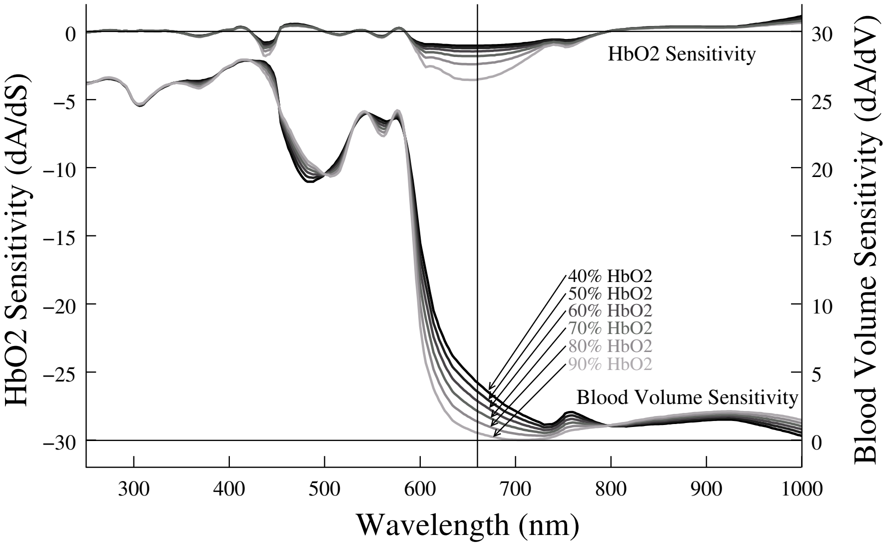

Figure 6.1: The top trace shows the sensitivity of the optical signal to oxyhemoglobin changes as a function of wavelength, described by Equation 6.7, for varying initial oxygenated hemoglobin saturation conditions. At 660 nm, the optical signal is more sensitive to changes in deoxyhemoglobin with higher oxyhemoglobin saturation. The lower trace shows the sensitivity of the optical signal to changes in blood volume for varying initial oxygenated hemoglobin saturation conditions. At 660 nm, the optical signal is less sensitive to changes in blood volume with higher oxyhemoglobin saturation, described by Equation 6.11. An inset of the hemoglobin absorption curve is shown with a line drawn at 660 nm.

In order to account for changes in blood volume, the absorption coefficient can be written as

$$\mu_\lambda = (1-V)\mu_{tissue} + V(S\epsilon_{\lambda_{HbO_2}}c + (1-S)\epsilon_{\lambda_{Hb}}c), \tag{6.8}$$

where V is the fractional blood volume to total volume and μ_{tissue} is the absorption coefficient of the tissue. The sensitivity of absorption to changes in blood volume can be written as

$$\frac{dA_\lambda}{dV} = -\mu_{tissue}d + S\epsilon_{\lambda_{HbO_2}}cd + (1-S)\epsilon_{\lambda_{Hb}}cd, \tag{6.9}$$

and the path length is

$$d = A\left[\frac{1}{(1-V)\mu_{tissue} + VS\epsilon_{\lambda_{HbO_2}}c + V(1-S)\epsilon_{\lambda_{Hb}}c}\right]. \tag{6.10}$$

The sensitivity of absorption to changes in blood volume becomes

$$\frac{dA_\lambda}{dV} = A\frac{(-\mu_{tissue} + S\epsilon_{\lambda_{HbO_2}}c + (1-S)\epsilon_{\lambda_{Hb}}c)}{(1-V)\mu_{tissue} + VS\epsilon_{\lambda_{HbO_2}}c + V(1-S)\epsilon_{\lambda_{Hb}}c}, \tag{6.11}$$

where $A = 0.7404$ for the example rat in Figure 8.2, $\mu_{tissue} = 2.63$ cm^{-1} (Cheong et al., 1990), $V = 5.2$ % (Leenders et al., 1990), and $c = 5.36$E-3 moles/liter (Prahl, 1999). We assumed that we are predominantly collecting photons traveling through gray matter, that the optical properties of gray matter are similar between human tissue and rat tissue, and that the hemoglobin concentration is similar to whole blood. A plot of the absorption sensitivity to changes in blood volume as a function of wavelength is shown in the bottom trace of Figure 6.1, varying the initial oxygenated hemoglobin saturation. At 660 nm, the higher the fractional oxygenated hemoglobin saturation, the less sensitive the signal is to changes in blood volume.

6.2 In Vivo Imaging

Light entered the cortex and was multiply scattered before being detected by the photodiode. The mean free path for neural tissue is approximately 5 μm - 0.1 mm (Taddeucci et al., 1996; Fukui et al., 2003). In our studies, the hemodynamic response was measured in terms of changes in 660 nm light. Due to the relatively high number of photons absorbed by hemoglobin at this wavelength, we assume that our signal is predominantly affected by changes in absorption rather than scattering (Roggan et al., 1999). Additionally, according to the hemoglobin absorption curve, deoxygenated hemoglobin absorbs ten times more 660 nm light than oxygenated hemoglobin.

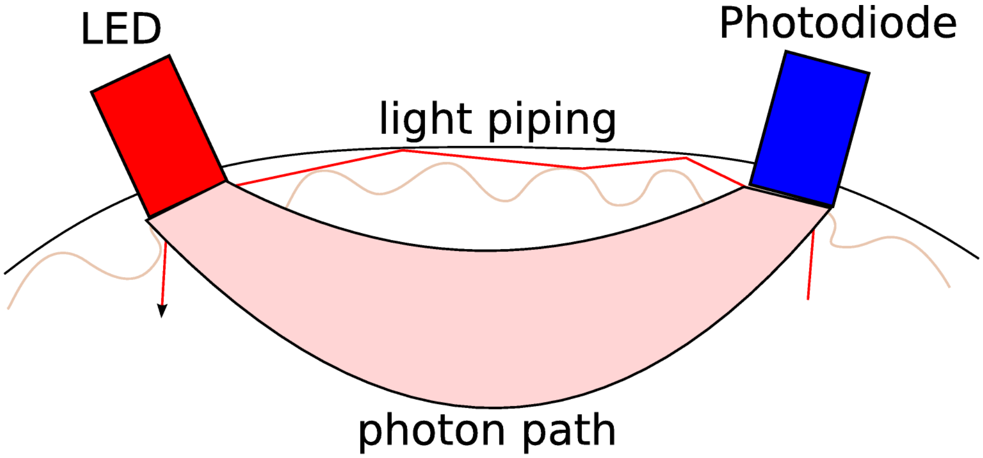

Figure 6.2: Model of light scattering within the cortex.

However, changes in oxyhemoglobin and deoxyhemoglobin concentrations are coupled with changes in blood volume and flow. Figure 6.1 shows the sensitivity of the optical signal to changes in tissue oxygen saturation (top) and to changes in blood volume (bottom) for varying initial oxygen saturation conditions. As the blood becomes more oxygenated, the optical response is more sensitive to changes in deoxygenated hemoglobin and less sensitive to changes in blood volume. Bulk brain tissue oxygen saturation is lower than arterial oxygen saturation; thus, we expect that our optical

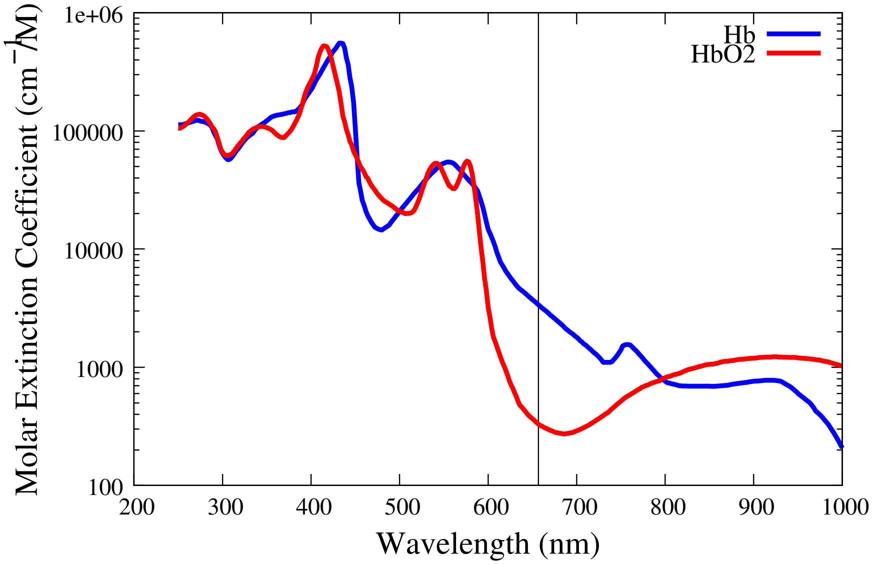

Figure 6.3: Oxygenated and deoxygenated hemoglobin absorption as a function of wavelength (Prahl, 1999). The black vertical line indicates the absorption at 660 nm, the wavelength of light used in these studies.

signal will be affected by a combination of changes in deoxyhemoglobin concentration and blood volume. Since we are limited to one wavelength, the deoxyhemoglobin and blood volume components cannot be separated and additional studies are needed using at least two wavelengths.

Chapter 7

Experimental Techniques

7.1 Hardware

We measured reflected light changes from the rat auditory cortex using an implanted 1 mm silicon photodiode (Figure 7.1(A), PC1-6, Pacific Silicon Sensors, Westlake Village, CA, USA) and a 660 nm light emitting diode (LED, Figure 7.1(B), 1.6 mW, B5b-436-30, Roithner Lasertechnik, GmbH, Vienna, Austria). We chose 660 nm light because LEDs at this wavelength provided the brightest illumination, which is necessary in order to collect a sufficient number of photons to extract the hemodynamic response with sufficient signal-to-noise. To reduce the LED size while maintaining high intensity output, we thinned the plastic casing of the LED to a width of 1 mm. A small drop of epoxy on the end of the LED acted as a lens to focus the light onto the cortex. The photodiode collected multiply scattered light from the cortex. To maximize light collection efficiency, we coupled the photodiode to a 1 mm thick plastic optical fiber encased in stainless steel hypodermic tubing which was in direct

---

Portions of this chapter were published as: Schei, J.L., Foust, A.J., Rojas, M.J., Navas, J.A., and Rector, D.M. 2009. State-dependent auditory evoked hemodynamic responses recorded optically with indwelling photodiodes. *Applied Optics* 48:D121-D129.

contact with the tissue (Figure 7.1(A)). Other methods form an optical window over the cortex, and use lens coupled imaging devices. By placing the optical fiber in contact with the tissue, we reduced photon loss within the free space between the dura and photodiode. The fiber was cut to 8 mm in length and polished prior to implantation.

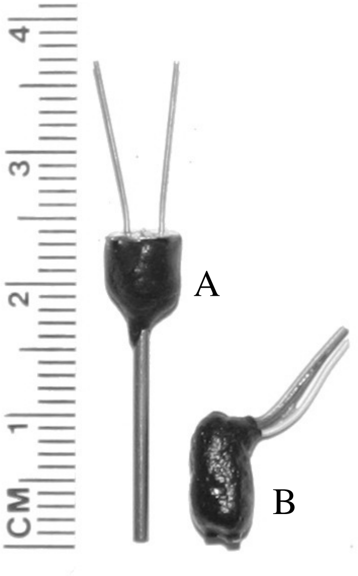

Figure 7.1: A 1 mm diameter photodiode (A) was coupled to a 1 mm optical fiber encased in hypodermic tubing and covered with black epoxy. The distal end of the optical fiber was cut to 8 mm length, polished, and placed directly in contact with the cortical tissue to collect light from the cortex. To illuminate the tissue with 660 nm light, a light emitting diode (LED, B) was cut down to a 1 mm width and covered with black epoxy.

7.2 Implantation

During initial surgical procedures, female Sprague-Dawley rats (250-300 g, Simonsen Laboratories, Gilroy, CA, USA, n = 4) were anesthetized using isoflurane gas mixed with pure oxygen. We delivered 5.0 % isoflurane for the initial induction and then reduced the concentration (2.3 % - 2.9 %) for the remaining surgical procedure. The anesthesia depth was monitored via the toe pinch reflex, electrocardiogram (EKG), and respiration. All procedures were approved by the Washington State University Animal Care and Use Committee (IACUC). The body temperature was maintained at 37° C (± 0.5° C) using a heating pad and rectal thermometer probe and the heart rate and respiration rate were continuously monitored using subcutaneous pin electrodes. After shaving the rat's scalp and fixing the head in a stereotaxic frame, we made an incision down the midline exposing the skull. We retracted the skin, removed the fascia, and detached the temporalis muscle from the skull in order to expose the area over the auditory cortex. Eight 0.9 mm diameter holes were drilled around the skull using a dental drill and blunted stainless steel screws were inset making contact with the cortex without applying pressure or puncturing the dura. One frontal screw and one parietal screw measured EEG, one occipital screw served as a ground reference (Figure 7.2, solid circles), and the remaining screws secured the headstage in place (Figure 7.2, open circles). A 1.4 mm hole was drilled approximately 3 mm caudal to bregma, over the thinned temporal ridge, for insertion of the photodiode and another 1.4 mm hole was drilled approximately 3 mm caudal to the photodiode for insertion of the LED. Two insulated stainless steel wires with 1 mm exposed wire ends were placed in the thoracic cavity and neck muscles to measure the heart rate (EKG) and muscle activity (EMG), respectively. A miniature plug connected wires from the LED, photodiode, and recording electrodes and all components were secured using dental cement. Flunixin (1.1 mg/kg) was delivered subcutaneously and a liberal amount of antibiotic ointment was applied to the base of the headstage each day for 3 days following the recovery. Rats were allowed a 2 week recovery period before recording.

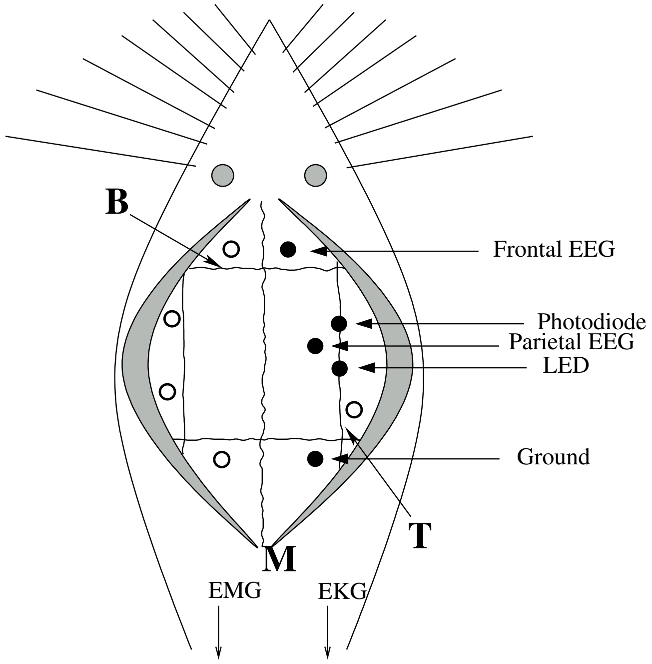

Figure 7.2: Rats were implanted with a light emitting diode (LED) and photodiode pair which were placed over the right temporal ridge (T) and 3 mm caudal to Bregma (B) with 3 mm between the LED and photodiode. To assess behavioral state, EEG screw electrodes were implanted in the frontal and parietal lobes and a ground reference screw was placed in the occipital lobe (solid circles). Five additional screws served as anchors for the headstage (open circles). Neck EMG and EKG wires recorded muscle activity and heart rate.

7.3 Recordings

For freely moving conditions, rats were placed in a 26.5 cm x 26.5 cm x 34 cm acrylic chamber and tethered using a 55 cm long cable and swivel commutator. Signals were amplified, (AC photodiode x200, DC photodiode x1, EEG x1000, EKG x1000, EMG x1000), filtered from 0.1 Hz to 3.2 kHz and digitized at 10 kHz using custom built hardware (Rector and George, 2001). To reduce noise in the recordings, the frontal EEG screw electrode was grounded.

In order to generate a substantial hemodynamic response, we stimulated the cortex through a 10 Hz burst of 5 speaker clicks (~64 dB) delivered at random intervals between 2 and 13 seconds throughout the recording. Although we recorded from a large area of cortex, we provided a relatively specific stimulus and therefore assume that the evoked electrical and optical responses were primarily due to auditory stimulation, despite volume conduction (Penfield and Jasper, 1954). Rats were recorded under freely moving conditions, during wake and sleep states, with food and water available *ad libitum*. In order to achieve adequate sleep, we recorded rats for 24 consecutive hours. Wake/sleep states were sorted into 2 second epochs and scored based on EEG delta power (0 - 3 Hz) and EMG activity. Wake characteristics included high frequency, low amplitude EEG signals along with large amplitude, variable EMG signals. Quiet sleep (QS) states showed low frequency, high amplitude EEG signals along with a constant moderate amplitude EMG from sustained muscle tone. Rapid eye movement (REM) sleep exhibited high frequency, low amplitude EEG, similar to wake, with a nearly flat EMG due to muscle atonia (Rector et al., 2009a). Two 24 hour recordings were averaged together in order to improve signal-to-noise in the optical signal. An anesthetized state was achieved using a mask to deliver isoflurane gas mixed with oxygen at high concentrations (5.0 %) for initial induction. The concentration of isoflurane was then reduced to ~2.0 % before experimentation to maintain a deep anesthetic plane and was monitored by muscle relaxation, respiratory rate, evoked electrical responses, and burst suppression ratio (BSR). The BSR, defined as the sum of the silent periods over the total epoch time, was 0.74 ± 0.05. We averaged together 500 stimuli and then allowed the rat one week to recover before the next recording.

7.4 Data Analysis

All data were analyzed using Octave, an open source data analysis package. The evoked electrical and optical responses were sorted by state and averaged together across stimuli. The evoked electrical response was recorded from the parietal screw electrode, closest to the auditory cortex. The amplitude of the evoked electrical response potential (ERP) was reported as the amplitude difference between the first peak (P1) and first trough (N1) components of the first ERP

To assess evoked changes in the hemodynamics due to neural activation, the AC optical signal was divided by the DC optical signal reporting fractional changes (dI/I) and then inverted so that an increase in signal corresponded to an increase in blood volume/deoxyhemoglobin. The signal peak was defined as the first local maximum following stimulation and the trough was defined as the local minimum following the peak. The peak and trough amplitude were measured in referenced to baseline activity. In order to average across multiple recordings, the optical responses during wake, QS, and REM were normalized to the QS peak. We chose QS because responses were most consistent in this state. Since the isoflurane recordings took place at a different time, these data were not normalized. Evoked electrical and optical response amplitudes and times were measured for 4 animals and the mean and standard error were calculated. Statistical significance was calculated using a Mann-Whitney test. In order to test the state-dependence of the neurovascular response, we plotted the ERP amplitude (P1-N1) versus the optical response amplitude (peak-trough) for each individual recording.

Chapter 8

State-Dependent Hemodynamic Responses

8.1 Optical Hemodynamic Imaging

Optical imaging of cerebral hemodynamic activity provides an index of neuronal activation and can be used as an indirect probe of neural processing and function. Several investigators have utilized optical brain imaging techniques (Mayhew et al., 2000; Berwick et al., 2002; Devor et al., 2003; Sheth et al., 2003; Chen et al., 2005; Dunn et al., 2005; Chen-Bee et al., 2007; Hillman et al., 2007; Jones et al., 2008), although animals typically remain anesthetized or restrained throughout the recordings. Alterations in conscious states, however, have profound effects on global cerebral perfusion (Braun et al., 1997), evoked electrical responses (Rojas et al., 2006; Rector et al., 2005b), and evoked hemodynamic responses (Berwick et al., 2002; Chen et al., 2005). How these different states affect neurovascular coupling is still not well under-

---

Portions of this chapter were published as: Schei, J.L., Foust, A.J., Rojas, M.J., Navas, J.A., and Rector, D.M. 2009. State-dependent auditory evoked hemodynamic responses recorded optically with indwelling photodiodes. *Applied Optics* 48:D121-D129.

stood. While some investigators have studied changes in the hemodynamic response between wake and anesthetized conditions (Berwick et al., 2002; Chen et al., 2005), the wake-like conditions are confined to restrained animals. In order to probe state-dependent neurovascular coupling, we measured changes in local cerebral perfusion across different states of consciousness under freely behaving conditions.

Sleep research has long postulated that sleep leads to restoration of neural tissue (Krueger and Obäl Jr, 1993); however, direct causal evidence for this theory remains elusive. Previous sleep studies have shown a decrease in metabolic activity during quiet sleep (QS) compared to wake and an increase in metabolic activity during rapid eye movement (REM) sleep compared to QS (Braun et al., 1997), for review see (Maquet, 2000; Zoccoli et al., 2002). Additionally, evoked electrical response potentials (ERPs) are larger during QS than wake (Rojas et al., 2006; Rector et al., 2005b) and evoked hemodynamic signals are larger in amplitude under wake conditions than anesthetized conditions (Berwick et al., 2002; Chen et al., 2005). Other optical studies in humans show slow (on the order of minutes) net increases in oxygenated hemoglobin and deoxygenated hemoglobin during wakeful stimulation and net decreases during sleep stimulation (Hoshi and Tamura, 1993).

In order to systematically investigate evoked cerebral hemodynamic responses during different conscious states, we measured the evoked electrical response along with the evoked hemodynamic response using 660 nm light reflected from the rat auditory cortex following auditory stimulation during wake and sleep of freely behaving animals and during isoflurane anesthesia.

8.2 Evoked Electrical Responses

Figure 8.1 shows a sample of the ERPs across state from one rat. Under all conditions, the ERP was largest for the first stimulus and subsequent ERPs corresponding to subsequent stimuli were smaller. As previously reported, ERPs during QS were significantly larger in amplitude compared to wake. REM sleep ERPs were similar in size and shape to the ERPs during wakefulness (Rector et al., 2005b). Under isoflurane anesthesia, a small evoked response appeared after the first stimulus followed by a large, elongated, and late peak due to averaged burst activity synchronized to the stimulus. The average of the bursts forms a response that appears similar to a large and late evoked response, but the underlying mechanisms that generate the burst is different (Rojas et al., 2006). An example of synchronized individual bursts and the burst average are shown in the lower inset of Figure 8.1.

8.3 Evoked Hemodynamic Responses

Typical evoked hemodynamic responses from one rat across all states are shown in Figure 8.2. While some initial fast optical components may have been present, we did not collect a sufficient number of trials to resolve the fast signal (Rector et al., 2005a). This study focused on two components from the slower hemodynamic response. During wake, the optical signal showed an initial peak that occurred around 1.8 s followed by a successive trough at 3.3 s. During QS, there was a large increase in dI/I at 2.3 s and a decrease at 4.1 s. During this state, the signal was phase shifted where the peak and trough appear later compared to the other states. REM sleep exhibited a peak at 1.5 s followed by a trough at 3.3 s. Under isoflurane anesthesia, the evoked hemodynamic response had an initial increase at 1.6 s and a subsequent decrease at 3.2 s.

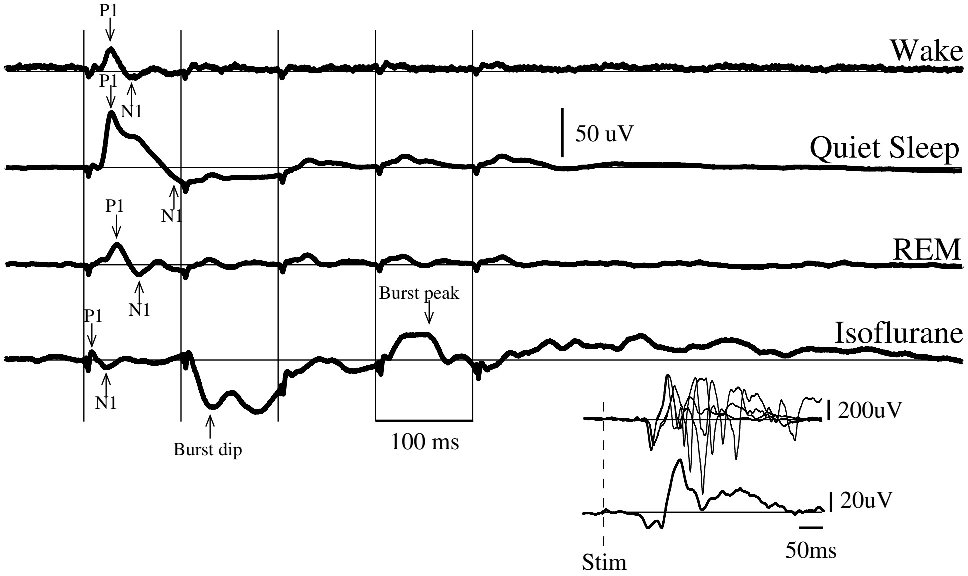

Figure 8.1: Sample evoked electrical response potentials (ERPs) from one animal for wake, sleep, and anesthetized states were averaged across stimuli and plotted across time. The vertical lines represent each stimulus in the burst. The ERP amplitude, measured from the first peak (P1) to the first trough (N1), was significantly larger during quiet sleep (QS) than during wake. During rapid eye movement (REM) sleep, the ERP was similar in amplitude to the ERP during wake. Under isoflurane anesthesia, a small amplitude ERP appeared after the first stimulus followed a late burst of activity synchronized to the stimulus. The lower inset panel demonstrates electrical recordings from a different rat using single click stimuli. The top trace shows several burst events that synchronize to the stimulus and are stacked on top of each other. The bottom trace shows the corresponding average of the bursts, which appears very similar to a late ERP, but is unrelated to mechanisms that underlie the ERP (Rojas et al., 2006). The dotted line indicates the time of the stimulus.

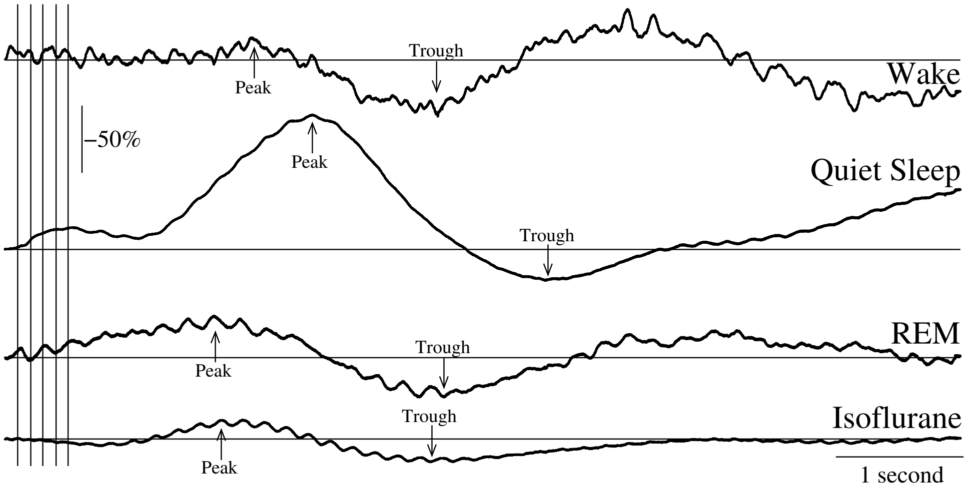

Figure 8.2: Inverted evoked hemodynamic responses were averaged across wake, sleep, and anesthetized states and plotted across time in this example from one rat. The vertical lines represent each stimulus in the burst. To compare sleep state related responses, the wake, quiet sleep (QS), and rapid eye movement (REM) sleep traces were normalized to the QS peak while the isoflurane trace was reported as fractional change from baseline, pre-stimulus conditions. An increase in the inverted signal corresponded to an increase in 660 nm light absorption (a decrease in reflected light) and an increase in deoxyhemoglobin/blood volume. The peak amplitude was larger during QS than wake and REM, but the trough amplitude did not significantly differ. Both the peak and the trough were shifted later in time during QS than wake, REM, and isoflurane.

Evoked hemodynamic responses across states for 4 animals are shown in Figure 8.3. The wake/sleep amplitudes were normalized to the QS peak for each rat. Note that the optical amplitude scaling was twice as large during QS (Figure 8.3(B)) than during wake (Figure 8.3(A)) and REM (Figure 8.3(C)). Since the isoflurane recordings took place on a different day than the wake/sleep recordings, the trace amplitudes were presented as changes from baseline conditions and the amplitudes are based on a different scale. The peaks and troughs in the responses were marked with arrows. The traces show similar trends in peak and trough amplitudes and times during each state along with the variability between animals.

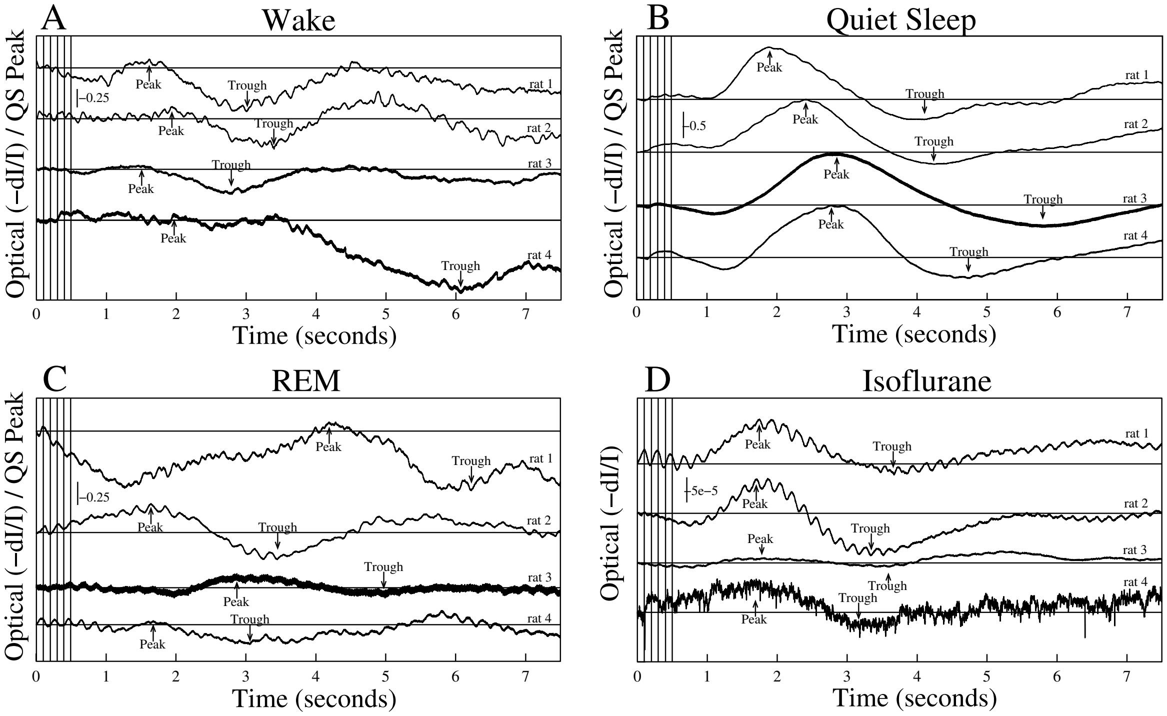

Figure 8.3: Hemodynamic response traces from 4 animals are shown for wake (A), quiet sleep (QS) (B), rapid eye movement (REM) sleep (C), and isoflurane (D). The peaks and troughs, marked by arrows, show the amplitude and timing trends. The variability between rats may be caused by different amounts of movement artifact and/or placement differences. During wake, rat 4 showed a large, late trough that may have been influenced by movement artifact. Rat 3 showed thicker traces in QS and REM, as well as rat 4 during isoflurane due to decreased signal -to-noise in these recordings.

Table 8.1: Mean and standard error values of the electrical and hemodynamic responses from four animals [a]

	Electrical	Optical			
States	ERP Amplitude	Peak Amplitude	Peak Time	Trough Amplitude	Trough Time
Wake	0.51 ± 0.085 [b]	0.11 ± 0.02[b]	1.66 ± 0.12	-0.61 ± 0.2	3.72 ± 0.76
QS	1.00	1.00	2.38 ± 0.22	-0.36 ± 0.05	4.62 ± 0.38
REM	0.486 ± 0.088[b]	0.16 ± 0.06[b]	2.50 ± 0.60	-0.33 ± 0.1	4.31 ± 0.73
Isoflurane	0.16 ± 0.029[b]	$6.3e-5 \pm 2e-5$	1.63 ± 0.029[b]	$-4.5e-5 \pm 2e-5$	3.34 ± 0.16[b]
Iso burst	1.44 ± 0.40				

[a] The evoked electrical response potential (ERP) amplitude (P1N1), normalized to quiet sleep (QS), was smaller during wake, rapid eye movement (REM) sleep, and isoflurane ($p < 0.05$) compared to QS. The isoflurane burst amplitude did not significantly differ from the QS ERP. As previously reported, the ERP amplitude during REM was not statistically different than wake. The hemodynamic response amplitudes during wake and sleep were normalized to QS while the hemodynamic response amplitude of the isoflurane response was reported as changes from baseline. During QS, the hemodynamic response peak amplitude was larger than wake and REM ($p < 0.05$), The QS trough, however, was not significantly larger than wake or REM. Both the QS peak and the trough occurred significantly later in time than isoflurane ($p < 0.05$).

[b] $p < 0.05$

8.4 Evoked Response Amplitudes

We compared the ERP amplitude, measured as the difference between P1 and N1 and normalized to QS, across states (Table 8.1). The ERP amplitude was significantly larger during QS than wake, REM and isoflurane ($p < 0.05$). As expected, the ERP amplitude did not differ between wake and REM.

We compared the hemodynamic response peaks and troughs across states by plotting the amplitude and time for each animal (Figure 8.4(A)). The mean amplitude and time from the 4 rats were plotted for each state along with the vertical and horizontal error bars, respectively. The peak amplitude was significantly larger ($p < 0.05$) during QS than wake or REM; however the trough amplitude did not significantly differ (circled data points, mean and standard error values shown in Table 8.1). Both

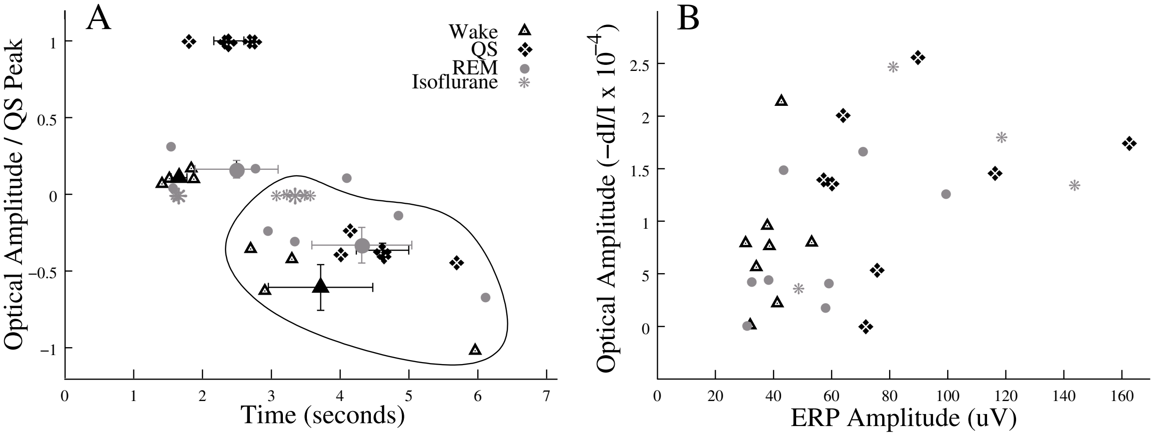

Figure 8.4: The peak amplitude versus time are plotted for all 4 animals across states (A). The wake/sleep responses were normalized to the quiet sleep (QS) peak while the isoflurane response was reported as changes from baseline. The mean peak amplitudes and times are plotted with vertical and horizontal standard error bars, respectively. During QS, the peak amplitude is significantly larger compared to wake and rapid eye movement (REM) sleep. The QS peak was shifted significantly later in time compared to isoflurane. The trough amplitude versus time are plotted for all 4 animals across states along with the mean and standard error (circled region). Unlike the peak, the QS trough amplitude did not significantly differ between wake and REM, but it occurred significantly later in time compared to isoflurane. A plot of the hemodynamic amplitude (peak-trough) versus the evoked electrical response potential (ERP) amplitude (P1-N1) for individual recordings is shown in B. Wake states exhibited lower amplitude ERP and hemodynamic responses while QS states exhibited larger ERP and hemodynamic amplitudes. Evoked responses during REM were similar in amplitude to wake responses, but experienced larger variations between animals. During isoflurane, the hemodynamic response was similar in amplitude to QS while the synchronized burst amplitudes was similar to QS ERP amplitudes.

the hemodynamic peak and trough during QS occurred later in time than during isoflurane ($p < 0.05$).

In order to illustrate the relationship between the ERP response and the hemodynamic response, we plotted the hemodynamic amplitude (peak-trough) versus the ERP amplitude (P1-N1) across each state (Figure 8.4(B)). During wake, both the ERP and hemodynamic amplitude were small compared to QS. During REM, there was a larger range of ERP and hemodynamic amplitudes but, on average, lower response amplitudes compared to QS. The ERP amplitude during QS was similar in amplitude to the burst activity during isoflurane anesthesia. Additionally, the hemodynamic responses were similar in amplitude.

8.5 Conclusions

Optical studies under freely behaving conditions allowed us to probe the processes involved in neurovascular coupling under wake, sleep, and anesthetized states. The ERP signals during REM sleep were nearly identical to those during wakefulness. While the averaged evoked hemodynamic responses were similar in time and amplitude, the individual hemodynamic responses experienced high variability in the signal, as evident by a lower a lower signal-to-noise ratio compared to QS. Under wakefulness, movement artifact may have contributed to the noise in the signal. The large, late trough in rat 4 may be residue of a strong movement artifact. During REM sleep, however, movement artifact does not contribute since animals experience muscle atonia, a characteristic of REM sleep. In rat 3, it was difficult to distinguish between deep QS and REM. As a result, the peak and trough in the REM hemodynamic response may have shifted later in time, having a time course similar to QS.

The ERP signal during QS exhibited a significant amplitude increase compared to the wake and REM states. The hemodynamic peak amplitude was significantly larger during QS, yet the trough amplitude did not significantly differ. The larger hemodynamic response during QS may be due to a lower initial blood perfusion baseline and a larger fractional change. During wake and REM there may be a larger degree of ongoing neuronal activity and a concomitant larger blood perfusion baseline, resulting in a smaller fractional change. Additionally, since blood flow decreases during quiet sleep (Braun et al., 1997), for review see (Maquet, 2000; Zoccoli et al., 2002), the larger amplitude hemodynamic response during QS may result from to blood vessels initially being in a less dilated state, with greater ability to dilate in response to neural activation, resulting in a larger vessel cross-sectional area change. During wake, however, blood vessels may be in a semi-dilated state because they are continually providing metabolites to waking tissue with higher ongoing activity levels, and may undergo a smaller change in diameter due to saturation effects. Alternatively, larger ERPs during QS may result from increased synchronous neural activity recruiting more cells and exhibit a greater need for metabolites. As a result, there may be a larger recruitment of blood or increased deoxyhemoglobin concentration within the activated area during QS compared to wake and REM. These conclusions require additional experiments with multiple wavelengths to further investigate the nature of these blood volume changes.

Anesthetics alter the state of cortical cells through enhanced inhibition, potentially affecting neurovascular coupling. Isoflurane anesthesia showed a small initial evoked response along with a late synchronization of electrical burst activity that was larger on average than the waking response (Rojas et al., 2006), but elicited a significantly earlier evoked hemodynamic response. The hemodynamic response may result from a convolution of the ERP and burst responses which could not be dissected in the present study. The earlier phase shift in the hemodynamic signals seen under isoflurane anesthesia may result from a suppression of neurovascular control, or decreased latency in the overall neural response since the ERP also appeared earlier (see Figure 8.1). Further studies to relate the electrical activity and the hemodynamic response are needed to investigate the effects of different anesthetic agents on neurovascular coupling.

A similar hemodynamic response was reported by Chen-Bee *et al.* where a peak in the inverted optical response occurred around 1 s and a trough occurred around 4 s while the animal was anesthetized with Nembutal and atropine (Chen-Bee et al., 2007). These studies, however, were conducted using a whisker twitching stimulus paradigm and the optical measurements used 635 nm light. Regardless of these different recording protocols, the similarities between the hemodynamic responses reported here under isoflurane anesthesia are striking. However, our sleep and waking responses show a significantly different amplitude and timing that demonstrate behavioral state modulation of neurovascular coupling.

Since most optical studies are performed under a variety of different anesthetics and since alterations in the conscious state drastically affect the optical recordings, hemodynamic response models must address the behavioral state of the tissue under investigation. Different anesthetics may alter the neurovascular coupling as evident by the data presented here and elsewhere (Berwick et al., 2002; Chen et al., 2005; Chen-Bee et al., 2007). If the changes in blood perfusion were directly proportional to electrical activity, we would expect a linear increase in the hemodynamic response under QS. However, since the increase in the hemodynamic response under QS was not only larger amplitude, but also phase shifted later in time, a non-linear effect on neurovascular coupling is evident. Furthermore, the relationship between the two responses appears to differ depending on the state of the tissue. Studies with different stimulus intensities to investigate the coupling changes between the electrical and hemodynamic response are required. Investigation of the hemodynamic response during state transitions can further probe changes in state-dependent coupling.

Chapter 9

Sleep Deprivation Hemodynamic Effects

Neural activation initiates vascular dilation that delivers oxygen and glucose to the activated region; a phenomenon that forms the basis for a variety of functional imaging techniques including positron emission tomography (PET), functional magnetic resonance imaging (fMRI) and near infrared spectroscopy (NIRS) (Belliveau et al., 1991; Franceschini et al., 2008; Logothetis et al., 2001; Martin et al., 2006; Oakes et al., 2004; Roy and Sherrington, 1890; Villringer and Chance, 1997). With increased neural activity, more blood is required to supply metabolic demand. Of particular importance is whether there is a physiological limit to the amount of blood that can be delivered. Under pathological conditions, such as epilepsy or stroke, the blood vessels may reach a limit in their capacity to expand and deliver metabolites, leading to further tissue trauma. Waking activity does not normally require as many resources as severe pathological conditions; however, it is characterized by neural de-

---

Portions of this chapter were published as: SCHEI, J.L. AND RECTOR, D.M. 2011. Reduced evoked cerebral vascular responses following sleep deprivation. *Progress in Brain Research* (accepted).

polarization and frequent spontaneous action potentials, a period of activity with high metabolic demand. Thus, it is possible that vascular smooth muscle expansion during extended waking and sleep deprivation may also cause vessels to approach their limit of metabolite delivery, with the possibility of limited tissue resources during these periods. Alternatively, quiet sleep is characterized by a synchronous membrane potential oscillations between hyperpolarized and depolarized states at a Delta frequency (0.3 - 3 Hz), where neurons spend roughly half of the time in a hyperpolarized, less metabolically demanding state. Since regional cerebral blood flow and metabolism, as measured from resting brain activity, is decreased during quiet sleep compared to wakefulness (Braun et al., 1997), sleep may be required to restore the vascular compliance back to a more relaxed state.

Several lines of evidence support the notion that blood vessels exhibit compliance limits under non-pathological conditions. First, regional evoked vascular responses to external stimuli are larger during quiet sleep compared to wake (Larson-Prior et al., 2009; Schei et al., 2009), suggesting that blood vessels exhibit lower compliance during wake due to their larger volume, causing a blunted evoked response. Conversely, since basal cerebral blood flow and metabolism levels are lower during quiet sleep, vessel relaxation may allow a larger evoked vascular response, resulting in a larger influx of blood. Second, healthy, older adults exhibit decreased blood oxygen level-dependent (BOLD) responses, requiring age-sensitive fMRI studies (D'Esposito et al., 1999). Thus, age related changes may result from reduced smooth muscle compliance, impacting vascular responsiveness, and reducing local perfusion.

While limits to vascular dilation may not impact the tissue under normal conditions, over the long term, sleep restriction and deprivation have detrimental consequences on cerebral processing and cognitive performance (Goel et al., 2009; Van Dongen and Dinges, 2005). Conditions of impaired perfusion and over-driven cells underlie significant injury described for obstructive sleep apnea (OSA) (Macey et al., 2008). Additionally, studies following total sleep deprivation in humans showed decreased glucose metabolism in subcortical structures and increased in the visual cortex associated with a visual vigilance task, yet with no overall change in whole brain metabolism (Wu et al., 1991).

To test the hypothesis that prolonged high basal neural activity can decrease blood vessel compliance, and blunt evoked hemodynamic responses, we investigated both electrical and hemodynamic responses to auditory stimulation following varying amounts of sleep deprivation. Combined EEG and near infrared spectroscopy allow simultaneous assessment of electrical neural activity with vascular changes associated with increased metabolite demand during stimulation. With longer sleep deprivation periods, we expect the evoked vascular response will become smaller as blood vessels stretch and become less compliant.

9.1 Sleep Deprivation Paradigm

At least two weeks after surgical recovery, we recorded animals under freely moving conditions, using an acrylic chamber (26.5 cm x 26.5 cm x 34 cm) and tethered their headstage to a 55 cm cable connected to a swivel commutator (ProMed-Tec, Bellingham, MA, Pro-ES24). Food and water were available *ad libitum* and animals were housed under a 12-12 hour light cycle where ambient lights came on at 0:00. Ambient room temperature was approximately 22° C. Two hours after lights on (02:00), animals were brought from their housing area to the recording room, and tethered to the data acquisition system. Animals were sleep deprived for 2, 4, or 6 hours by gentle handling, gentle petting with a paintbrush, and introducing novel objects, then recordings proceeded for one hour after each deprivation session (Figure 9.1). To

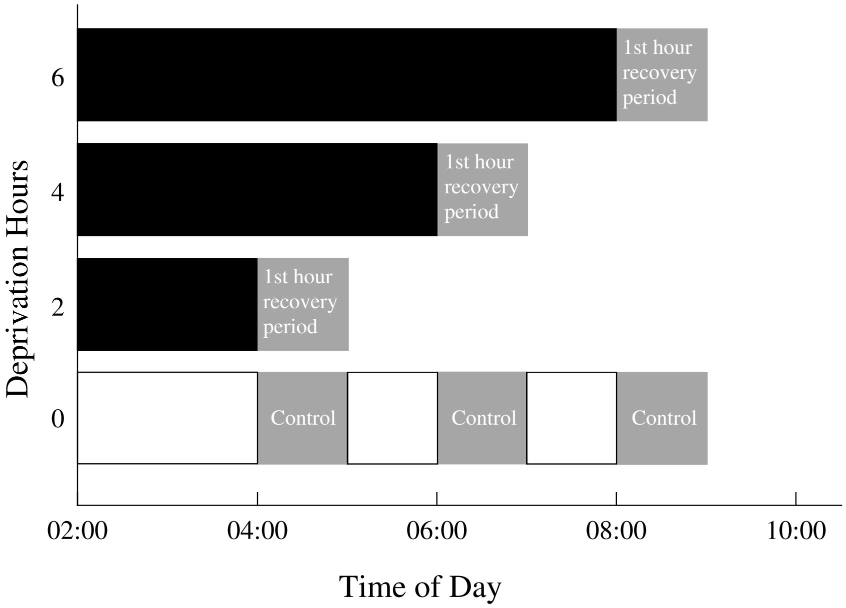

Figure 9.1: Sleep deprivation began two hours after lights on (02:00) and lasted for 2, 4, or 6 hours (black blocks). The first hour of the recovery period began at 04:00, 06:00, or 08:00, respectively, illustrated by the gray blocks. All results represent evoked responses collected during quiet sleep within this first hour recovery period. In the control condition, animals were freely behaving and responses were measured during a one hour period beginning at 04:00, 06:00, and 08:00.

control for time-of-day and novel environment effects, all animals were also recorded continuously during non-deprived conditions and were allowed to sleep normally for 7 hours, from 02:00 to 09:00. The order of sleep deprivation duration/control condition was randomized within and across animals, and each condition was repeated two to six times. Each animal was allowed one week recovery between recordings and sessions continued over a period of 8 months.

To generate evoked responses, we stimulated the auditory cortex using a train of 5 auditory clicks (10 Hz, ~65 dBa) delivered by a speaker placed 3 cm above the recording chamber. Stimuli occurred at random intervals between 2 and 13 seconds. Physiological data were amplified (AC photodiode x200, DC photodiode x1, EEG x1000, ECG x1000, EMG x1000), filtered (0.1 Hz - 3.2 kHz), and digitized (10 kHz) using custom built hardware (Rector and George, 2001). Additionally, we collected images using a digital USB camera (1 Hz) to aid in sleep scoring. All data were archived to a hard-drive for post hoc analysis.

9.2 Sleep Scoring

Electrophysiological data were sorted into 2 second epochs and fast Fourier transform (FFT) analysis was performed to calculate a power spectrum for different frequency ranges. A scatter plot of the EEG Delta power versus the total EMG power was generated using each 2 second epoch in the recording (Rector et al., 2009a). Data point density clusters revealed the animal state such that high EMG power and low EEG Delta power corresponded to wake; low EMG power and high EEG Delta power corresponded to quiet sleep; and low EMG power and low EEG Delta power corresponded to rapid eye movement (REM) sleep. Quiet sleep was further sorted into light quiet sleep (LQS) corresponding to higher EMG power and high EEG Delta power, and deep quiet sleep (DQS) corresponding to lower EMG power and high EEG Delta power (Rector et al., 2009a). Once clusters were sorted by state, we visually reviewed the physiological traces and camera images to confirm each epoch. Since the evoked vascular response lasted several seconds, state changes during the response may alter the signal, and such events were excluded from analysis. While arousals following the stimulus were rare (Phillips et al., 2011), if a state change occurred within 6 seconds of a stimulus, the stimulus was ignored, resulting in elimination of 5.7 ± 3.5 % of the total stimuli.

9.3 Sleep States

Increased sleep deprivation altered sleep patterns significantly during the first hour of the recovery period (Figure 9.2(A)). Compared to the 2 hour deprivation condition, there was significantly less time spent in wake and more time spent in LQS, DQS, and REM in the 4 hour and 6 hour deprivation conditions ($p < 0.05$). While the percent time spent in REM sleep increased with longer deprivation periods, it composed less than 15 percent of the total time. Consequently, there were too few stimuli present during REM, and the optical responses showed small signal-to-noise ratios. The data during waking states was convoluted with movement artifact, making the interpretation of the hemodynamic response difficult. Therefore, we focused our analysis on the LQS and DQS states. In the control condition, the total amount of time

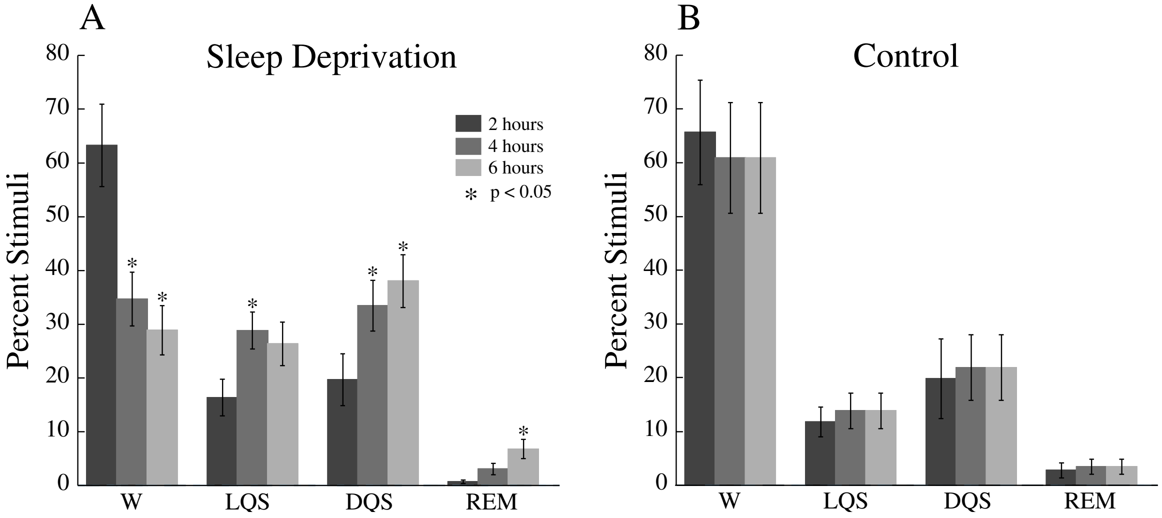

Figure 9.2: The percent time spent in each state for the first hour recovery period (A) from 4 animals shows that increased amounts of sleep deprivation caused a significant decrease in the percent time spent in wake (W) and a significant increase in the percent time spent in light quiet sleep (LQS), deep quiet sleep (DQS), and rapid eye movement sleep (REM). Significant changes are denoted with * ($p < 0.05$, Mann-Whitney U-test). During the no deprivation, control condition (B), no significant difference in the amount of time spent in wake or sleep across the three time periods was found, suggesting no time of day effect.

spent in wake and sleep did not significantly differ across the different time periods (Figure 9.2(B)). While we might expect to observe small time-of-day differences in sleep structure, the novel environment may have artificially increased the amount of waking these animals experienced over the recording period.

9.4 Evoked Electrical Responses

Two example traces are shown in Figure 9.3 from recordings conducted with no sleep deprivation. Evoked electrical responses showed larger P1 amplitudes during LQS and DQS compared to wake (Figure 9.3(A, B), $p < 0.05$), as expected (Rector et al., 2009a), at a 65 dBa stimulus intensity. The simultaneous evoked hemodynamic response peak amplitude was larger during LQS and DQS compared to wake (Schei et al., 2009) (Figure 9.3(C, D), $p < 0.05$).

A plot of the evoked electrical response potential (ERP) mean P1 and N1 amplitude from all 4 animals after both sleep deprivation and control conditions, along with standard error, is shown in Figure 9.4(A). There were no statistically significant within-state differences in the P1 and N1 amplitudes for LQS and DQS during the first hour recovery period following 2, 4, or 6 hours of sleep deprivation. Figure 9.4(B) shows the ERP P1 and N1 amplitudes for the no deprivation, control condition. The only difference we observed occurred between the third hour and seventh hour time periods where there was a small but significant decline in the ERP P1 amplitude ($p < 0.05$).

9.5 Evoked Hemodynamic Responses

Two examples of the evoked vascular responses during LQS (Figure 9.5(A, B)) and DQS (Figure 9.5(C, D)) for the first hour recovery period show that the evoked vas-

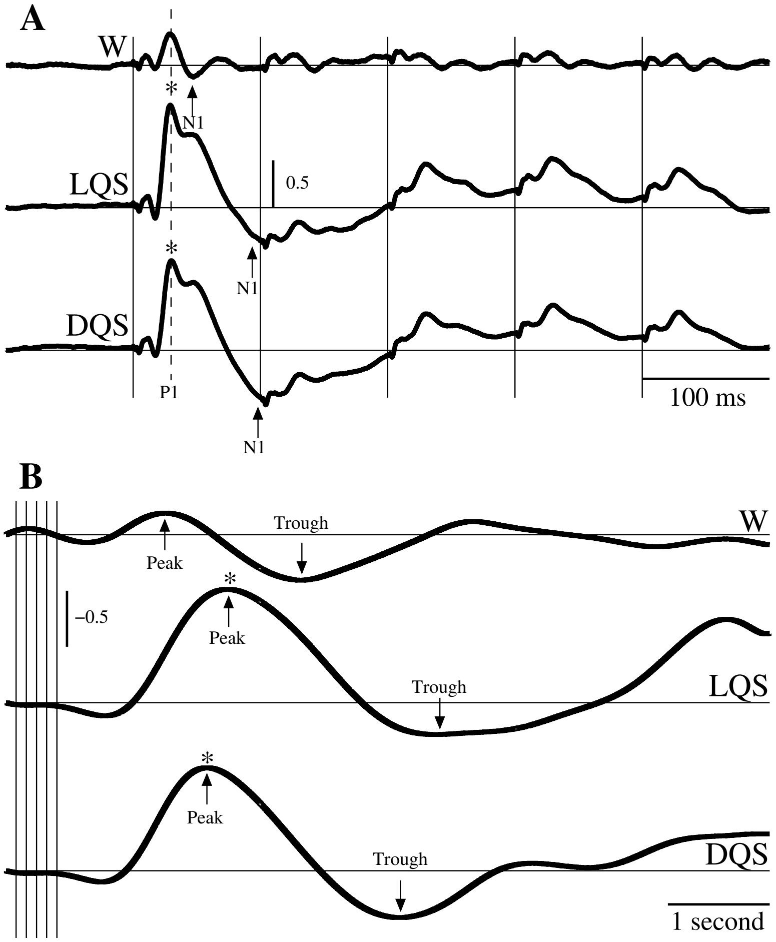

Figure 9.3: Example evoked electrical response potentials (ERPs, A, B) and inverted evoked hemodynamic responses (C, D) from two animals recorded under no sleep deprivation conditions. We measured the ERP P1 and N1 amplitudes and the hemodynamic response peak and trough amplitudes, as indicated by the arrows. In agreement with our previous report (Schei et al., 2009), the ERP P1 amplitude was larger during light quiet sleep (LQS) and deep quiet sleep (DQS) compared to wake (W) and the hemodynamic peak amplitude was larger during LQS and DQS compared to W. Significant changes are denoted with * ($p < 0.05$, Mann-Whitney U-test).

cular response became smaller for DQS with longer deprivation periods. We focused on the changes in the peak and trough amplitudes, indicated by the arrows, during LQS and DQS for the first hour recovery period following sleep deprivation.

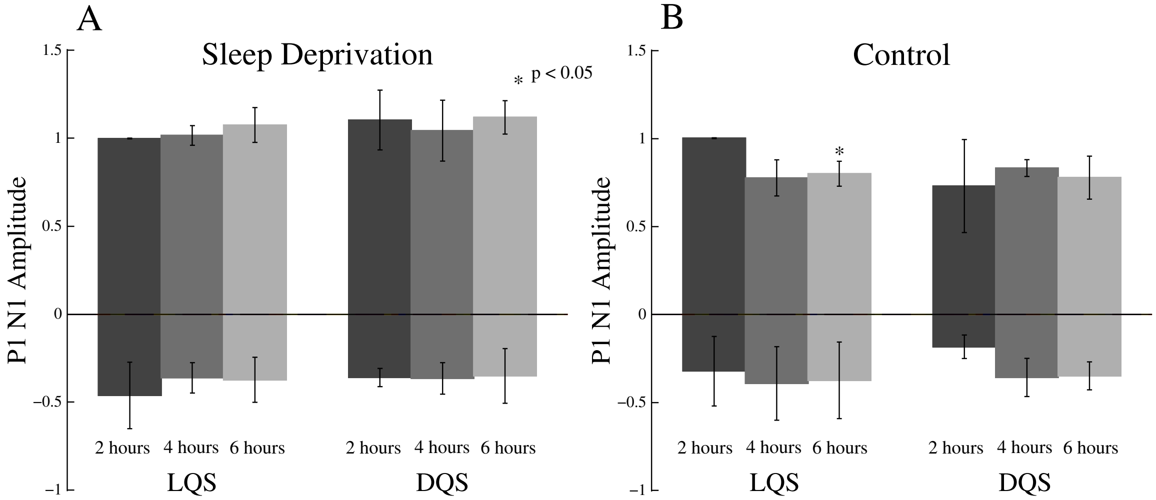

Figure 9.4: The evoked electrical response potential (ERP) P1 and N1 amplitudes across light quiet sleep (LQS) and deep quiet sleep (DQS) during the first hour recovery period measured from 4 animals showed no significant difference across deprivation hours (A). Under the no deprivation control (B), we observed a small but significant decline in the ERP P1 amplitude in the seventh hour compared to the third hour ($p < 0.05$, Mann-Whitney U-test).

Figure 9.6(A) shows the average and standard error of the peak and trough amplitudes from 4 animals after sleep deprivation. During the LQS state, the hemodynamic response peak and trough amplitudes did not significantly differ across sleep deprivation duration. However, the DQS peak amplitude was significantly smaller after 6 hours deprivation compared to those obtained after 2 hours deprivation ($p < 0.1$). The trough amplitude did not significantly differ across sleep deprivation periods. In the control condition, the peak and trough amplitudes did not significantly differ (Figure 9.6(B)).

9.6 Conclusions

In corroboration with our earlier studies, evoked hemodynamic responses were largest during quiet sleep (Figure 9.3) (Schei et al., 2009), and the control condition showed no

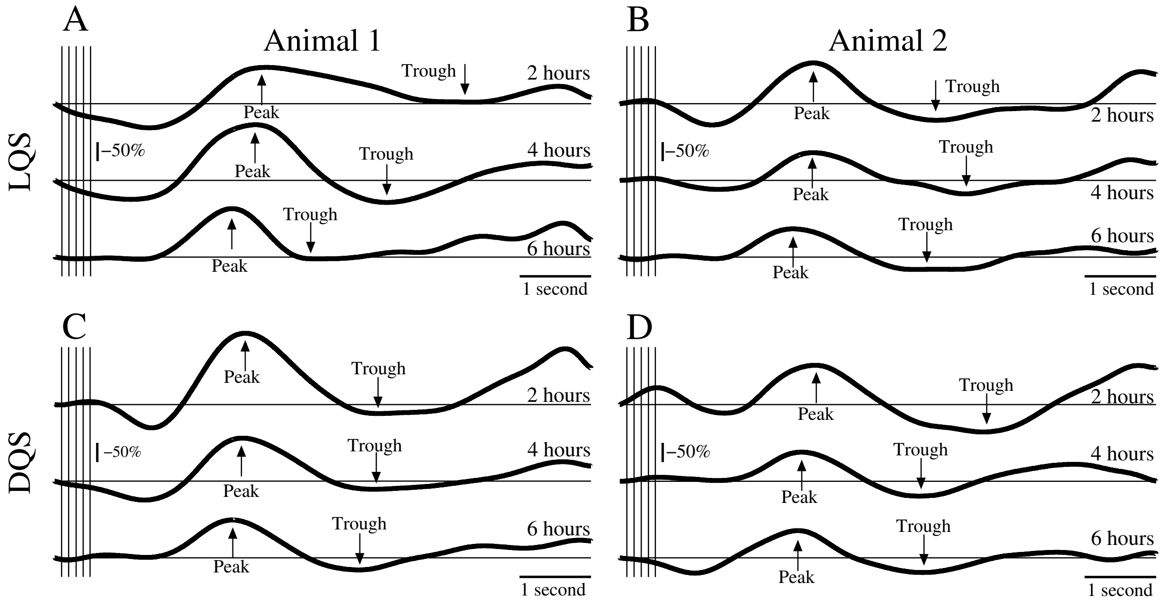

Figure 9.5: Two example inverted evoked optical response traces during the first hour recovery period across light quiet sleep (LQS, A, B) and deep quiet sleep (DQS, C, D) from 2 animals shows progressively smaller responses after sleep deprivation, particularly in DQS. When using 660 nm light, the optical response was dominated by changes in absorption due to blood volume and deoxyhemoglobin concentration changes. Therefore, the trace was inverted such that a peak in the signal corresponded to an evoked increase in blood volume/deoxyhemoglobin concentration. We measured the peak and trough components of the response, marked by arrows. The vertical scale bars represent the normalized percent change from the peak during LQS following 2 hours sleep deprivation. With longer sleep deprivation, the peak decreased, suggesting a blunted evoked response.

significant difference in hemodynamic response amplitude during LQS or DQS across 7 hours. However, with increased sleep deprivation, we observed a significant decrease in the evoked hemodynamic response amplitude during DQS. High neuronal use requires metabolites, stretching blood vessels and blunting the evoked hemodynamic response during wake. With prolonged use over extended waking periods, the surrounding vasculature may reach a limit in its ability to expand and supply metabolites to the activated tissue, further blunting evoked responses during sleep immediately following deprivation.

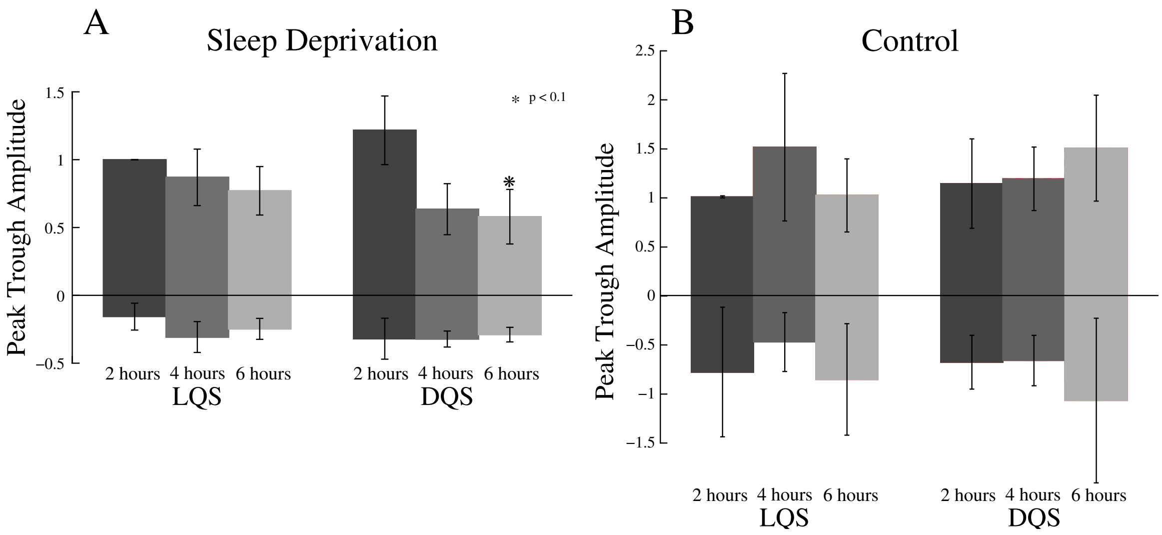

Figure 9.6: The peak and trough mean amplitude and standard error of the vascular response was measured from 4 animals during light quiet sleep (LQS) and deep quiet sleep (DQS) for the first hour recovery period following 2, 4, or 6 hours sleep deprivation (A). There was a trend for the response to be smaller during LQS with increased sleep deprivation; however, due to small signal-to-noise, the differences were not significant. During DQS, the peak amplitude significantly decreased in 6 hours deprivation compared to 2 hours deprivation. A mean decrease was also observed after 4 hours of sleep deprivation, but again, the variability was too high to reach significance. Significant changes are denoted with * ($p < 0.1$, Mann-Whitney U-test). Panel B shows the peak and trough mean amplitude and standard error of the vascular response from a no deprivation control condition during the same recovery time periods as the 2, 4, and 6 hour deprivation data. The peak and trough amplitudes did not significantly differ, suggesting no time-of-day effect on the vascular response.

The data from LQS showed a similar trend of decreasing vascular responses with longer sleep deprivation; however, this result did not reach significance due to high variability in the data. Future studies must reduce the variability in the hemodynamic signals to allow further assessment of extended neural use and sleep deprivation across all states, including wake and REM. Modifying the stimulation paradigm could produce more robust hemodynamic responses and enhance signal-to-noise ratios. For example, other work in our laboratory indicates that a 10 Hz stimulus initiates habituation, resulting in a smaller response, while a 5 Hz stimulus can produce a larger response. Additionally, the present study required significant effort by at least a dozen people to deprive and observe the animals over a period of 8 months; therefore, only 4 animals could be recorded. With further miniaturization of the headstage, currently in progress, such studies could be less labor-intensive and the number of animals could be increased. In spite of the high signal variability, these results are important, and could lead to additional studies into novel mechanisms of sleep control and incorporated into theories of sleep regulation which propose more localized control over sleep states within the cortex (Krueger et al., 2008; Rector et al., 2009b). For example, if limits to blood delivery could lead to metabolic deficiency, then local sleep may be required to restore vascular compliance and resources to the tissue.

Mounting evidence suggests that basal neural activity has a significant effect on the evoked hemodynamic response. Cerebral blood flow and the BOLD response are correlated to Delta rhythms and k-complexes (Czisch et al., 2004) as well as isoflurane bursting EEG activity (Liu et al., 2010). The waking state is characterized by high basal neural activity and is highly demanding of metabolites to replenish the tissue, and in response, blood vessels expand to allow for sufficient nutrient delivery, which may reduce vessel compliance, blunting the evoked hemodynamic response. Thus, during wake, the evoked vascular response was smaller in amplitude compared to quiet sleep due to these potential limits. Consequently, smaller vascular responses in DQS were observed following sleep deprivation, which may be due to decreased vessel compliance. Synchronous Delta rhythms of membrane potential fluctuations between depolarized and hyperpolarized states during quiet sleep may be less metabolically demanding, allowing blood vessels to relax and become more compliant during sleep.

The present study provides preliminary evidence for a novel mechanism in the control of sleep. If high basal neural activity during wake can cause vessels to approach their limits in blood delivery due to stretching and low compliance, sleep may serve as a mechanism to circumvent tissue damage associated with metabolic deficit. Furthermore, sleep deprivation puts additional strains on the system and longer sleep bouts may be needed for the restoration period (Friedman et al., 1979). Chronic sleep restriction, deprivation, and other sleep pathologies, may be consequential to the limits of the cerebral vasculature over the long term and lead to processing deficits, performance impairments, and tissue damage.

Chapter 10

Conclusions

These data support the hypothesis that one of the primary functions of sleep may be to restore the ability of the vasculature to deliver essential metabolites to tissue. Long periods of neural activity require continual provision of metabolites to the tissue. During waking activity, cortical columns modulate their vascular supply through vasodilation to increase blood volume and flow in an activity and use-dependent manner. Extended neural use may lead to a metabolic deficit when the vessels can no longer dilate to provide nutrients to the activated region. When metabolic demand exceeds supply, cells within the localized region could enter a hyperpolarized, sleep-like state, lowering metabolic requirements, reducing vasodilation, and restoring metabolites to the region. Sleep states may serve as a neural protection mechanism that limits activity during times of low metabolic supply, similar to the way that muscles fatigue before metabolic resources become limited (Enoka and Duchateau, 2008). Sleep related vascular changes may be used to assess tissue state and ultimately assist in predicting task performance errors.

Portions of this chapter were published as: Schei, J.L. and Rector, D.M. Assessment of network states: Local hemodynamics. *Topics in Medicinal Chemistry* (in press).

These experiments demonstrated larger hemodynamic response amplitudes during quiet sleep, which could be related to changes in vessel compliance. In order to further examine the vascular consequences of wake and sleep with finer temporal resolution, our future experiments include separating evoked responses between different periods of sustained states. Currently, we require many averaged responses to assess the time course of the hemodynamic response because these experiments were limited by signal-to-noise ratios in the optical response, especially during wakefulness where movement artifact contaminated the signal. Additionally, rats exhibit polyphasic sleep patterns (multiple bouts of sleep interrupted by wake periods), potentially decreasing the period and increasing the frequency of vascular recovery compared to animals that exhibit monophasic sleep (a single bout of sleep in a 24 hour period) or biphasic sleep (two bouts of sleep in a 24 hour period) patterns. To improve the signal-to-noise ratios, different stimulation paradigms that generate stronger hemodynamic responses may allow for fewer averages and further separation of evoked responses during periods of wake and sleep. We can further dissect the hemodynamic response into oxyhemoglobin and deoxyhemoglobin concentrations changes by using multiple wavelength illumination since light absorption is wavelength-dependent and the individual components can be assessed using the modified Beer-Lambert law (Boas et al., 2001). Additionally, changes in cerebral blood flow can be measured using Doppler flow or laser speckle analysis. Each of these approaches will assist in further demonstrating vascular compliance changes across wake and sleep states.

Publications Resulting from this Work

Refereed Papers

Schei, J.L., McCluskey, M.D., Foust, A.J., Yao, X.-C., and Rector, D.M. 2008. Action potential propagation imaged with high temporal resolution near-infrared video microscopy and polarized light. *NeuroImage* 40:1034-1043.

Foust, A.J., **Schei, J.L.**, Rojas, M.J., and Rector, D.M. 2008. In vitro and in vivo noise analysis for optical neural recording. *Journal of Biomedical Optics* 13:0044038.

Schei, J.L., Foust, A.J., Rojas, M.J., Navas, J.A., and Rector, D.M. 2009. State-dependent auditory evoked hemodynamic responses recorded optically with indwelling photodiodes. *Applied Optics* 48:D121-D129.

Rector, D.M., **Schei, J.L.**, Van Dongen, H.P.A., Belenky, G., and Krueger, J.M. 2009. Physiological markers of local sleep. *European Journal of Neuroscience* 29:1771-1778.

Schei, J.L. and Rector, D.M. 2011. Assessment of network states: Local hemodynamics. *Topics in Medicinal Chemistry* (in press).

Schei, J.L. and Rector, D.M. 2011. Reduced evoked cerebral vascular responses following sleep deprivation. *Progress in Brain Research* (accepted).

Abstracts and Published Proceedings*

Rector, D.M., Foust, A.J., **Schei, J.L.**, and McCluskey, M.D. 2006. Neural activity imaged with reflected near-infrared birefringence video microscopy. *In* Neuroscience 2006. Society for Neuroscience.

Schei, J.L., Foust, A.J., Rojas, M.J., Navas, J.A., Wilson, A.R., and Rector, D.M 2007. Evoked metabolic responses differ significantly during sleep stages. *In* Neuroscience 2007. Society for Neuroscience.

Foust, A.J., **Schei, J.L.**, Rojas, M.J., and Rector, D.M. 2007. Low noise light emitting diodes outperform high intensity coherent sources for neural recording both in-vivo and in-vitro. *In* Neuroscience 2007. Society for Neuroscience.

Schei, J.L., Foust, A.J., Rojas, M.J., Navas, J.A., and Rector, D.M. 2008. Evoked optical response under wake, sleep and anesthetized states. *In* Biomedical Optics. Optical Society of America.

Schei, J.L., Foust, A.J., Rojas, M.J., Navas, J.A., and Rector, D.M. 2008. Evoked optical responses differ between quiet sleep stages. *In* Journal of Sleep and Sleep Disorders Research. Associated Professional Sleep Societies.

Schei, J.L., Phillips, D.P., Rojas, M.J., and Rector, D.M. 2009. Evoked hemodynamic responses decrease following sleep deprivation. *In* Journal of Sleep and Sleep Disorders Research. Associated Professional Sleep Societies.

Schei, J.L., McCluskey, M.D., and Rector, D.M. 2009. Fast optical neurophysiology. Research and Industrial Collaboration Conference: Focus on Sensing and Imaging Technologies.

Schei, J.L., M.D. McCluskey, and Rector, D.M. 2009. Biophysical mechanisms underlying fast optical neurophysiology. WE-Heraeus Seminar: Optical Imaging of Brain Function.

Rector, D.M., **Schei, J.L.**, and Meighan, P.C. 2009. Implantable data systems with photodetectors and multiple light sources for optical studies in freely moving and restrained rodents. WE-Heraeus Seminar: Optical Imaging of Brain Function.

Schei, J.L., Phillips, D.J., Rojas, M.J., and Rector, D.M. 2010. Evoked hemodynamic responses decrease following sleep deprivation. NSF IGERT 2010 Project Meeting.

Rector, D.M. And **Schei, J.L.** 2010. Microvascular compliance changes across sleep and wake: Mechanisms for local sleep regulation. 26th International Summer School of Brain Research.

***Schei, J.L.** Van Nortwick, A. S., Meighan, P. C., and Rector, D.M. 2011. Saturation thresholds of evoked neural and hemodynamic responses in awake and asleep rats. *Proceedings of SPIE* 7898:78981D.

Book Chapters

Schei, J.L. and Rector, D.M. 2009. Fast Optical Neurophysiology, chapter 10, pp. 223-243. *In* A.W. Roe (ed.), Imaging the Brain with Optical Methods. Springer, New York, NY.

Bibliography

Aaslid, R., Lindegaard, K., Sorteberg, W., and Nornes, H. 1989. Cerebral autoregulation dynamics in humans. *Stroke* 20:45.

Achermann, P. and Borbely, A. 2003. Mathematical models of sleep regulation. *Frontiers in Bioscience* 8:S683–S693.

Arridge, S. and Hebden, J. 1997. Optical imaging in medicine: II. Modelling and reconstruction. *Physics in Medicine and Biology* 42:841–853.

Belenky, G., Wesensten, N., Thorne, D., Thomas, M., Sing, H., Redmond, D., Russo, M., and Balkin, T. 2003. Patterns of performance degradation and restoration during sleep restriction and subsequent recovery: a sleep dose-response study. *Journal of Sleep Research* 12:1–12.

Belliveau, J., Kennedy Jr, D., McKinstry, R., Buchbinder, B., Weisskoff, R., Cohen, M., Vevea, J., Brady, T., and Rosen, B. 1991. Functional mapping of the human visual cortex by magnetic resonance imaging. *Science* 254:716–719.

Berezhnyy, I. and Dogariu, A. 2004. Time-resolved mueller matrix imaging polarimetry. *Optics Express* 12:4635–4649.

BERGER, H. 1929. Über das elektrenkephalogramm des menschen. *European Archives of Psychiatry and Clinical Neuroscience* 87:527–570.

BERWICK, J., MARTIN, C., MARTINDALE, J., JONES, M., JOHNSTON, D., ZHENG, Y., REDGRAVE, P., AND MAYHEW, J. 2002. Hemodynamic response in the unanesthetized rat: Intrinsic optical imaging and spectroscopy of the barrel cortex. *Journal of Cerebral Blood Flow & Metabolism* 22:670–679.

BIXLER, E. 2009. Sleep and society: An epidemiological perspective. *Sleep Medicine* 10:S3–S6.

BOAS, D., BROOKS, D., MILLER, E., DIMARZIO, C., KILMER, M., GAUDETTE, R., AND ZHANG, Q. 2002. Imaging the body with diffuse optical tomography. *IEEE Signal Processing Magazine* 18:57–75.

BOAS, D., GAUDETTE, T., STRANGMAN, G., CHENG, X., MAROTA, J., AND MANDEVILLE, J. 2001. The accuracy of near infrared spectroscopy and imaging during focal changes in cerebral hemodynamics. *NeuroImage* 13:76–90.

BORBÉLY, A., BAUMANN, F., BRANDEIS, D., STRAUCH, I., AND LEHMANN, D. 1981. Sleep deprivation: Effect on sleep stages and EEG power density in man. *Electroencephalography and Clinical Neurophysiology* 51:483–493.

BRAUN, A., BALKIN, T., WESENTEN, N., CARSON, R., VARGA, M., BALDWIN, P., SELBIE, S., BELENKY, G., AND HERSCOVITCH, P. 1997. Regional cerebral blood flow throughout the sleep-wake cycle. An H2 (15) O PET study. *Brain* 120:1173–1197.

BUCHSBAUM, M., GILLIN, J., WU, J., HAZLETT, E., SICOTTE, N., AND DUPONT, R. 1989. Regional cerebral glucose metabolic rate in human sleep assessed by positron emission tomography. *Life Sciences* 45:1349–1356.

BUCKWEITZ, E., SINHA, A., AND WEISS, H. 1980. Cerebral regional oxygen consumption and supply in anesthetized cat. *Science (New York, NY)* 209:499–501.

CARTER, K. M., GEORGE, J. S., AND RECTOR, D. M. 2004. Simultaneous birefringence and scattered light measurements reveal anatomical features in isolated crustacean nerve. *Journal of Neuroscience Methods* 135:9–16.

CHEN, L., FRIEDMAN, R., AND ROE, A. 2005. Optical imaging of SI topography in anesthetized and awake squirrel monkeys. *Journal of Neuroscience* 25:7648–7659.

CHEN-BEE, C. H., AGONCILLO, T., XIONG, Y., AND FROSTIG, R. D. 2007. The triphasic intrinsic signal: Implications for functional imaging. *Journal of Neuroscience* 27:4572–4586.

CHEONG, W., PRAHL, S., AND WELCH, A. 1990. A review of the optical properties of biological tissues. *IEEE Journal of Quantum Electronics* 26:2166–2185.

COHEN, L. B., KEYNES, R. D., AND HILLE, B. 1968. Light scattering and birefringence changes during nerve activity. *Nature* 218:438–441.

COLRAIN, I. AND CAMPBELL, K. 2007. The use of evoked potentials in sleep research. *Sleep Medicine Reviews* 11:277–293.

CRAGG, B. G. 1951. The turgidity of giant axons. *Journal of Physiology* 114:234–239.

CULVER, J. P., SIEGEL, A. M., FRANCESCHINI, M. A., MANDEVILLE, J. B., AND BOAS, D. A. 2005. Evidence that cerebral blood volume can provide brain activation maps with better spatial resolution than deoxygenated hemoglobin. *NeuroImage* 27:947–959.

CZISCH, M., WEHRLE, R., KAUFMANN, C., WETTER, T., HOLSBOER, F., POLLMÄCHER, T., AND AUER, D. 2004. Functional MRI during sleep: BOLD signal decreases and their electrophysiological correlates. *European Journal of Neuroscience* 20:566–574.

D'Esposito, M., Zarahn, E., Aguirre, G., and Rypma, B. 1999. The effect of normal aging on the coupling of neural activity to the bold hemodynamic response. *NeuroImage* 10:6–14.

Devor, A., Dunn, A., Andermann, M., Ulbert, I., Boas, D., and Dale, A. 2003. Coupling of total hemoglobin concentration, oxygenation, and neural activity in rat somatosensory cortex. *Neuron* 39:353–359.

Devor, A., Tian, P., Nishimura, N., Teng, I. C., Hillman, E. M. C., Narayanan, S. N., Ulbert, I., Boas, D. A., Kleinfeld, D., and Dale, A. M. 2007. Suppressed neuronal activity and concurrent arteriolar vasoconstriction may explain negative blood oxygenation level-dependent signal. *Journal of Neuroscience* 27:4452–4459.

Dunn, A., Devor, A., Dale, A., and Boas, D. 2005. Spatial extent of oxygen metabolism and hemodynamic changes during functional activation of the rat somatosensory cortex. *NeuroImage* 27:279–290.

Eggert, H. R. and Blazek, V. 1987. Optical properties of human brain tissue, meninges, and brain tumors in the spectral range of 200 to 900 nm. *Neurosurgery* 21:459–464.

Enoka, R. and Duchateau, J. 2008. Muscle fatigue: What, why and how it influences muscle function. *The Journal of Physiology* 586:11–23.

Flaig, J. V. 1947. Viscosity changes in axoplasm under stimulation. *Journal of Neurophysiology* 10:211–221.

Foust, A. and Rector, D. 2007. Optically teasing apart neural swelling and depolarization. *Neuroscience* 145:887–899.

Foust, A. J., Beiu, R. M., and Rector, D. M. 2005. Optimized birefringence changes during isolated nerve activation. *Applied Optics* 44:2008–2012.

Foust, A. J., Schei, J. L., Rojas, M. J., and Rector, D. M. 2008. In vitro and in vivo noise analysis for optical neural recording. *Journal of Biomedical Optics* 13:044038.

Fox, P., Raichle, M., Mintun, M., and Dence, C. 1988. Nonoxidative glucose consumption during focal physiologic neural activity. *Science* 241:462–464.

Franceschini, M., Nissilä, I., Wu, W., Diamond, S., Bonmassar, G., and Boas, D. 2008. Coupling between somatosensory evoked potentials and hemodynamic response in the rat. *NeuroImage* 41:189–203.

Friedman, L., Bergmann, B., and Rechtschaffen, A. 1979. Effects of sleep deprivation on sleepiness, sleep intensity, and subsequent sleep in the rat. *Sleep* 1:369–391.

Frostig, R. D., Lieke, E. E., Ts'o, D. Y., and Grinvald, A. 1990. Cortical functional architecture and local coupling between neuronal activity and the microcirculation revealed by in vivo high-resolution optical imaging of intrinsic signals. *Proceedings of the National Academy of Sciences of the United States of America* 87:6082–6086.

Fukui, Y., Ajichi, Y., and Okada, E. 2003. Monte Carlo prediction of near-infrared light propagation in realistic adult and neonatal head models. *Applied Optics* 42:2881–2887.

Furusawa, K. 1929. The depolarization of crustacean nerve by stimulation or oxygen want. *Journal of Physiology* 67:325–342.

Gerrard, A. and Burch, J. M. 1975. Introduction to matrix methods in optics. Wiley.

Ghosh, N., Wood, M. F. G., and Vitkin, I. A. 2008. Mueller matrix decomposition for extraction of individual polarization parameters from complex turbid media exhibiting multiple scattering, optical activity, and linear birefringence. *Journal of Biomedical Optics* 13:044036.

Goel, N., Rao, H., Durmer, J., and Dinges, D. 2009. Neurocognitive consequences of sleep deprivation. *Seminars in Neurology* 29:320–339.

Goldman, D. 1943. Potential, impedance, and rectification in membranes. *The Journal of General Physiology* 27:37–60.

Gratton, G., Fabiani, M., Corballis, P. M., and Gratton, E. 1997. Non-invasive detection of fast signals from the cortex using frequency-domain optical methods. *New York Academy Sciences Annals* 820:286–299.

Grinvald, A., Lieke, E., Frostig, R. D., Gilbert, C. D., and Wiesel, T. N. 1986. Functional architecture of cortex revealed by optical imaging of intrinsic signals. *Nature* 324:361–364.

Hadley, K. and Vitkin, I. 2002. Optical rotation and linear and circular depolarization rates in diffusively scattered light from chiral, racemic, and achiral turbid media. *Journal of Biomedical Optics* 7:291–299.

Hall, J. 2006. New handbook of auditory evoked responses. Pearson.

Hecht, E. 2002. Optics. Addison Wesley, fourth edition.

Hill, D. K. and Keynes, R. D. 1949. Opacity changes in stimulated nerve. *Journal of Physiology* 108:278–281.

Hillman, E. 2007. Optical brain imaging in vivo: Techniques and applications from animal to man. *Journal of Biomedical Optics* 12:051402.

Hillman, E., Devor, A., Bouchard, M., Dunn, A., Krauss, G., Skoch, J., Bacskai, B., Dale, A., and Boas, D. 2007. Depth-resolved optical imaging and microscopy of vascular compartment dynamics during somatosensory stimulation. *NeuroImage* 35:89–104.

Hodgkin, A. L. and Huxley, A. F. 1952. Propagation of electrical signals along giant nerve fibres. *Proceedings of the Royal Society of London. Series B, Biological Sciences* 140:177–183.

Hodgkin, A. L. and Keynes, R. D. 1955. Active transport of cations in giant axons from Sepia and Loligo. *Journal of Physiology* 128:28–60.

Hoge, R., Atkinson, J., Gill, B., Crelier, G., Marrett, S., and Pike, G. 1999. Linear coupling between cerebral blood flow and oxygen consumption in activated human cortex. *Proceedings of the National Academy of Sciences of the United States of America* 96:9403.

Hoshi, Y. and Tamura, M. 1993. Dynamic multichannel near-infrared optical imaging of human brain activity. *Journal of Applied Physiology* 75:1842–1846.

Iadecola, C. and Nedergaard, M. 2007. Glial regulation of the cerebral microvasculature. *Nature Neuroscience* 10:1369–1376.

Jakovcevic, D. and Harder, D. 2007. Role of astrocytes in matching blood flow to neuronal activity. *Current Topics in Developmental Biology* 79:75–97.

Jöbsis, F. 1977. Noninvasive, infrared monitoring of cerebral and myocardial oxygen sufficiency and circulatory parameters. *Science* 198:1264.

Jones, M., Devonshire, I., Berwick, J., Martin, C., Redgrave, P., and Mayhew, J. 2008. Altered neurovascular coupling during information-processing states. *European Journal of Neuroscience* 27:2758–2772.

Kandel, E., Schwartz, J., and Jessell, T. 2000. Principles of neural science. McGraw-Hill, 4th edition.

Knight, R., Brailowsky, S., Scabini, D., and Simpson, G. 1985. Surface auditory evoked potentials in the unrestrained rat: Component definition. *Electroencephalography and Clinical Neurophysiology* 61:430–439.

Kornakova, Y. E., Frank, G. M., and Shtyngauz, L. N. 1947. Structural processes in the nerve. *Fiziol. J. USSR* 33:483–494.

Krueger, J. and Obäl Jr, F. 1993. A neuronal group theory of sleep function. *Journal of Sleep Research* 2:63–69.

Krueger, J., Rector, D., Roy, S., Van Dongen, H., Belenky, G., and Panksepp, J. 2008. Sleep as a fundamental property of neuronal assemblies. *Nature Reviews Neuroscience* 9:910–919.

Landowne, D. 1985. Molecular motion underlying activation and inactivation of sodium channels in squid giant axons. *Journal of Membrane Biology* 88:173–185.

Larson-Prior, L., Zempel, J., Nolan, T., Prior, F., Snyder, A., and Raichle, M. 2009. Cortical network functional connectivity in the descent to sleep. *Proceedings of the National Academy of Sciences* 106:4489–4494.

Leenders, K., Perani, D., Lammertsma, A., Heather, J., Buckingham, P., Jones, T., Healy, M., Gibbs, J., Wise, R., Hatazawa, J., et al. 1990. Cerebral blood flow, blood volume and oxygen utilization: normal values and effect of age. *Brain* 113:27–47.

Liu, X., Zhu, X., Zhang, Y., and Chen, W. 2010. Neural origin of spontaneous hemodynamic fluctuations in rats under burst-suppression anesthesia condition. *Cerebral Cortex* .

Logothetis, N., Pauls, J., Augath, M., Trinath, T., and Oeltermann, A. 2001. Neurophysiological investigation of the basis of the fMRI signal. *Nature* 412:150–157.

Lu, S.-Y. and Chipman, R. A. 1996. Interpretation of mueller matrices based on polar decomposition. *Journal of the Optical Society of America A* 13:1106–1113.

Macey, P., Kumar, R., Woo, M., Valladares, E., Yan-Go, F., and Harper, R. 2008. Brain structural changes in obstructive sleep apnea. *Sleep* 31:967–977.

Maclin, E. L., Low, K. A., Sable, J. J., Fabiani, M., and Gratton, G. 2004. The event-related optical signal to electrical stimulation of the median nerve. *NeuroImage* 21:1798–1804.

Madsen, P. and Vorstrup, S. 1991. Cerebral blood flow and metabolism during sleep. *Cerebrovascular and Brain Metabolism Reviews* 3:281–296.

Mahowald, M. and Schenck, C. 2005. Insights from studying human sleep disorders. *Nature* 437:1279–1285.

Mann, G. 1894. Histological changes induced in sympathetic, motor, and sensory nerve cells by functional activity. *Journal of Anatomy and Physiology* 29:100–108.

Maquet, P. 2000. Functional neuroimaging of normal human sleep by positron emission tomography. *Journal of Sleep Research* 9:207–231.

Martin, C., Martindale, J., Berwick, J., and Mayhew, J. 2006. Investigating neural-hemodynamic coupling and the hemodynamic response function in the awake rat. *NeuroImage* 32:33–48.

Masamoto, K. and Tanishita, K. 2009. Oxygen transport in brain tissue. *Journal of Biomechanical Engineering* 131:074002.

Massimini, M., Rosanova, M., and Mariotti, M. 2003. EEG slow ($\sim$1 Hz) waves are associated with nonstationarity of thalamo-cortical sensory processing in the sleeping human. *Journal of Neurophysiology* 89:1205–1213.

Maxwell, J. C. 1865. A dynamical theory of the electromagnetic field. *Philosophical Transactions of the Royal Society of London* 155:459–512.

Mayhew, J., Johnston, D., Berwick, J., Jones, M., Coffey, P., and Zheng, Y. 2000. Spectroscopic analysis of neural activity in brain: Increased oxygen consumption following activation of barrel cortex. *NeuroImage* 12:664–675.

McNichols, R. and Cote, G. 2000. Optical glucose sensing in biological fluids: an overview. *Journal of Biomedical Optics* 5:5–16.

Niedermeyer, E. and Da Silva, F. 2005. Electroencephalography: Basic principles, clinical applications, and related fields. Lippincott Williams & Wilkins.

Oakes, T., Pizzagalli, D., Hendrick, A., Horras, K., Larson, C., Abercrombie, H., Schaefer, S., Koger, J., and Davidson, R. 2004. Functional coupling of simultaneous electrical and metabolic activity in the human brain. *Human Brain Mapping* 21:257–270.

Oldenbourg, R., Salmon, E., and Tran, P. 1998. Birefringence of single and bundled microtubules. *Biophysical Journal* 74:645–654.

Orzeł-Gryglewska, J. 2010. Consequences of sleep deprivation. *International Journal of Occupational Medicine and Environmental Health* 23:95–114.

Penfield, W. and Jasper, H. 1954. Epilepsy and the functional anatomy of the human brain. Little, Brown.

Phillips, D., Schei, J., Meighan, P., and Rector, D. 2011. Cortical evoked responses associated with arousal from sleep. *Sleep* 34:65–72.

Pittman, R. 1986. In vivo photometric analysis of hemoglobin. *Annals of Biomedical Engineering* 14:119–137.

Prahl, S. 1999. Tabulated molar extinction coefficient for hemoglobin in water.

Rector, D. and George, J. 2001. Continuous image and electrophysiological recording with real-time processing and control. *Methods* 25:151–163.

Rector, D., Schei, J., and Rojas, M. 2009a. Mechanisms underlying state dependent surface-evoked response patterns. *Neuroscience* 159:115–126.

Rector, D. M., Carter, K. M., Volegov, P. L., and George, J. S. 2005a. Spatio-temporal mapping of rat whisker barrels with fast scattered light signals. *NeuroImage* 26:619–627.

Rector, D. M., Poe, G. R., Kristensen, M. P., and Harper, R. M. 1997. Light scattering changes follow evoked potentials from hippocampal schaeffer collateral stimulation. *Journal of Neurophysiology* 78:1707–1713.

Rector, D. M., Ranken, D. M., and George, J. S. 2003. High-performance confocal system for microscopic or endoscopic applications. *Methods* 30:16–27.

Rector, D. M., Schei, J. L., Dongen, H. P. A. V., Belenky, G., and Krueger, J. M. 2009b. Physiological markers of local sleep. *European Journal of Neuroscience* 29:1771–1778.

Rector, D. M., Topchiy, I. A., Carter, K. M., and Rojas, M. J. 2005b. Local functional state differences between rat cortical columns. *Brain Research* 1047:45–55.

Roggan, A., Friebel, M., Dörschel, K., Hahn, A., and Müller, G. 1999. Optical properties of circulating human blood in the wavelength range 400–2500 nm. *Journal of Biomedical Optics* 4:36–46.

Rojas, M. J., Navas, J. A., and Rector, D. M. 2006. Evoked response potential markers for anesthetic and behavioral states. *American Journal of Physiology - Regulatory, Integrative and Comparative Physiology* 291:R189–196.

Rolfe, D. and Brown, G. 1997. Cellular energy utilization and molecular origin of standard metabolic rate in mammals. *Physiological Reviews* 77:731–758.

Rosanova, M. and Timofeev, I. 2005. Neuronal mechanisms mediating the variability of somatosensory evoked potentials during sleep oscillations in cats. *The Journal of Physiology* 562:569–582.

Roy, C. and Sherrington, C. 1890. On the regulation of the blood-supply of the brain. *The Journal of Physiology* 11:85–158.

Salzberg, B., Kosterin, P., Muschol, M., Obaid, A., Rumyantsev, S., Bilenko, Y., and Shur, M. 2005. An ultra-stable non-coherent light source for optical measurements in neuroscience and cell physiology. *Journal of Neuroscience Methods* 141:165–169.

Schei, J. L., Foust, A. J., Rojas, M. J., Navas, J. A., and Rector, D. M. 2009. State-dependent auditory evoked hemodynamic responses recorded optically with indwelling photodiodes. *Applied Optics* 48:D121–D129.

Schei, J. L., McCluskey, M. D., Foust, A. J., Yao, X.-C., and Rector, D. M. 2008. Action potential propagation imaged with high temporal resolution near-infrared video microscopy and polarized light. *NeuroImage* 40:1034–1043.

Sheth, S., Nemoto, M., Guiou, M., Walker, M., Pouratian, N., and Toga, A. W. 2003. Evaluation of coupling between optical intrinsic signals and neuronal activity in rat somatosensory cortex. *NeuroImage* 19:884–894.

Sochurek, H. and Miller, P. 1987. Medicine's new vision. *National Geographic Magazine* pp. 2–41.

Steinbrink, J., Kohl, M., Obrig, H., Curio, G., Syr, F., Thomas, F., Wabnitz, H., Rinneberg, H., and Villringer, A. 2000. Somatosensory evoked fast optical intensity changes detected non-invasively in the adult human head. *Neuroscience Letters* 291:105–108.

Stepnoski, R., LaPorta, A., Raccuia-Behling, F., Blonder, G., Slusher, R., and Kleinfeld, D. 1991. Noninvasive detection of changes in membrane potential in cultured neurons by light scattering. *Proceedings of the National Academy of Sciences of the United States of America* 88:9382–9386.

Steriade, M., Timofeev, I., and Grenier, F. 2001. Natural waking and sleep states: a view from inside neocortical neurons. *Journal of Neurophysiology* 85:1969–1985.

Strandgaard, S. and Paulson, O. 1984. Cerebral autoregulation. *Stroke* 15:413.

Taddeucci, A., Martelli, F., Barilli, M., Ferrari, M., and Zaccanti, G. 1996. Optical properties of brain tissue. *Journal of Biomedical Optics* 1:117–123.

Tasaki, I., Watanabe, A., Sandlin, R., and Carnay, L. 1968. Changes in fluorescence, turbidity, and birefringence associated with nerve excitation. *Proceedings of the National Academy of Sciences of the United States of America* 61:883–888.

Tassi, P., Bonnefond, A., Engasser, O., Hoeft, A., Eschenlauer, R., and Muzet, A. 2006. EEG spectral power and cognitive performance during sleep inertia: the effect of normal sleep duration and partial sleep deprivation. *Physiology & Behavior* 87:177–184.

Uludag, K., Dubowitz, D., Yoder, E., Restom, K., Liu, T., and Buxton, R. 2004. Coupling of cerebral blood flow and oxygen consumption during physiological activation and deactivation measured with fMRI. *NeuroImage* 23:148–155.

Van Dongen, H. and Dinges, D. 2005. Sleep, circadian rhythms, and psychomotor vigilance. *Clinical Sports Medicine* 24:237–249.

Villringer, A. and Chance, B. 1997. Non-invasive optical spectroscopy and imaging of human brain function. *Trends in Neurosciences* 20:435–442.

Vyazovskiy, V., Olcese, U., Lazimy, Y., Faraguna, U., Esser, S., Williams, J., Cirelli, C., and Tononi, G. 2009. Cortical firing and sleep homeostasis. *Neuron* 63:865–878.

Wu, J., Gillin, J., Buchsbaum, M., Hershey, T., Hazlett, E., Sicotte, N., and Bunney Jr, W. 1991. The effect of sleep deprivation on cerebral glucose metabolic rate in normal humans assessed with positron emission tomography. *Sleep* 14:155–162.

Yao, X.-C., Foust, A., Rector, D. M., Barrowes, B., and George, J. S. 2005. Cross-polarized reflected light measurement of fast optical responses associated with neural activation. *Biophysical Journal* 88:4170–4177.

Yao, X.-C. and George, J. S. 2006a. Dynamic neuroimaging of retinal light responses using fast intrinsic optical signals. *NeuroImage* 33:898–906.

Yao, X.-C. and George, J. S. 2006b. Near-infrared imaging of fast intrinsic optical responses in visible light activated amphibian retina. *Journal of Biomedical Optics* 11:064030.

Yao, X.-C., Rector, D. M., and George, J. S. 2003. Optical lever recording of displacements from activated lobster nerve bundles and nitella internodes. *Applied Optics* 42:2972–2978.

Yodh, A. and Chance, B. 1995. Spectroscopy and imaging with diffusing light. *Physics Today* 48:34–41.

Zoccoli, G., Walker, A., Lenzi, P., and Franzini, C. 2002. The cerebral circulation during sleep: regulation mechanisms and functional implications. *Sleep Medicine Reviews* 6:443–455.